APPLICATION AND MODELING OF FREQUENCY-DOMAIN LIFETIME SPECTROSCOPY FOR MICROSPHERE-BASED OPTICAL GLUCOSE SENSORS

A Dissertation

by

FENG LIANG

Submitted to the Office of Graduate Studies of
Texas A&M University
in partial fulfillment of the requirements for the degree of

DOCTOR OF PHILOSOPHY

December 2006

Major Subject: Chemical Engineering

APPLICATION AND MODELING OF FREQUENCY-DOMAIN LIFETIME SPECTROSCOPY FOR MICROSPHERE-BASED OPTICAL GLUCOSE SENSORS

A Dissertation

by

FENG LIANG

Submitted to the Office of Graduate Studies of
Texas A&M University
in partial fulfillment of the requirements for the degree of

DOCTOR OF PHILOSOPHY

Approved by:

Chair of Committee,	Eva M. Sevick-Muraca
Committee Members,	Michael A. Bevan
	Friedhelm Schroeder
	Mahmoud El-Halwagi
Head of Department,	Kenneth R. Hall

December 2006

Major Subject: Chemical Engineering

ABSTRACT

Application and Modeling of Frequency-domain Lifetime Spectroscopy for Microsphere-based Optical Glucose Sensors. (December 2006)

Feng Liang, B.S., China University of Petroleum;

M.S., China University of Petroleum

Chair of Advisory Committee: Dr. Eva Sevick-Muraca

A new glucose affinity sensor based on a homogeneous fluorescence resonance energy transfer (FRET) assay system was developed to monitor the competitive binding between concanavalin A (ConA) and dextran. The FRET quenching kinetics of the donor were analyzed from frequency-domain (FD) measurements as functions of both glucose and acceptor-protein concentrations using a Förster-type decay kinetics model. The results showed that the FD measurements and donor decay kinetics can indicate quantitative changes in the presence of glucose at concentrations ranging from 0 to 224 mg/dL.

The second set of experiments proved the feasibility of performing analyte sensing with FD lifetime spectroscopy using microsphere-based sensors in multiple scattering solutions. A well characterized pH-sensitive fluorophore was entrapped in poly(ethylene glycol) microspheres. The particles were then immersed in a buffered polystyrene solution of various pH. Measurements of phase shift and modulation of the generated and multiply scattered fluorescent light were acquired as the modulation frequency of the incident excitation light varied from 10 to 120 MHz. After the

measured data were analyzed with the coupled diffusion equations, the obtained lifetimes from the scattering measurements matched values from non-scattering measurements.

Lastly, a new two-speed Monte Carlo (MC) simulation was developed to predict light propagation through the sensors and thus was used to evaluate these sensors and to design these sensors for implantation. The model used random packing structure and considered geometric optics and two light propagation speeds. Experimental measurements of phase-shift and modulation of excitation light were made on a cubic phantom with non-fluorescent resin microspheres of 74 μm diameter, and compared to those computed from the MC simulation. The results showed that the mean phase shift (PS) deviation was 0.736˚ and the mean amplitude deviation was 42%. Quantitative changes in detected fluorescence phase-shift and modulation were investigated for microsphere diameter, volume fraction, refractive index, and fluorophore lifetime. We also found that even though the sensitivity of PS change in the presence of scattering was the same as the value without scattering, the values of PS were magnified due to the scattering effects.

DEDICATION

To my parents, my wife, and my son

ACKNOWLEDGMENTS

There are lots of people I would like to thank who contributed directly or indirectly to the completion of my thesis.

First, I wish to thank my advisor, Dr. Eva Sevick-Muraca. She is one of the most respected professors whom I have had the opportunity to interact with and learn from. Her continued support and encouragement allowed me to pursue several areas of research that I have found very interesting.

I wish to express my sincere appreciation to my previous and current committee members for their guidance and support throughout the course of this research. They are: Dr. Michael Bevan, Dr. Friedhelm Schroeder, Dr. Mahmound El-Halwagi, Dr. Chun Li, and Dr. Babara Atshaves.

I wish to thank Mrs. Xiaoxia Wen and Dr. Avery McIntosh. I also wish to thank the following people from Electrical Engineering, Chemistry, and Biochemistry departments at Texas A&M University: Huiliang Zhang, Dr. Xiangshi Tan, Dr. Tinglu Yang, Dr. Mauricio Lasagna, and Dr. Liqun Gu. My research gave me the opportunity to talk with those intelligent people.

I wish to thank all my colleagues at the Photon Migration Laboratory, especially Drs. Eddy Kuwana, Yingqing Huang, Jessica Houston, Alan Thompson, Michael Gurfinkel, Anu Godavarty, Amit Joshi, Zhigang Sun, Dali Sarabjyot, and John Rasmussen. Working with my group members, I improved my communication skills and learned many new research techniques.

I am especially grateful to Dr. Tianshu Pan for our successful collaboration. He is the smartest person I ever met.

I wish to thank Towanna Hubacek and the Chemistry Department at Texas A&M University for providing help and support throughout my studies and research. I also wish to thank the Radiology Department at Baylor College of Medicine for providing support for my last year of research. Especially, I wish to thank Dr. Kristen Adams, Dr. Shi Ke, and Jessica Nollkamper at the Division of Molecular Imaging.

Finally I wish to thank my parents, my parents-in-law, and my wife. They have always inspired and supported me, especially through my Ph.D. work. Without them, I could not have successfully completed my Ph.D.

TABLE OF CONTENTS

Page

Page

Page

Page

LIST OF FIGURES

Page

Page

Page

Page

LIST OF TABLES

Page

1. INTRODUCTION

1.1 Motivation

1.1.1 The Importance of Continuous Glucose Sensing

The daily routine for a diabetes patient currently involves pricking the skin and drawing blood 4 to 8 times a day measure the blood glucose level. According to the Centers for Disease Control and Prevention, 20.8 million people, or about 7% of the total population in the U.S. had either type I or type II diabetes in 2005 (1) . The World Health Organization estimates the number of diabetes patients worldwide to be 300 million by the year 2025 (2). Currently, diabetics are directly treated by either pancreas transplantation or islet cell transplantation. There are many technical difficulties associated with both approaches, such as transplantable organ shortage, immune complications, and organ or cell failure (3). The recent interest in stem cell research has attracted public interest but the hope of large scale, cell-based treatment of diabetes has a long way from fruition (4). An alternative approach to treat diabetes is based upon the idea of an artificial beta cell (5). The artificial beta cell could measure glucose concentration and then automatically deliver insulin needed. Therefore, the most important component of the artificial beta cell is the continuous glucose-sensing unit.

This dissertation follows the style of *Photochemistry and Photobiology*.

Continuous glucose monitoring would allow diabetics to immediately, accurately, and conveniently control their glucose levels, thereby reducing the most serious complications of diabetes, including heart disease, blindness, amputations of extremities, and early death. Diabetes has an annual economic cost in the U.S. of more than 132 billion dollars, making the continuous glucose sensor the "holy grail" of all biomedical sensor development efforts.

Glucose is represented as $C_6H_{12}O_6$. It has a molecular weight (MW) of 180 Da and a molecular size less than 5 Å. In solution, the molecules are not open chains but rings as shown in Figure 1.1 (6). Glucose levels in normal blood range from 90 mg/dL to 120 mg/dL (7,8)). In diabetes, blood glucose levels may fluctuate between 40 mg/dL and 400 mg/dL (8). The "gold standard" for glucose measurement requires the patient to extract a drop of blood (typically by pricking the fingertip or the forearm). The glucose in the blood reacts with the oxygen in the air and is catalyzed by the glucose oxidase (GOX) enzyme to produce hydrogen peroxide. The hydrogen peroxide is then detected, providing an indirect measurement of glucose concentration.

$$D-glucose + O_2 + H_2O \xrightarrow{GOX} D-gluconate + H_2O_2 \qquad (1.1)$$

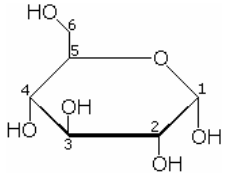

Figure 1.1. The molecule structure of glucose in aqueous solution.

The finger-pricking enzymatic measurement method consumes blood and has several severe limitations such as low accuracy, constant calibration, poor compliance from diabetic patients, and most importantly, the inability to continuously monitor changing glucose levels. It has been reported that a tighter control of blood glucose in insulin-dependent diabetics could reduce the severity of long-term complications such as retinopathy, nephropathy, and neuropathy (9). Therefore, a new glucose monitoring system capable of continuous measurement is needed. Currently the three commercially available mini-invasive glucose sensors which perform continuous monitoring based on enzymatic analysis, are: MiniMed-Medtronic Continuous Glucose Monitoring System (CGMS) (Northridge, CA, USA); GlucoWatch biographer (Animas, West Chester, PA), and GlucoDay microdialysis system (Menarini, Medulla, Italy). None of these systems are adequate due to a lack of biocompatibility and significant signal drifts (10,11).

1.1.2 Fluorescence Lifetime Spectroscopy as an Emerging Tool for Glucose Sensing

A number of minimally invasive or noninvasive techniques have been investigated for glucose monitoring during the last decades. The optical sensing methods which are promising for physiological glucose sensing include near-infrared (NIR) absorption spectroscopy (12-14), Raman spectroscopy (15), surface plasmon spectroscopy (16-18), polarimetric measurement of eye fluids (19), light scattering measurement (20-22), optical coherence tomography (OCT, (23)), and fluorescence spectroscopy (24,25). In Section 2.1, a review of optical glucose sensing techniques is provided.

In light of the difficulties associated with conventional glucose meters, fluorescence spectroscopy may provide a feasible and robust way to create a new type of implantable glucose sensor (7). The concept of fluorescence is shown in the Jabłoński diagram at Figure 1.2. The fluorophore lifetime, τ_0, which is typically on the order of 10^{-9} seconds, is defined as the average time the fluorophore spends in its excitation state and is shown mathematically as Equation 1.2:

$$\tau_0 = \frac{1}{\kappa_{nr} + \kappa_r} \tag{1.2}$$

where the κ_{nr} and κ_r refer to the rate of non-radiative relaxation and radiative relaxation of the fluorophore. The fluorescence quantum efficiency Q is defined as the ratio of the number of fluorescent photons emitted to the number of excitation photons absorbed by the fluorophore:

$$Q = \frac{1}{1 + \kappa_{nr} / \kappa_r} \tag{1.3}$$

Both lifetime and quantum efficiency of fluorophores are known to be sensitive to the local biological and chemical environments (26). There are many intra- and intermolecular interactions which influence the fluorophore lifetime such as collision quenching and FRET. Therefore the measured fluorescence lifetime τ is usually shorter than τ_0. Thus the measured fluorescence lifetime is the inverse of the total rate of all relaxation processes that cause deactivation from the excitation state.

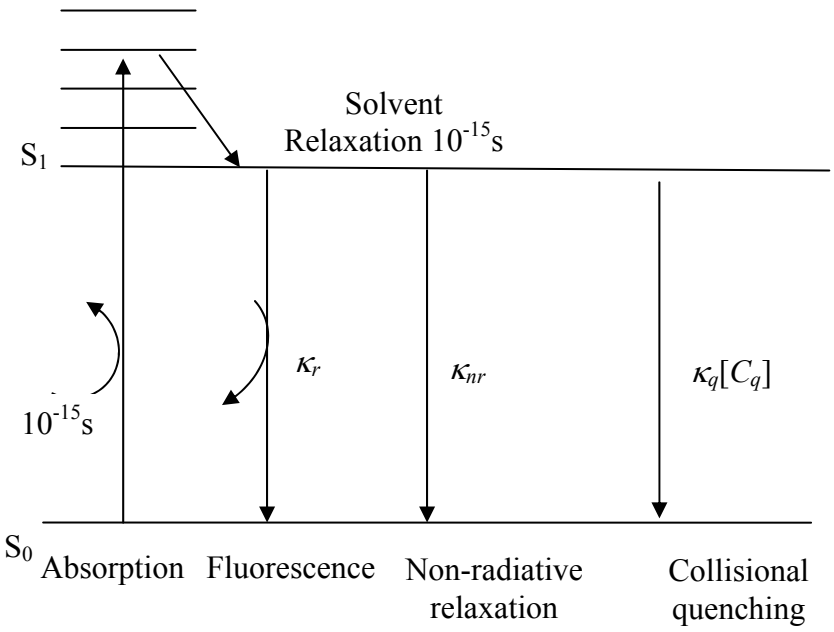

Figure 1.2. Jabłoński diagram illustrating absorption, fluorescence and non-radiative relaxation and collisional quenching, where κ_r and κ_{nr} correspond to the rate of radiative and non-radiative relaxation. The term κ_q is the Stern-Volmer constant for collisional quenching . $[C_q]$ is the quencher concentration. S_0 is the electronic ground state and S_1 is the first excited singlet state. Adapted from Richards-Kortum and Sevick-Muraca (27).

In the presence of collisional quenching and FRET, the measured fluorescence lifetime is given as Equation 1.4:

$$\tau = \frac{1}{\kappa_{nr} + \kappa_r + \kappa_T + \kappa_q \left[C_q \right]} \tag{1.4}$$

where the κ_q is the Stern-Volmer constant; κ_T refers to the rate of FRET; and $[C_q]$ is the quencher concentration.

While the fluorescence intensity measurements are technologically simple and straightforward, they can suffer from distortion of emission spectra because of the

wavelength dependent scattering and absorption properties of tissues. Fluorescence lifetime measurement provides more intrinsic advantages as compared to fluorescence intensity measurement. The lifetime measurement is not influenced by fluorophore photobleaching (28), fluorophore concentration fluctuation (29), and instrumentation artifacts (30). Lifetime-based chemical sensing has been proposed by several groups for the quantitation of pO_2 (31), pH (32) , Ca^{2+} (33), Cu^{+} (34), Zn^{2+} (35), and other metabolites.

For a sensor implanted in tissue, scattering and absorption of tissue will attenuate the intensity of the fluorescent signal and add nanosecond "time-of-flight" to the photon propagation in the tissue (27). Both signal attenuation and photon "time-of-flight" must be accounted for in order to achieve quantitative *in vivo* analyte sensing in tissue. Fluorescence lifetime measurements can be made independently of tissue scattering and absorption properties (36). Most importantly, previous work has shown that the combination of (i) fluorescence lifetime spectroscopy, (ii) models of fluorescence lifetime decay kinetics, and (iii) models of time-resolved light propagation enabled quantitative biomedical sensing in tissue phantoms (30). In this work, the feasibility of using lifetime measurement to detect glucose concentrations within the physiological range is presented.

1.1.3 Implantable Polymer Microsphere-based Glucose Sensors

The idea of implantable glucose sensors was initially reported in 1974 by Alibisser *et al.* (37). Drs. Cote and Pishko's research groups first investigated using a "smart tattoo" consisting of small polymer microsphere-based implantable sensors for

monitoring glucose (38-42). The idea was to physically or chemically immobilize the fluorophores and glucose-sensitive affinity system inside a polymer matrix for protection of the fluorophore. The polymer protection also increased the stability of glucose sensitive affinity system in biological samples and decreased toxicity. After the microsphere-based sensors were implanted in the skin, fluorescence intensity spectra were obtained by noninvasively scanning the skin surface and were analyzed for the glucose concentration (41). Their results showed feasibility for qualitative glucose monitoring with fluorescence intensity measurements (40). Initially in their study, alginate-poly-L-lysine microparticles were used. Subsequent work employed PEG due to its biocompatibility and porous structure, which removed transport limitations. Recent experimentation has explored alternate polymer types, including Sephadex(43), Sepharose(44), polystyrene(45,46), and polyelectrolyte-coated alginate microbeads (38,47). All of these studies measured changes in fluorescence intensity with glucose concentration. The work presented in this dissertation sought to measure florescence lifetime changes arising from physiological glucose concentrations in a microsphere-based sensor. Figure 1.3 illustrates a possible scheme for implantable polymer microsphere-based, fluorescence glucose sensors.

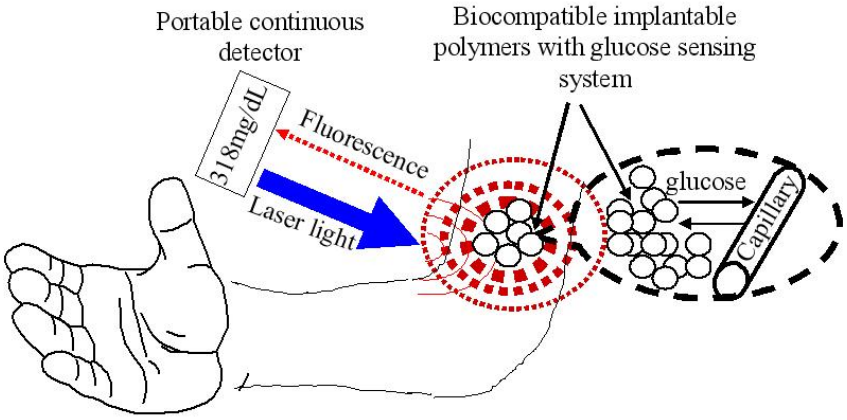

Figure 1.3. A potential scheme for continuous glucose sensing using fluorescence and implantable polymer microspheres. In this case, a portable continuous detector provides laser light and detects the fluorescence signal change with glucose level in the interstitial fluid. The polymer microspheres are implanted underneath the skin.

1.1.4 Using Protein-dextran Affinity System and FRET to Measure Glucose Concentration

Many efforts to develop noninvasive glucose sensors have focused upon the ConA–dextran affinity system for FRET-based sensing of glucose as an alternative to conventional enzymatic glucose sensors (24,32,40,41,44,48-54). In this scheme, the sugar-binding plant lectin, ConA, is labeled with fluorescent dyes acting either as donor or acceptor and competitively binds glucose and dextran (48,50). Competitive binding can be followed if the dextran is also conjugated with a fluorescent dye which acts as the corresponding acceptor or donor. The change of FRET between donor and acceptor due to competitive binding can be monitored to determine the concentration of glucose (48). For this affinity system, the acceptor, which itself might not necessarily be fluorescent

(50,51), has been labeled to either ConA or dextran without any clear advantage of one over another (44,50,51).

1.2 Goals of the Research

The goal of the research is to apply fluorescence lifetime spectroscopy to the development of an implantable, polymer microsphere-based optical sensor for glucose. Despite the current progress of development of polymer-based implantable glucose sensors (38,40,41,55,56), three elusive questions remain to be answered for the development of microsphere-based fluorescence implantable sensor:

1. Could FD lifetime measurements be used to determine glucose concentration in the physiological range? If so, what is the relationship between fluorescence decay kinetics and binding affinity?

2. Could fluorescence lifetime sensing using frequency-domain photon migration (FDPM) techniques be applied to detect fluorescence lifetime for implantable glucose sensors in scattering tissues?

3. How should the implantable polymer microsphere-based sensors be designed for lifetime measurement?

The specific aims of this research are:

1. To develop a new glucose-sensitive affinity system based upon FRET, then to measure the glucose concentration in non-scattering solution using FD lifetime spectroscopy, finally to assess changing FRET decay kinetics with glucose concentrations.

2. To explore the feasibility of fluorescence lifetime sensing in microsphere-based implantable sensors in tissue-mimicking scattering phantoms.

3. To develop and experimentally validate a new Monte Carlo model for light propagation in microsphere-based implantable sensors.

1.3 Organization of Dissertation

The flowchart in Figure 1.4 provides the sequences of sections and the topics presented.

Section 2 provides a detailed review of various optical techniques used in glucose sensing and highlights the fluorescence spectroscopic methods. The theories and application of FRET are introduced and previous applications of FRET measurements in glucose sensing are detailed. Finally, an introduction to the glucose sensitive ConA-dextran affinity sensor is introduced and reviewed.

In Section 3, time-dependent light propagation, its theory, and the incorporation of fluorescence decay kinetics are presented.

Section 4 contains published work towards this thesis demonstrating measurement of FRET for a new glucose-sensitive affinity system and analysis of FRET decay kinetics (57).

In Section 5, the results are presented for implantable pH sensors in the tissue-mimicking scattering solution using FD lifetime measurement (58).

Section 6 details the development of a new MC simulation of fluorescence light propagation capable of predicting fluorescence lifetime measurements. The simulation method was experimentally validated in a resin-packed, three dimensional phantom.

Then the influence of optical/physical properties of the microspheres is discussed using the simulation results.

In Section 7, the major results of the research are summarized and possible future studies are presented.

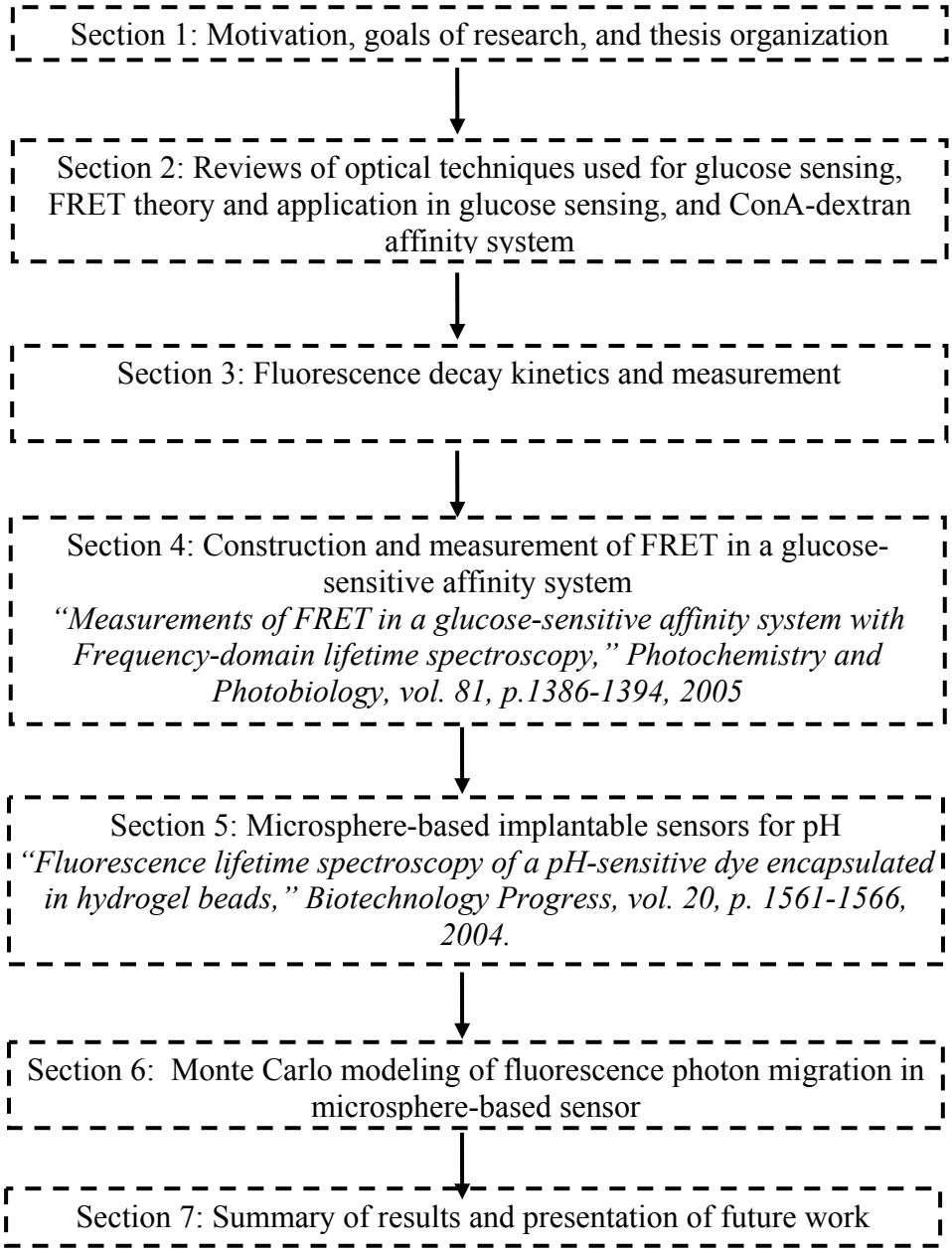

Figure 1.4. Organization of the dissertation.

2. BACKGROUND: OPTICAL GLUCOSE SENSING TECHNIQUES, FRET THEORY, AND CONA-DEXTRAN AFFINITY SYSTEM

To preface the application of fluorescence lifetime spectroscopy in glucose sensing, a complete summary is provided below describing optical glucose sensing techniques, FRET theory and its application to glucose sensing, and the ConA-dextran affinity sensor.

2.1 Optical Techniques Used to Monitor Glucose Concentration *in vivo*

Optical techniques for glucose monitoring are promising and are one of the fastest growing biomedical areas because: (i) optical sensing may provide noninvasive measurements without detectors physically contacting the body, for patients leading to less pain and more convenience; (ii) fast reading of signal changes should allow continuous glucose monitoring; (iii) when used non-invasively, optical signal is not subject to ambient electrical interference; and (iv) optical sensors do not consume glucose or blood in the body.

Typically optical glucose measurement techniques focus on measuring the change in optical properties with change in blood glucose levels. Change in blood glucose level will change the scattering coefficients, μ_s, isotropic or reduced scattering coefficient, μ_s', the absorption coefficients of tissue, μ_a', and polarization of the transmitted or backscattered light. The isotropic or reduced scattering coefficient μ_s' is define as: $\mu_s^{'} = \mu_s(1-g)$, where the parameter g is the mean of the cosine of the scattering angle.

Table 2.1 provides an overview of the influence of glucose concentration on measured tissue optical properties. In this review, we classify the bulk of recent research on optical glucose sensing techniques into two different groups: (i) non-fluorescence glucose sensing optical methods, which include light scattering, NIR and Raman spectroscopy, photonic crystal method, OCT, and polarimetry; and (ii) fluorescence-based glucose sensing optical methods. The review of each technique will start by introducing its optical/physical principles, and discussing recent results and difficulties which still remain to be overcome. The optical glucose monitoring techniques can be classified as shown in the following Figure 2.1.

Table 2.1. A summary of the effect of glucose concentration change upon measured optical properties of tissues, measured diffraction signal, and measured Raman intensity.

Increasing glucose concentration		**Methodology**
Change in absorption		
Water absorption coefficient	$\mu_a^w(\lambda) \downarrow$	NIR and mid-IR spectroscopy Photoacoustic spectroscopy
Intrinsic glucose absorption coefficient	$\mu_a^g(\lambda) \uparrow$	
Change in scattering		
Scattering or Isotropic scattering coefficient	$g \uparrow \mu_s(\lambda) \downarrow \mu_s'(\lambda) \downarrow$	Light scattering measurements, OCT
Change in polarization		
Observed rotation	$\phi(\lambda) \uparrow$	polarimetry
Change in photonic crystal		
Observed diffraction	Blue-shift ↑ (59) or red-shift ↑ (60)	Photonic crystal measurement
Change in Raman scattering		
Observed Raman Intensity	Intensity ↑	Raman spectroscopy

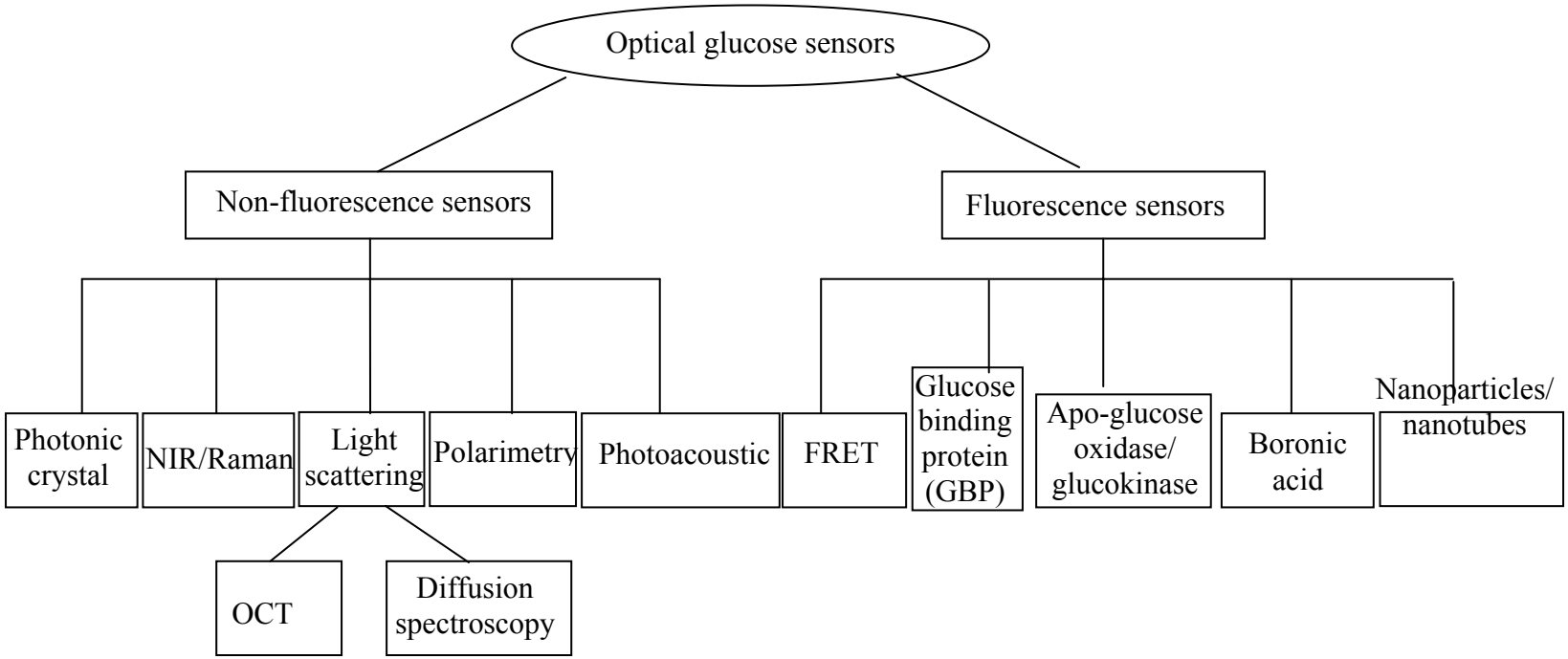

Figure 2.1. The various optical glucose sensing techniques reviewed in this section.

2.1.1 Non-fluorescence Glucose Sensors

2.1.1.1 Light Scattering Methods

Light scattering methods rely on the refractive-index change caused by glucose concentration changes. Therefore the measured optical isotropic scattering coefficient of tissue, μ_s', changes with the concentration of glucose in the extracellular fluid. For a simple model of scattering spherical particles, the isotropic scattering coefficient, μ_s' can be related to the refractive index of the scattering medium based on the Mie theory as shown in the following equation (23,61):

$$\mu_s' = 20.34 r^2 \rho_p \left(\frac{r}{\lambda}\right)^{0.37} \left(\frac{n_p}{n_m} - 1\right)^{2.09} \qquad (2.1)$$

where r is the spherical particle radius; ρ_p is the volume density of the particles; λ is the wavelength of incident light; and n_p , n_m are the refractive indices of particles and the medium. Increased glucose concentration will increase the refractive index of the medium, n_m and thus decrease the isotropic scattering coefficient.

The refractive-index increment of an aqueous glucose solution Δn_m for visible wavelength is 2.5×10^{-5} /mM glucose (20-22). By using polystyrene and lyposyn aqueous phantoms, two research groups have shown that the presence of glucose dissolved in an aqueous solution increased the refractive index of the solution and therefore influenced the scattering properties of particles suspended within it (20,21). Kohl *et al.* measured the fractional change of the isotropic scattering coefficient $\Delta\mu_s'$ (cm^{-1}) caused by glucose to be -0.016%/mM glucose (22). Maier *et al.* demonstrated that the small change in

scattering coefficient made it difficult to measure glucose level in biological tissues due to confounding factors from other tissue substances and organelles, and blood glucose distribution. He used a FD reflectance system on the thigh of a normal volunteer (21). Bruulsema *et al.* evaluated the sensitivity of the isotropic scattering coefficient for monitoring change of blood glucose levels in 41 diabetic volunteers (62). They used a charged-coupled device (CCD) detection system to measure the tissue reflectance. Their results showed qualitatively that they could relate tissue reflectance with blood glucose concentration on the patients. However, the unclear drifts in measured μ_s' prevented the quantitative correlation between μ_s' and blood glucose level.

Extensive work explored using OCT to measure the changes in scattering coefficient, μ_s (63). This method was first studied in animals and then in healthy volunteers (64). Larin *et al.* used OCT to measure scattering coefficient changes in the skin of Yucatan micropigs and New Zealand rabbits (23). In the human study, a difference of 10 mg/dL glucose corresponded to 1.2-2% change in the slope of the linear fit of OCT signals (64).

2.1.1.2 NIR Spectroscopy

IN the last decade most of the research in this field has focused on NIR spectroscopy. This method has been used to extract glucose concentrations from reflectance or transmission spectra with wavelengths from 600 to 1300nm or even longer than 2μm. This method is based upon the fact that (i) increasing glucose concentration will increase the intrinsic absorption of glucose bands, and (ii) increasing glucose

concentration will decrease the intrinsic absorption of water bands by the volume displacement of water with glucose (65). Using multivariate analysis techniques to relate NIR responses and glucose concentrations to the spectral changes, models can be derived in which there is a good correlation between NIR readings and blood glucose concentrations (12,14,66-69). Unfortunately, poor precision due to interference from several confounding factors such as (i) background noise, (ii) change of temperature, pH, and scattering, (iii) skin pigmentation, (iv) blood flow variation, and (v) probe placement and probe pressure have slowed clinical development. Raman spectroscopy, based on the inelastic scattering of incident light, also has similar difficulties (70).

2.1.1.3 Photonic Crystal Method

The photonic crystal method involved diffraction of light from polymerized crystalline colloidal arrays (PCCAs) that swell with changes in glucose concentration (59,71). The PCCA is polymerized within a hydrogel film that includes GOX or phenylboronic acids. When GOX reacts with glucose or when the boronic acids reversibly bind glucose, the pH of the hydrogel is reduced and the hydrogel expands. The expansion caused an increase in the spacing between the spherical polystyrene colloids (~10 μm in diameter) bound to the hydrogel. This caused the angle at which light is diffracted off of the spherical colloids to increase, enabling detection of glucose concentration changes (72). The photonic crystal sensor was tested recently with artificial tear fluids and is intended to be worn as a contact lens (73). The sensitivity and specificity of this sensor primarily depend on the glucose recognition group, which is

either GOX or boronic acid. Therefore, it faced the similar problems as found with other GOX or boronic acid-based glucose sensing methods, as discussed below in section 2.1.2.

2.1.1.4 Polarimetric Method

The polarimetric method is based on the fact that glucose, as an optically active molecule, will rotate the plane of linearly polarized light passing through the solution (24). The relationship between glucose concentration [*C*] and measured rotation $\phi(\lambda)$ in solution is shown as follows (65):

$$[C]_{glucose} = \frac{\phi(\lambda)_{measured}}{\phi(\lambda)_{specific}} \frac{1}{L} \qquad (2.2)$$

where $\phi(\lambda)_{specific}$ is the specific rotation of the glucose at a given wavelength λ. At 589 nm, $\phi(\lambda)_{specific}$ is equal to 52.6˚. The term *L* is the path length, and $\phi(\lambda)_{measured}$ is the observed rotation in degrees. $\phi(\lambda)_{measured}$ is also the function of temperature and pH.

Within physiological concentrations and when the pathlength *L* is equal to 1 cm, glucose will rotate the linear polarization of a light beam about 0.4 millidegrees per 10 mg/dL. Cameron *et al.* presented *in vivo* results from a laser-based optical polarimetry system using the anterior chamber of rabbit eyes to demonstrate the potential non-invasive glucose monitoring method (19). Challenges with polarimetric glucose sensing in the eye include other optical rotations due to the cornea, birefringence of the cornea, movement of the eyes, and the presence of other optically active components in the aqueous humor (7).

2.1.1.5 Photoacoustic Spectroscopy

The photoacoustic technique involves the creation of acoustic wave by the absorption of light energy. The ultrasonic pressure generates a pulse that propagates and can be detected by a piezoelectric detector (74). For a weak absorbing sample, the generated pressure increase can be described by the following equation (75):

$$\Delta P = \left(\frac{\beta v^2}{C_P} \right) \Phi \mu_a \tag{2.3}$$

where β is the coefficient of thermal expansion; v is the speed of sound in the medium; C_p is the specific heat of the medium; Φ is the light fluence; and μ_a is the absorption coefficient of the medium. As it can be seen from the above Equation 2.3, the pressure increase is the proportional to the absorption coefficient of the irradiated medium. Eqation 2.3 represents the principle of photoacoustic spectroscopy for glucose sensing. Mackenzie *et al.* reported *in vitro* and *in vivo* experimental photoaccoustic results using the wavelength range from 800 nm to 1200 nm (75). Their *in vitro* experiments investigated the interference effects from sodium chloride, cholesterol, and bovine serum albumin and showed that they did not influence the photoacoustic signal due to the change of glucose concentration. A study with 53 volunteers showed good correlation between the photoacoustic measurements and the measured blood glucose concentrations. Kinnunen *et al.* conducted photoacoustic measurement in 1% intralipid and whole blood of swine at the wavelengths of 532 nm and 1064 nm (74). The sensitivity of photoacoustic signals to change in glucose concentration was higher in blood samples

(11.4%/500 mg.dL^{-1}) than the intralipid sample (1.35%/500 mg.dL^{-1}). There is however, a potential problem in the non-invasive photoacoustic measurement which lies in the confounding effects of temperature change.

2.1.2 Fluorescence-based Glucose Sensor

Fluorescence-based glucose measurement methods have involved fluorescence spectroscopy to measure fluorescence intensity, anisotropy, or lifetime change with glucose concentration change. Based on different transduction mechanism and recognition elements for glucose, these approaches fall into five categories listed below:

(i) The lectin ConA – dextran affinity system,

(ii) GBP based glucose sensing system,

(iii) Apo-glucose oxidase or glucokinase sensor,

(iv) Boronic acid – based glucose sensing systems, and

(v) Gold or silver nanoparticles, quantum-dot, PEBBLEs, and nanotube based glucose sensing systems.

The lectin ConA-dextran affinity system is the most intensively studied system. It is reviewed in section 2.3. The brief review of the rest of these techniques in the following section will focus on answering three questions: (i) what is the basic mechanism of these fluorescent sensing methods? (ii) are the fluorescent decay mechanisms investigated and if so, how are the fluorescent lifetime changes related to glucose concentration change? And finally, (iii) what are the measurement methods and choice of wavelengths?

2.1.2.1 GBP based Glucose Sensing System

A variety of well characterized GBPs have been isolated from *Escherichia coli* and other bacteria. The proteins have been engineered such that glucose binding events could be traced by site specifically attached fluorophores, either through conformational change-induced FRET between donor-acceptor pairs on the protein or by fluorescent changes from an environmentally sensitive single fluorophore (76,77). Tolosa *et al.* demonstrated a mutated GBP with a single cysteine residue and an environmentally sensitive fluorophore 2-(4-iodoacetamidoanilino)naphthalene-6-sulfonic acid (I-ANS) (77). In the experiments, the excitation wavelength was 325 nm and emission wavelength was 450 nm. The response to glucose displayed a twofold decrease in intensity but no change in fluorescence lifetime. Ye and Schultz fused two fluorescent reporter proteins (green fluorescent protein (GFP) as the FRET donor and yellow fluorescent protein (YFP) as the FRET acceptor) to each end of a GBP (76). Glucose binding resulted in a conformation change and reduced FRET. Both GBP systems have narrow glucose sensing ranges (up to 0.18 mg/dL) and the measurement wavelength is in the UV range (<400 nm) where tissue penetration of light is minimal. All of these results were obtained from measuring intensity in free solutions. Another recent study using GBP and surface plasmon resonance (SPR) has reported a the low sensing range of glucose concentration (up to 36 mg/dL) (78).

2.1.2.2 Apo-glucose Oxidase and Glucokinase Sensors

An inactivated form of GOX has been developed without the ability to oxidize glucose wile maintaining the ability to bind glucose (79). In the study carried out by D'Auria *et al.*, the fluorophore, 8-anilino-1-naphthalene sulfonic acid (ANS) was non-covalently bound to the apo-glucose oxidase (80,81). The addition of glucose (from 0 to 60 mM) caused ~ 25% decrease in fluorescence intensity from ANS and a 25% decrease in lifetime as found using FD lifetime measurements in free solution (80). In this research, the excitation wavelength was 335 nm while the emission wavelength was 535 nm. The same research group also explored using thermostable glucokinase from the thermophilic microorganism *Bacillus stearothermophilus* (BSGK) (82). The ANS-labeled glucokinase displayed about a 25% decrease in the emission intensity but no change in lifetime. The excitation wavelength in their study was 295 nm. The McShane group used apo-glucose oxidase conjugated with TRITC and FITC-dextran to develop a competitive binding assay (83). The competitive binding system was encapsulated into polyelectrolyte microspheres (~5 μm in diameter). The sensitive study showed 67% change in fluorescence intensity signal as the glucose concentration ranged between 0 to 720 mg/dL (55,84). The toxicity and the stability of this apo-glucose oxidase sensor have not yet been reported.

2.1.2.3 Boronic Acid-based Glucose Sensors

Boronic acid binds covalently to diols to form five- or six-membered cyclic esters in aqueous basic media (85). James *et al.* first synthesized derivatives of boronic acid

which were linked to a fluorophore which coupled molecular recognition of glucose to a fluorescence change (86-88). They introduced the photoinduced electron transfer (PET) as a tool for the transduction of the fluorescence signal. PET glucose sensors generally consist of a fluorophore and a boric acid receptor linked by a short spacer. In the absence of glucose, the fluorescence intensity of the anthracene fluorophore (EX/EM = 370/423 nm) was quenched by the nitrogen atom within the PET sensor. Upon binding of glucose to the boronic acid receptor, PET was suppressed, resulting in the recovery of the fluorescence intensity of anthracene. The glucose sensing range was from 0.03 mM to 1 mM in a 33% MeOH/H_2O solution (pH=7.7). Camara *et al*. developed a boronic acid receptor by combining another fluorophore pyranine with a boronic acid substituted with benzyl viologen as a quencher (89). In the absence of glucose, the fluorophore/quencher complex is nonfluorescent. Upon binding of glucose, the complex dissociates, resulting in increased fluorescence intensity. DiCesare and Lakowicz have also studied fluorescence lifetime changes with glucose binding to boronic acid derivatives, including an anthracene derivative which showed an increase in mean lifetime from 6.4 ns to 11.5 ns with the addition of 10 mM glucose (90,91). In their recent study, the Lakowicz group developed glucose sensing contact lenses by embedding several boronic acid containing fluorophores (92). The approach may be suitable for continuous monitoring of tear glucose levels in the range of 0.05-1 mM. However, glucose measurement using boronic acid is subject to several difficulties (85): (i) many boronic acid-based sensors are not water-soluble; (ii) the selectivity for glucose among similar compounds (such as fructose,

galactose and mannose) is comparably lower than ConA-dextran affinity glucose sensor; and (iii) the sensitivity of the boronic acid-based sensors is influenced strongly by pH.

2.1.2.4 Nanoparticle or Nanotube-based Glucose Sensors

Aslan *et al.* reported using ConA-aggregated dextran-coated gold colloids and dextran with boronic acid-capped silver colloids to measure glucose concentration (16,93). They measured the change of SPR by changing the size of the nanostructure geometry due to the competitive binding between glucose and dextran to ConA or boronic acid.

Quantum dots (QDs) have been used in maltose sensing by Clapp *et al* (94,95), but have not yet been investigated for glucose sensing. In the maltose-sensing research, maltose-binding proteins labeled with Cy3 as the FRET acceptor were immobilized on a CdSe-ZnS core-shell QD. Change of QD lifetime owing to change of the immobilized maltose binding protein was measured using time-domain methods as discussed in section 3.2. The advantage of using quantum dots may rely on the size-dependent absorption and high photostability.

Barone *et al.* loaded $Fe(CN)_6^{3-}$/GOX-suspended carbon nanotubes into a 200 μm × 1 cm (MWCO =13 kDa) microdialysis capillary tube (96). The carbon nanotubes were tuned to have near-infrared (NIR) fluorescence emission. Upon placing the capillary beneath human epidermal tissue samples, they measured the fluorescence intensity change of carbon nanotubes with glucose concentration change at an excitation

wavelength of 785 nm. However, the detection limit of this sensing system was shown to be 34.7 μM.

Xu *et al*. presented an innovative polyacrylamide (PAA) PEBBLE glucose sensors (Probes Encapsulated by Biologically Localized Embedding) using ratiometric measurements (97). Using an emulsion polymerization process, the PEBBLE nanoparticles (~45 nm in diameter) incorporated GOX, an oxygen-sensitive fluorophore, $(Ru[dpp(SO_3Na)_2]_3)Cl_2$, and a reference dye, Oregon Green 488-dextran or Texas Red-dextran. The oxygen sensitive ruthenium dye was used to detect oxygen concentration change from an enzymatic reaction. The PAA hydrogel eliminated the interferences such as protein binding or membrane/organelle sequestration. The hydrogel matrix also minimized the dye toxicity to cells (98). The glucose sensing range of this sensor is up to 8 mM for fluorescence intensity measurement in PBS buffer solution (pH =7.2). This method has a response time of 100 s and has only been tested with *in vitro* microscopy studies, thus the feasibility of using this sensor for in *vivo* sensing is not known. The excitation wavelength in their study was 488 nm.

As discussed in this section, while glucose sensing based on intensity change has been studied in some depth, the potential of fluorescence lifetime measurements has yet to be investigated in any detail (10). Given that lifetime measurements have intrinsic advantages for *in vivo* sensing such as freedom from artifacts due to (i) light scattering, (ii) fluorophore concentration, and (iii) photobleaching, this research will explore frequency-domain technique by measuring FRET effects change in the ConA-dextran affinity sensor.

2.2 Review of FRET Theory and FRET Application in Glucose Sensing

2.2.1 Simplified FRET Theory

The theory of FRET is quite complicated; therefore the section focuses on a comprehensive description of (i) FRET basic theory, (ii) FRET decay kinetics, and (iii) FRET decay kinetics measurements. FRET is a physical process in which part of the energy from an excited fluorescent donor (D) molecule, nonradiatively transfers to another closely positioned molecule, defined as acceptor (A) located within 3-10 nm distance of the donor (26). The acceptor is not necessarily fluorescent (26). In this nonradiative energy transfer process, the donor does not emit a photon and acceptor does not re-absorb a photon from donor. Figure 2.2 illustrates the diagram of FRET and the Jabłoński diagram. the following schematic equation describes the FRET process (99):

$$\mathrm{D} + h\nu_E \rightarrow \text{ excited D} + \mathrm{A} \xrightarrow{k_T} \mathrm{D} + \text{excited A} \qquad (2.4)$$

where ν_E is the frequency of excitation; h is the Planck constant (6.626×10^{-34} J·s); and k_T is the energy transfer rate. The essential requirements for FRET to occur are: (i) adequate overlap in the emission spectrum of D and the absorption spectrum A; (ii) sufficiently high the quantum yield of D; (iii) a non-perpendicular relative orientation of the D-A transition dipoles (26); and (iv) the distance between D and A molecules should between ~10 Å and ~100 Å.

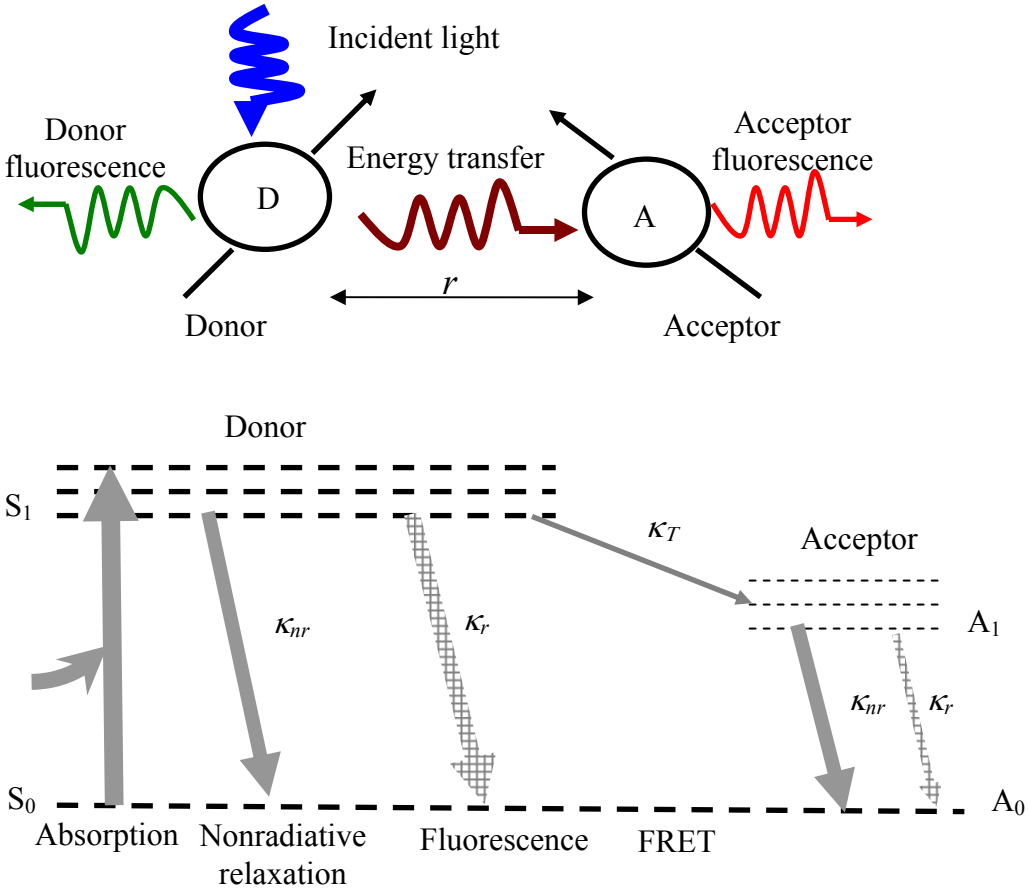

Figure 2.2. Illustration of the process of FRET (upper figure) and Jabłoński diagram (lower figure) illustrates the FRET process. D is the donor molecule and A is the acceptor molecule. r is the distance between donor and acceptor molecules. The parameters κ_r, κ_{nr} and κ_T correspond to the radiative relaxation, non-radiative relaxation, and fluorescence resonance energy transfer rate. S_0 is the electronic ground state and S_1 is the first excited singlet state. A_0 and A_1 correspond to the ground and excited electronic state of the acceptor, respectively.

If the donor and acceptor are assumed to be separated a constant distance (r), then with the dipole-dipole interaction, the non-radiative energy transfer rate is given by,

$$k_T(r) = \frac{1}{\tau_0}\left(\frac{R_0}{r}\right)^6 \tag{2.5}$$

where τ_0 is the unquenched donor fluorescence lifetime, and R_0 is the Förster distance. The Förster distance is defined as (92):

$$R_0^6 = \frac{161.9\kappa^2 Q}{\pi^5 n^4 N_A} \int_0^\infty F_D(\lambda)\varepsilon_A(\lambda)\lambda^4 d\lambda \tag{2.6}$$

where Q is the donor quantum yield in the absence of acceptor; n is the refractive index of solvent, for water, n is 1.33; $F_D(\lambda)$ is the normalized fluorescence spectra of the donor; $\varepsilon_A(\lambda)$ is the extinction coefficient of the acceptor; N_A is Avogadro's number (6.0221415×10^{23}); and κ^2 is the orientation factor. The integral in Equation 2.6 is defined as the overlap integral $J(\lambda)$ and it can be calculated from the overlap of the donor emission spectra and acceptor absorption spectra as well as from PhotochemCAD software (100) .

$$J(\lambda) = \int_0^\infty F_D(\lambda)\varepsilon_A(\lambda)\lambda^4 d\lambda \tag{2.7}$$

The overlap integral $J(\lambda)$ indicates the degree of spectral overlap between the donor emission and acceptor absorption. Figure 2.3 illustrates the spectra overlap of one FRET pair studied in this research. The acceptor, QSY21 is a non-fluorescent quencher while the donor is AF647. Both were obtained from Molecular Probes (Eugene, OR). It has to be emphasized that the spectral overlap is a necessary, but not a sufficient condition for FRET to be happen.

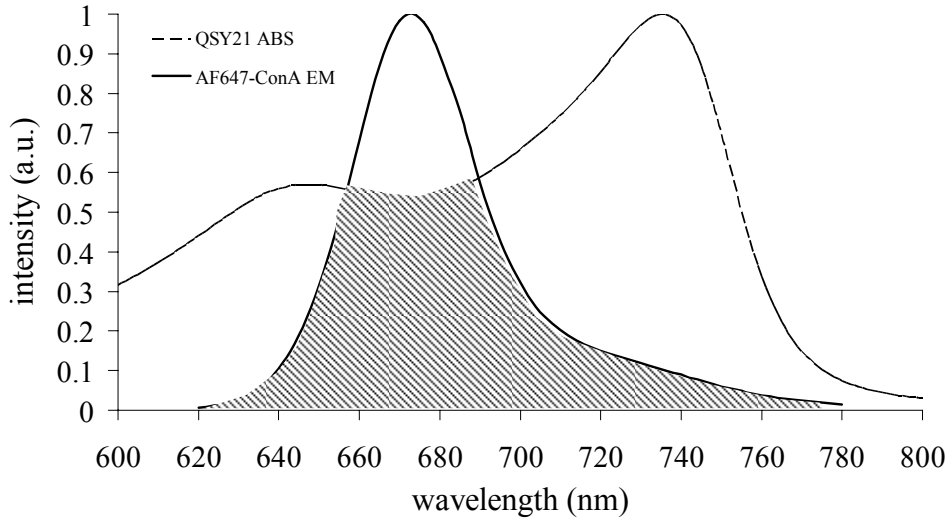

Figure 2.3. The absorption spectra of QSY21 (the dashed line) and the emission spectra of AF647 (the solid line) in PBS buffer (pH= 7.2). The shadow area in the figure shows the spectral overlap between donor (AF647) emission and acceptor (QSY21) absorption. The acceptor molecule, QSY21 is a non-fluorescent quencher.

Upon substituting Equation 2.7 into 2.6, and express the wavelength in nanometers, the Förster distance in Å is given can be written:

$$R_0^6 = 8.79 \times 10^{-5} \left\{ \kappa^2 n^{-4} Q J(\lambda) \right\} \tag{2.8}$$

The orientation factor κ^2 is equal to:

$$\kappa^2 = \left| \overrightarrow{\mu_A}\overrightarrow{\mu_D} - 3\left(\overrightarrow{\mu_D}\vec{R}\right)\left(\overrightarrow{\mu_A}\vec{R}\right) \right|^2 = \left(\cos\theta_T - 3\cos\theta_D \cos\theta_A\right)^2 \tag{2.9}$$

where the $\overrightarrow{\mu_A}$ and $\overrightarrow{\mu_D}$ are the unit vectors of the acceptor and donor transition moments and $\vec{R}$ is the unit vector joining the donor and the acceptor. θ_T is the angle between the emission dipole of the donor and the absorption dipole of the acceptor. θ_D and θ_A are the angles between these dipoles and the vector $\vec{R}$ (26). The value of κ^2 can vary from 0 to 4, but the orientation factor is rather difficult to determine in experimental systems. It is

normally assumed that κ^2 equals to 2/3 for randomly oriented D and A in bulk solutions (26). However, for immobilized systems, the orientation factor must be determined using Equation 2.9. Obtaining exact κ^2 is difficult and it has been suggested that the resulting uncertainty in κ^2 contributes a ~10% error in the Förster distance (101).

As shown in Equations 2.5-2.9, if the overlap integral *J(λ)*; the orientation factor κ^2; the donor quantum yield *Q*; the distance between donor and acceptor *r*; and the donor unquenched lifetime are known, then we may calculate the Förster distance R_0 and the energy transfer rate k_T.

The observed donor lifetime, τ_F, decreases with increasing energy transfer rate as shown in the follow equation:

$$\tau_F = \frac{1}{\kappa_{nr} + \kappa_r + \kappa_T} = \frac{\tau_0}{1 + \left(R_0 / r \right)^6} \tag{2.10}$$

The FRET efficiency, *E* is defined as the ratio of energy transfer rate k_T to the total decay rate of the donor and can be computed as follows:

$$E(r) = \frac{\kappa_T}{\kappa_{nr} + \kappa_r + \kappa_T} = \frac{\kappa_T}{1/\tau_0 + \kappa_T} = \frac{1}{\left(r / R_0 \right)^6 + 1} \tag{2.11}$$

The FRET efficiency is the fraction of energy absorbed by D that is nonradiatively transferred to the A. Therefore E could be used as the indicator of "strength of FRET." Equations 2.10–2.11 are valid only when the distance, r between D and A is constant. Both equations show that τ_F and E are strongly dependent on the distance between D and A. Figure 2.4 illustrates the simulation results of FRET efficiency as a function of D-A distance at different Förster distances and shows how the FRET efficiency is influenced by the change in the D-A distance. For example, if the Förster distance is 40 Å, the FRET efficiency approaches zero when the D-A distance is 90 Å. When the D-A distance is less than 20 Å, the FRET efficiency approaches 100% and will not change by further reducing the D-A distance. The observed FRET efficiency dependence on the D-A distance embodies the principle of FRET optical sensing techniques. The unique feature of FRET technique is its capability to quantitatively measure molecular interaction within 10-100 Å distance (101) . In a well studied allphycocyanin (APC, as D)-ConA and malachite green (MG, as A)-dextran affinity system, the computed D-A distance distribution curve had two maxima at 45 Å and 75 Å (102). With changing glucose concentrations, the calculated D-A distances also change significantly.

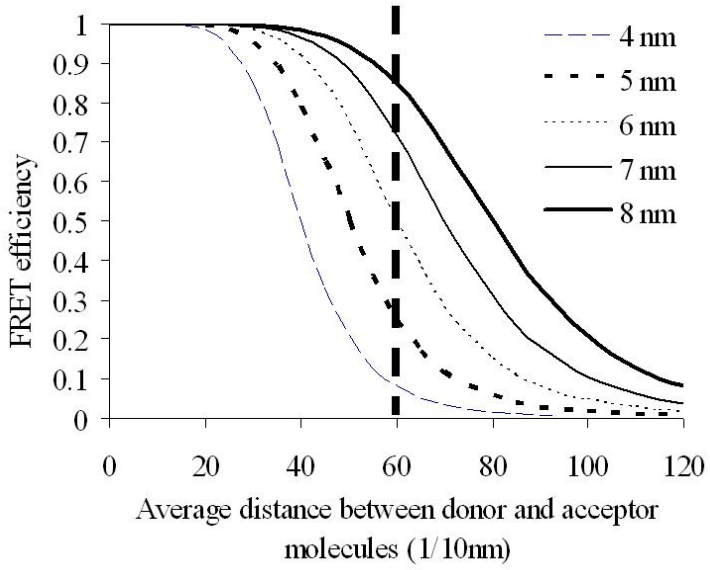

Figure 2.4. Dependence of FRET efficiency on the distance between D and A. The legend in the figure shows the different Förster distances, R_0, in nanometers. All the curves in this figure are the simulation results from Equation 2.11.

2.2.2 Summary of FRET Application in Glucose Sensing

FRET has been widely used to investigate: (i) protein structure, protein folding, and protein interactions (103); (ii) carbohydrate structure and conformation (104); (iii) metal ions sensing (Zn^{2+}, Cu^{2+}) (34); (iv) enzyme activity and kinetics (26); (v) nucleic acid structure and interaction (105); (vi) molecular interactions in membranes; and (vii) affinity sensors for quantitatively detecting gene, antigen, protein, and glucose concentration (106). This section focuses on reviewing the application of FRET specifically for glucose sensing. Table 2.2 provides a cumulative summary of the literature using FRET to measure glucose concentration *in vitro*.

Table 2.2. Review of literature involving glucose sensing based on FRET competitive-binding affinity system*.

Reference	Donor/ Acceptor	FRET affinity system	R_0 (Å)	λ, EX/ EM	Measurement methods/instrumentation	Glucose sensing range	Comments
Meadows and Schultz (1988) (107)	FITC/rhodamine	donor-dextran (MW=70,000)/ acceptor-ConA	N/A	470 /520 nm	fluorescence intensity change	up to 200 mg/dL	demonstrated glucose sensing based on the level of FITC fluorescence in a homogeneous solution
Meadows and Schultz (1993) (108)	FITC/TRITC	donor- dextran (MW=70,000)/ acceptor-succinylated-ConA	N/A	480 /540 nm	fluorescence intensity change	detection limit was 0.05 μg/ml and glucose concentration up to 1600 mg/dl, response time was 10 mins	demonstrated reduction of aggregation and improved sensitivity of FRET system over previous study
Lakowicz and Maliwal (1993) (54)	AMCA or CB or FITC/Texas Red or TRITC/MG	donor-ConA or donor-succinylated-ConA /acceptor-mannoside or acceptor-dextran (MW=10,000)	40~65	360/435 nm, AMCA-ConA 360/430 nm, CB-ConA) 442nm , FITC-ConA 570 or 576 nm, Texas Red-ConA	frequency-domain (modulation frequency from 10 to 500 MHz)	up to 4500 mg/dL	demonstrated the use of phase-modulation measurements for glucose assays using a variety of FRET pair

Table 2.2 Continued.

Reference	Donor/ Acceptor	FRET affinity system	R_0 (Å)	λ, EX/ EM	Measurement methods/instrumentation	Glucose sensing range	Comments
Lakowicz and Szmacinski (1993) (32)	AMCA/TRITC	donor-ConA /acceptor-mannoside	42	360 nm / ~450 nm	frequency-domain at 200 MHz	up to 4500 mg/dL	qualitatively demonstrated the ability to perform lifetime measurements for glucose sensing
Tolosa *et al.* (1997) (109)	Ruthenium MLC/MG	donor-ConA /acceptor-insulin-maltose	42	488/633±40 nm	frequency-domain (modulation frequency from 10-1000 KHz)	up to 1800 mg/dL.	demonstrated the use of long lifetime dyes (average ~500ns to enable blue LED as light source
Tolosa *et al.* (1997) (51)	Cy5/MG	donor-ConA/maltose-Insulin-acceptor	35	580/620 nm	time-domain	up to 1800 mg/dL	demonstrated the use of longer wavelength dyes and red laser diodes
Ballerstadt and Schultz (1997) (52)	FITC/RITC	donor- dextran (MW=2,000k) and acceptor-Dextran	N/A	495/ 520 nm	fluorescence intensity change	up to 300 mg/mL	demonstrated a new sandwich-like affinity assay based on the use of two groups of polymers which consisted of the same type of affinity ligands but different indicator tags

Table 2.2 Continued.

Reference	Donor/ Acceptor	FRET affinity system	R_0 (Å)	λ, EX/EM	Measurement methods/instrumentation	Glucose sensing range	Comments
Russell *et al.* (1999) (40)	FITC/TRITC	donor- dextran (MW2, 000k)/ acceptor-ConA two dyes immobilized into Poly(ethylene glycol) hydrogel microspheres	N/A	488/500-660 nm	fluorescence intensity change	up to 600 mg/dL	demonstrated immobilization of FRET pair into PEG hydrogel
Rolinski *et al.* (2000, 2001,2004) (50,110,111)	APC/MG	donor-ConA/ acceptor-dextran (MW=70,000)	59.3	670/>715 nm	time-domain	up to 540 mg/dL	demonstrated a long wavelength FRET system using time-domain measurements. the distribution function was used to determine glucose concentrations
McCartney *et al.* (2001) (53)	APC/MG	donor-ConA / acceptor-dextran (MW=70,000)	59.3	650/>695 nm	time-domain	45-540 mg/dL	investigated performance in serum and interference by albumin
D'Auria *et al.* (2002) (82)	Tryptophan/o-nitrophen-β-D-glucopyranoside	*Bacillus Stearothermophilus* / o-Nitrophen-β-D-glucopyranoside (acceptor)	N/A	290/340 nm	anistropy measurement	up to 108 mg/dL	demonstrated the use of a thermostabe glucokinase and use of anisotropy measurement

Table 2.2 Continued.

Reference	Donor/ Acceptor	FRET affinity system	R_0 (Å)	λ, EX/EM	Measurement methods/instrumentation	Glucose sensing range	Comments
Arimouri *et al.* (2002) (112)	Phenanthrene/pyrene	donor-boronic acid-acceptor	N/A	299 or 342 nm/397 or 417 nm	fluorescence intensity change	N/A	demonstrated the use of a modular design approach to build an intramolecular energy transfer glucose sensor. The preliminary experiments were carried out in a basic solution (pH=8.2), glucose sensing range was not shown
Ye and Schultz (2003) (76)	GFP/YFP	donor-glucose binding protein (from *E. coli*)-acceptor	N/A	395/527 nm	fluorescence intensity	10% change over 0-0.18 mg/dL; response time less than 100s	demonstrated the use of a novel genetically engineered glucose indicator protein
Ballerstadt *et al.* (2004) (113)	AF647/QSY21	donor- dextran (MW 70,000) / acceptor- ConA-Sepharose	80	645/675 nm	ratiometric measurement	13% change over 45-270 mg/dL	demonstrated the use of a long wavelength dye and immobilized ConA within Sepharose beads
Chinnayelka and McShane (2004) (55)	FITC/TRITC	donor-dextran/accepor-ConA	55	488/ 560 nm	fluorescence intensity	27% change over 0-1800 mg/dL	demonstrated the use of layer-by-layser self assembly of dextran and ConA into polymer microparticles

Table 2.2 Continued.

Reference	Donor/ Acceptor	FRET affinity system	R_0 (Å)	λ, EX/EM	Measurement methods/instrumentation	Glucose sensing range	Comments
Chinnayelka and McShane (2005) (83)	FITC/TRITC	donor-dextran/ acceptor- apo-glucose oxidase	N/A	480/ 500-625 nm	fluorescence intensity	67% change over 0-720 mg/dL	demonstrated the use of apo-glucose oxidase and polymer microcapsule
Ibey *et al.*(2005) (114)	AF594/AF647	donor-glycodendrimer/ acceptor-ConA	N/A	610/ 610-835 nm	fluorescence intensity	67% change over 0-600 mg/dL	demonstrated the feasibility of using a glycodendrimer to replace dextran in the competitive binding system
Liang *et al.* (2005) (57)	AF568/AF647	donor-dextran/acceptor-ConA	82	568/600 nm	Frequency-domain	67% change over 0-224mg/dL	demonstrated that frequency-domain measurement can be used to extract FRET decay kinetics
Blagoi *et al.* (2005)(46)	FITC/Texas Red	donor-ConA-polystyrene particles/acceptor-dextran	N/A	470/490-700nm	Fluorescence intensity	N/A	demonstrated the use of polystyrene particles labeling with FITC-ConA for screen carbohydrates
Chinnayelka and McShane (2006)(115)	Cy5/TRITC	donor-apo-GOX/acceptor-dextran	N/A	543/560-725 nm	Fluorescence intensity	0-720 mg/dL	demonstrated the use of a long-wavelength Cy5 dye replacing previous FITC dyes

* part of the table is reproduced from Liang *et al.*(57)

2.3 ConA-dextran FRET Affinity Sensor

2.3.1 Properties of ConA and Dextran

At physiological pH, 7.4, ConA is a tetramer of four identical subunits. ConA exists as a dimer at low pH, <5.5. Each subunit (MW= 26,000) has 237 amino acid residues and one sugar binding site specific to glucose-, mannose-, and fructose-like saccharides. The cross section of each subunit in ConA is about 40×39 Å in cross section and each subunit is 42 Å high (116). The tetramer (MW= 104,000) has four independent sugar binding sites. The binding clefts are located 65 Å apart (117). Excess Mn^{2+}, Ca^{2+} (1mM) is necessary for the sugar binding ability of ConA. Table 2.3 lists the specificity of ConA to different sugar molecules. Although maltose and fructose have higher binding affinities than glucose, only glucose is presenting a significant amount in blood plasma and interstitial fluid (70-140mg/dL (118)).

Table 2.3. Association constants of some sugar molecules to ConA (49)

Sugar	K^b (L/mol)
Maltose*	2880
Fructose*	1370
Glucose#	400
Sucrose*	526
Dextran#	15000

* at pH=6.2, 2˚C

at pH=7.2, 27˚C

b $K = \frac{[ConA - sugar]}{[ConA][sugar]}$

Succinylated ConA (Succinyl-ConA) was also tested for glucose sensing studies (108). By reacting lysine residues on ConA with succinic anhydride, the resultant, Succinyl-ConA exists as a dimer in neutral environment. Changing from ConA to Succinyl-ConA did not show significant improvement in sensitivity and sensing range of glucose sensing (108,119).

There may be a toxicity concern when using ConA within *in vivo* implantable sensors because it has been found that ConA is a T-cell mitrogen (120). The lethal dose of ConA in 50% of tested animals is 41.5 mg/kg delivered intraperitoneally and 50 mg/kg delivered intravenously. In the study by Ballerstadt *et al.* (44), the amount of ConA in the implantable sensors was less than 0.12 μg/kg of body weight. For the ConA-dextran system used in this study in a 1 cm^3 implantable cubic phantom, the concentration was less than 12 μg/kg of body weight. It is reasonable to expect that the ConA-dextran system, once implanted, will pose a minimal risk to the diabetic patients, especially since ConA will be immobilized and sequestered.

Dextran is a long-chain polysaccharide with many external branches. Dextran molecular weight ranges from 3000 Da to 5,000,000 Da. Dextran is a biocompatible and biodegradable polymer that is widely used in surgery and medicine (121). The multivalent binding between dextran and ConA are still not fully understood even though some published work exists to explain this receptor-ligand interaction (122).

2.3.2 ConA-dextran Affinity System

The principle of the ConA-dextran affinity sensor is the competitive and reversible binding of ConA to dextran and glucose in solution.

Figure 2.5 illustrates the FRET effects in ConA-dextran affinity system. The following reversible reaction takes place in the sensing system:

$$ConA + glucose \underset{}{\overset{k_1}{\rightleftharpoons}} ConA\text{-}glucose \qquad (2.12)$$

(receptor) (analyte)

$$ConA + dextran \underset{}{\overset{k_2}{\rightleftharpoons}} ConA - dextran \qquad (2.13)$$

(receptor) (multivalent ligand)

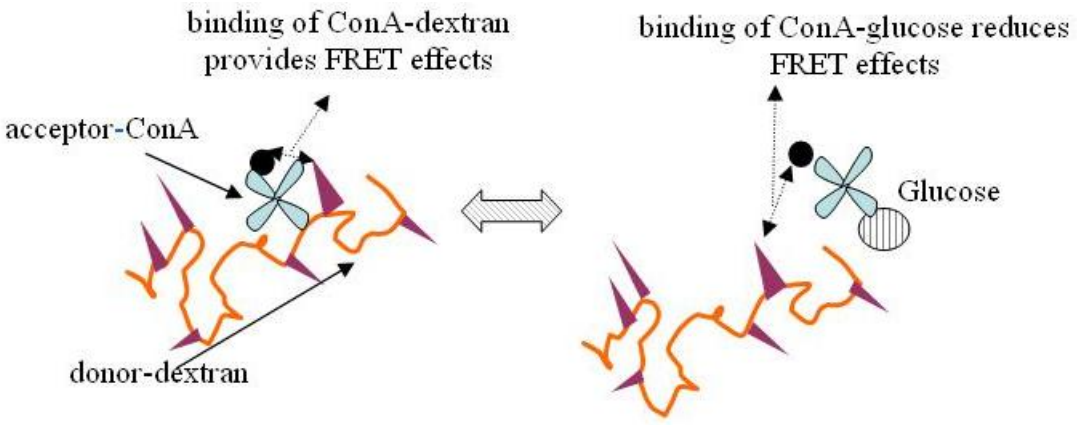

Figure 2.5. ConA-dextran affinity sensing system in presence of glucose in solution.

The first use of ConA-dextran affinity system to monitor glucose concentration was pioneered by Schultz *et al.*(48) As shown in Table 2.2, followed research by other groups focused on how to improve the sensitivity, stability, reversibility, and sensing ranging, of the system in several different ways such as: (i) changing the donor-acceptor FRET pairs (32,109); (ii) replacing the dextran with other sugar molecule or dendrimers (51,114); (iii) introducing microspheres into the system as “hosts” for the protein ConA

and dextran (40,41); (iv) applying time-resolved measurements instead of intensity measurements (50,54); and (v) carrying out *in vivo* measurements using implantable microspheres (41). This research focused on analysis of the FRET decay kinetics within the affinity system using FD measurements. Presented next are methodologies for fluorescence decay kinetics and light propagation in scattering media as a prelude to the results.

3. METHODS: FLUORESCENCE DECAY KINETICS, LIGHT PROPAGATION IN FDPM

3.1 Fluorescence Decay Kinetics with and without FRET Process

3.1.1 Fluorescence Decay Kinetics without FRET

Fluorescence decay kinetics describes the general process of fluorescence emission when fluorophores return from the excited energy states to the ground energy states. Table 3.1 provides an overview of fluorescence decay kinetics without FRET and shows that, different fluorophores follow different decay kinetics. Two-exponential decay kinetics are widely employed in fluorescence sensing systems (123). Our previous results showed that the average lifetime τ_{avg}, which could be easily extracted from experimental measurements, can be used to describe multi-exponential or stretched-exponential decay kinetics (123).

3.1.2 FRET Decay Kinetics

In a homogenous solution, the distance distribution of acceptors around a donor can be described as the probability function $\rho(r)$, where $\int_0^R \rho(r)dr$ is the number of acceptor molecules in a spherical volume of radius R.

Table 3.1. Overview of fluorescence decay kinetics model without presence of FRET in non-scattering solution. All the models are normalized to the incident intensity I_0 at time zero.

Decay kinetics	Equation	Comments	Example/ reference
Single-exponential	$I(t)_{sig} = e^{-t/\tau_0}$	the simplest decay kinetics model	DTTCI (124) ICG
Multiple-exponential	$I(t)_{mult} = \sum_{j=1}^{n} a_j e^{-t/\tau_j}$	fluorophores resides in different environments a_j is the pre-exponential factor	(26)
Two-exponential	$I(t)_{two} = a_1 e^{-t/\tau_1} + a_2 e^{-t/\tau_2}$	fluorophore molecules exist two different form in solution	SNAFL SNARF (125)
Stretched-exponential	$I(t)_{st} = e^{(-\alpha t - \beta t^{0.5})}$	fluorophore dyes are quenched by a non-fluorescent agent. α and β are functions of the diffusion coefficients of the fluorophore and quencher	collagen elastin (126,127)
Single-stretched-exponential	$I(t)_{\text{single-st}} = a_1 \exp(-t/\tau_1) + a_2 \exp(-\alpha t - \beta t^{0.5})$	potential fluorescence quenching of one fluorophore by another	(123)

If the donor fluorophore has a single lifetime, τ_0, and it follows the single-exponential decay, then in the presence of acceptors, the donor fluorescence, *I(t)*, in response to an incident excitation pulse I_0 at time zero, can be described as follows:

$$I(t) = exp\left(-t/\tau_0 - \int_0^\infty dr\rho(r)\left\{1 - exp\left[-tk_T(r)\right]\right\}\right) \tag{3.1}$$

where $k_T(r)$ is the distance-dependent energy transfer rate as defined in Equation 2.5. Combining Equation 2.5 with the above equation, the donor fluorescence can be written as follows:

$$I(t) = exp\left(-\frac{t}{\tau_o} - \int_0^\infty \rho(r)\left(1 - exp(-\left(\frac{t}{\tau_o}\right)\left(\frac{R_o}{r}\right)^6\right)\right)dr \tag{3.2}$$

To date, most FRET studies for sensing and imaging still estimate a single D-A distance and assume $\rho(r)$ is equal to unity (128). Only a few studies have provided analytical evaluation of $\rho(r)$ (34). For a random, homogenous, three-dimensional distribution of acceptors (no diffusion and very low donor concentration), the well-known Förster model predicts the time-dependent donor fluorescence, *I(t)* (26):

$$I(t) = exp\left[-t/\tau_0 - \gamma(t/\tau_0)^{1/2}\right] \tag{3.3}$$

where $\gamma = [A]/C_A$, *[A]* is the acceptor concentration and C_A is the critical acceptor concentration, $C_A = 3/\left(2\pi^{2/3}N_A R_0^3\right)$.

When the energy transfer between two donors is considered, the Huber's model modified the expression of time-dependent donor fluorescence (129):

$$I(t) = exp\left[-t/\tau_0 - (\gamma_D/\sqrt{2} + \gamma)(t/\tau_0)^{1/2}\right] \tag{3.4}$$

where $C_D = 0.135/N_A(R_0^{DD})^3$, $[D]$ is the acceptor concentration, and C_D is the critical donor concentration, $\gamma_D = [D]/C_D$. R_0^{DD} is the critical energy transfer distance for donor-donor energy transfer.

Gosele and Hausers' model considered the diffusion of donor and acceptor molecules in solution and resulting in the following expressions for time-dependent donor fluorescence (130):

$$I(t) = exp\left[-t/\tau_0 - 4\pi D r^*[A]N_A t - \gamma(t/\tau_0)^{1/2}\right] \qquad r^* > r_{DA} \tag{3.5}$$

$$I(t) = exp\left[-t/\tau_0 - 4\pi D r_{DA}[A]N_A t - 8r_{DA}^2[A]N_A(\pi D t)^{1/2}\right] \qquad r^* < r_{DA} \tag{3.6}$$

where D is the sum of diffusion coefficients of the acceptor and donor molecules; r^* is the interaction radius; and r_{AD} is the collision distance.

In solid and liquid media where the donor and acceptors are embedded in restricted geometries, Klafter and Blumen proposed a 3D fractal FRET decay model (131):

$$I(t) = exp\left[-t/\tau_0 - B(t/\tau_0)^{1/2}\right] \tag{3.7}$$

where B is a time-dependent factor. All these derived models can be summarized as a generalized Förster model as shown in Table 3.2:

$$I(t) = exp\left[-\frac{1}{\alpha}t - 2\gamma\left(\frac{1}{\alpha}t\right)^{\beta}\right] \tag{3.8}$$

where α (ns) is the unquenched lifetime of the donor, and the parameter β is related to dimensionality of the affinity system (1/2 for three dimensional and 1/3 for two dimensional systems).

Table 3.2. Summary of FRET decay kinetics models in homogenous, non-scattering medium.

FRET decay model	Description	α	2γ	β
Förster (26)	3D, no diffusion, homogeneous	τ_0	γ	1/2 or 1/3
Huber (129)	Donor-donor energy transfer was also considered	τ_0	$\left(\gamma_D/\sqrt{2}+\gamma\right)$	1/2
Gösele (130)	Added donor-acceptor diffusion influence	τ_0	N/A	1/2
			N/A	1/2
Blumen and Klafter (131)	Solid or liquid, condensed media	τ_0	B	1/2

Rolinski *et al*. recently pioneered an approach to invert Equation 3.1 in order to determine the D-A distance distribution function (102,110,111,132). They transformed Equation 3.1 into a Fredholm equation and solved for the D-A distribution subject to the constraint that the distance between the D-A pair cannot be less than that allowable by their molecular structures. They expanded the unknown $\rho(r)$ into a finite series (as shown in Equation 3.9) of orthonormal Laguerre polynomials and optimized the solution for the coefficient of the polynomial which provides the best fit to $I(t)$ from time-domain measurements (133).

$$\rho(r)=\begin{cases} 0 & 0\le r\le d \\ R_0^{-1}\sum_{i=0}^{\infty} a_i^s L_i^s\left(r/R_0\right) & r\ge d \end{cases} \tag{3.9}$$

where $L_i^s(r/R_0)$ is the infinite series of orthonormal Laguerro polynomials and a_i^s are the coefficients. The parameter *d* is the minimum donor-acceptor distance.

Using time-domain measurements, Rolinski *et al.* showed that the distribution function can be used to monitor glucose concentration in a solution-based FRET system of APC and MG (134,135). Recently they compared $\rho(r)$ from APC-MG FRET system with rhodamine 123-MG FRET system (110). The two systems have similar Förster distances but different molecule sizes and therefore should have different $\rho(r)$. However their simulated ρ(r) from time-domain experiments showed similar trends in both systems. The discrepancy between simulation results and biophysical theory indicates more work should be done in the future to improve the inverse solution technique.

3.2 Measurement of Fluorescence Decay Kinetics with or without FRET

Fluorescence decay kinetics can be measured using one of three broad classes of measurements: (i) continuous wave (CW); (ii) time-domain measurements which involve a pulse of excitation light; or (iii) FD measurements which involve a modulated light. The latter two measurements are shown in Figure 3.1 and consist of monitoring the time-response of the fluorescence emission.

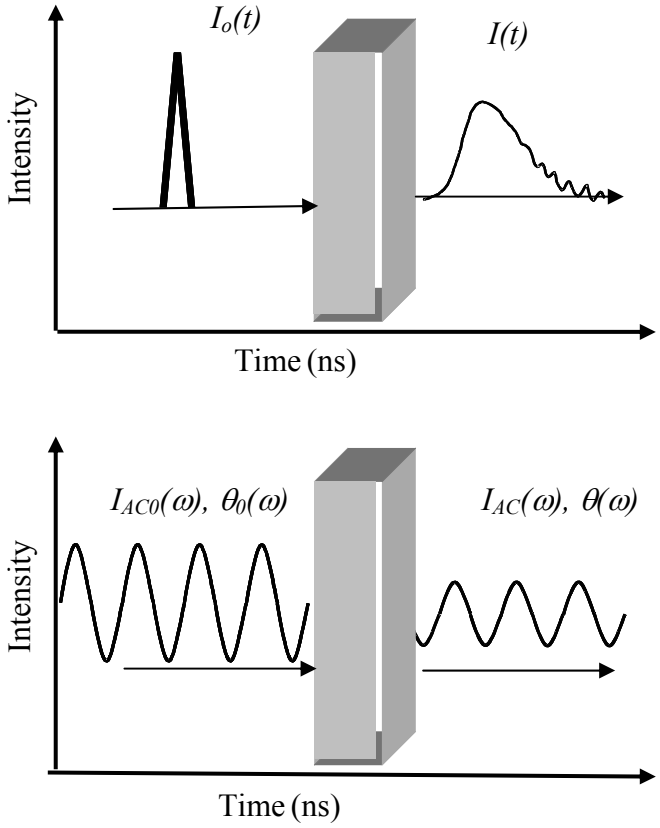

Figure 3.1. Illustration of time-domain (upper figure) and FD (lower figure) to measure fluorescence decay kinetics with or without the presence of FRET.

In time-domain measurements, a pulse of excitation light contacts the sample and the pulse generating a fluorescence light which is recorded, and whose width indicates the distribution of activated states. Typically the measurement of *I(t)* can be fit to one of a number of decay kinetics models as discussed above. Difficulties with time-domain measurements involve: (i) a reduced signal to noise ratio (SNR) in the fluorescence detected; and (ii) long data acquisition time. FD approaches represent a time-resolved measurement conducted in frequency-space. Intensity modulated excitation light produces fluorescent light modulated at the same frequency as the incident excitation light, but phase-shifted and amplitude attenuated relative to the incident light. Upon conducting measurements across a range of modulation frequencies (kHz – GHz), the same temporal information obtained from time-domain techniques can be achieved using FD or "phase-modulation" approaches. The drawback to conventional phase modulation approaches is the need for a "reference" dye in order to accurately report the phase-delay independent of instrument responses (32). The advantage of conducting time-dependent measurements, whether in time- or frequency-domains, is that they are independent of the amount of fluorophore present, thereby enabling an accurate sensing approach for fluorescence decay kinetics without the issue of fluorophore loading. However, without proper analysis of time-dependent measurements, the presence of tissue-like scattering creates a photon "time-of-flight" which impacts the phase and amplitude of FD measurements as well as the breadth of the re-emitted fluorescence pulse in time-domain measurements. Previous research in our group has demonstrated that the presence of scattering can be properly taken into account and eliminate the need for a "reference"

measurement using conventional phase modulation approaches (30,123). In this research, we used FD measurement to analysis the FRET decay kinetics. A more rigorous discussion of FD measurement is provided in section 3.3

3.3 Decay Kinetics Analysis in Non-scattering and Scattering Solutions

3.3.1 Decay Kinetics Analysis in Non-scattering Solutions

Frequency-domain fluorescence lifetime measurement in non-scattering solution involves: (i) excitation of a fluorophore by a light source whose intensity is modulated at frequency ω, and (ii) detection of the resulting fluorescence light perpendicular to the incident light. Figure 3.2 (a) illustrates the physical process of FD measurement of decay kinetics in dilute, non-scattering solution. In dilute solution, the measured fluorescence phase shift (θ) and modulation ($M = \frac{ac(\omega)}{dc(\omega)} \Big/ \frac{AC(\omega)}{DC(\omega)}$) relative to the source are functions of the fluorophore decay kinetics model. Here are three situations:

(1) For fluorophores which follow single-exponential decay kinetics as shown in Table 3.1, the phase shift and modulation can be directly related with fluorophore lifetime as shown:

$$\theta_M = arctan(\omega\tau) \tag{3.10}$$

$$M_M = 1/\sqrt{1+(\omega\tau)^2} \tag{3.11}$$

where ω is the modulation frequency (usually in MHz); τ is the lifetime of the fluorophore (usually several nanoseconds). In the experiment, the choice of modulation frequency is very important for choosing RF frequency synthesizer. As shown in Figure 3.3, for lifetime change from 1.0 to 0.5 ns (e.g. Cy5 dye), the useful frequency range can be from 30 MHz to 1000 MHz. For lifetime change from 10 ns to 20 ns, the useful frequency range will be from 0 MHz to 100 MHz. In my research, the fluorophore we used are (1) pH sensitive C-SNAFL-1 with lifetime 3.65 ns at pH = 7.0 (136); and (2) AF568 with lifetime 3.6 ns (57). Therefore the suitable modulation frequency range is within 0-200 MHz.

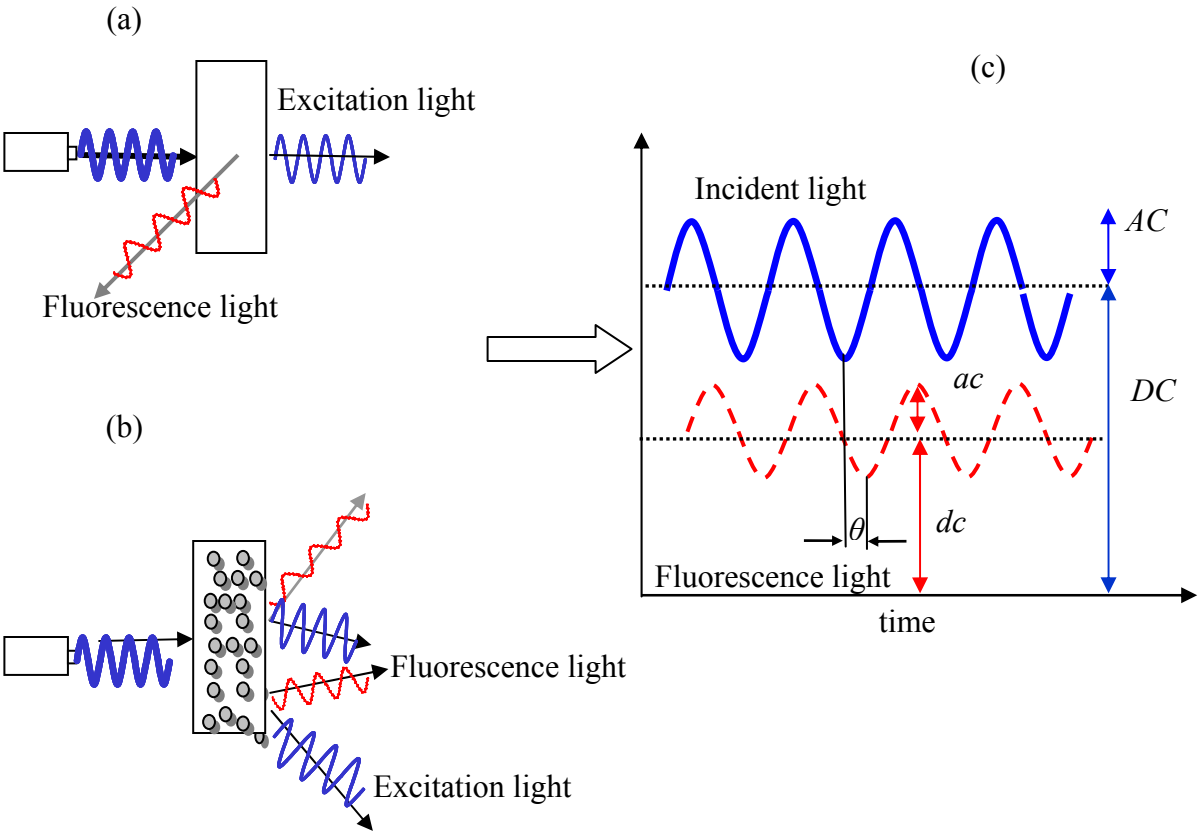

Figure 3.2. Frequency-domain lifetime measurement in (a) non-scattering solution; and (b) scattering solution. Figure (c) illustrates the amplitude attenuation *AC/ac*, phase shift θ, and the mean intensity *DC/dc*.

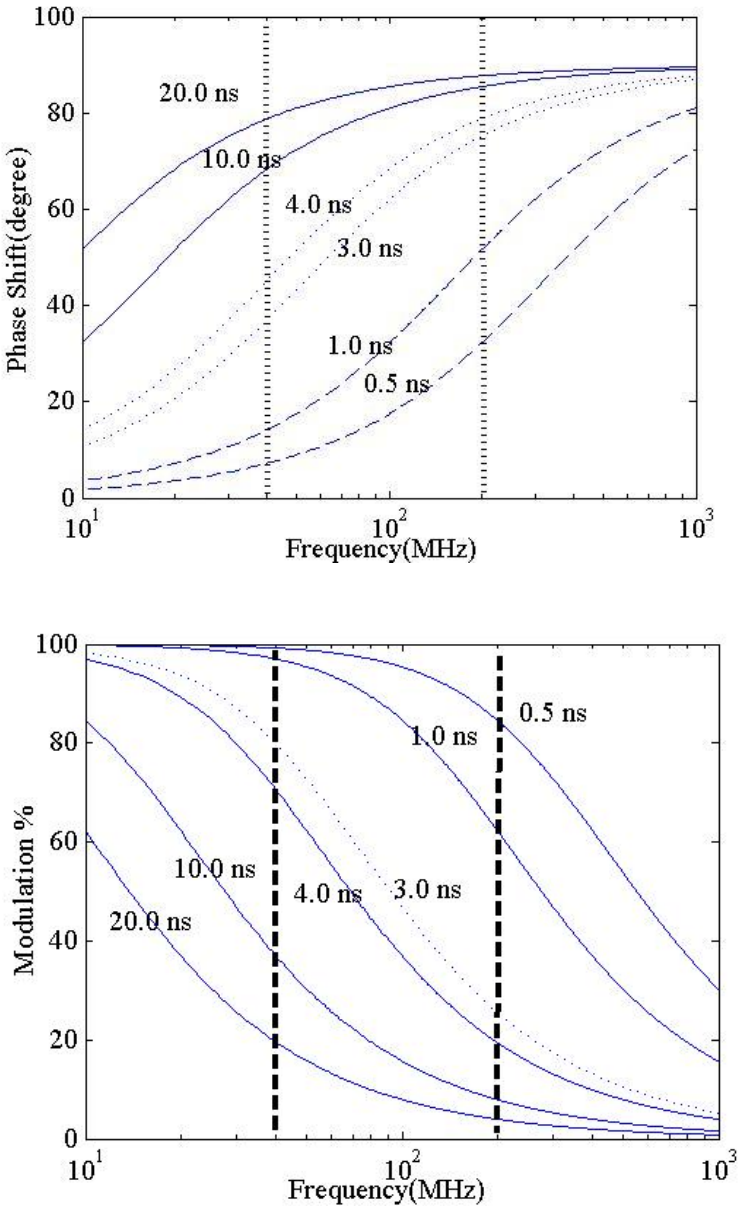

Figure 3.3. Phase shift change (upper figure) as the function of modulation frequency at different fluorescence lifetimes. Modulation (lower figure) as the function of modulation frequency at different fluorophore lifetimes. The two figures come from simulation results of Equation 3.10 and 3.11.

(2) For fluorophore which follows multi- or stretched- exponential decay kinetics as shown in Table 3.1, the measured phase shift and modulation can related to the lifetime as shown in the following equations:

$$N(\omega) = \frac{\int_0^\infty I(t)\sin(\omega t)dt}{\int_0^\infty I(t)dt} \tag{3.12}$$

$$P(\omega) = \frac{\int_0^\infty I(t)\cos(\omega t)dt}{\int_0^\infty I(t)dt} \tag{3.13}$$

$$\theta_M(\omega) = arctan\left[\frac{N(\omega)}{P(\omega)}\right] \tag{3.14}$$

$$M_M(\omega) = \sqrt{\left(N(\omega)^2 + P(\omega)^2\right)} \tag{3.15}$$

where $N(\omega)$ is the imaginary part of Fourier transform of the decay kinetics, $I(t)$ and the $P(\omega)$ is the real part of the Fourier transform. The phase-shift and modulation ratio can be related to those unknown parameters in decay kinetics models through $N(\omega)$ and $P(\omega)$. Those unknown parameters can be determined from the best fit between model predicted values ($\theta_p(\omega)$ and $M_p(\omega)$) and experimental measured ($\theta_M(\omega)$ and $M_M(\omega)$) as indicated by χ^2,

$$\chi^2 = \frac{1}{\nu}\left\{\sum\left(\frac{\theta_M(\omega) - \theta_p(\omega)}{\delta\theta}\right)^2 + \sum\left(\frac{M_M(\omega) - M_p(\omega)}{\delta M}\right)^2\right\} \tag{3.16}$$

where $\delta\theta$ and δM are the estimated uncertainties in the phase shift and modulation results at each modulation frequency. The value of χ^2 is expected to be close to one for the

correct model, and depending upon the estimated $\delta\theta$ and δM (26). In this research, the MatLab optimization toolbox (The Mathworks Inc., Natick, MA) was used to minimize χ^2.

(3) For fluorophores which follow FRET decay kinetics model, e.g. ConA-dextran affinity glucose sensing system, a generalized Förster model shown in Equation 3.8 is applied by taking a Fourier transform of Equation 3.8 as shown in Equation 3.17,

$$F(\omega)=\int_0^\infty I(t)\exp(i\omega t)dt=\int_0^\infty \exp\left[-\frac{1}{\alpha}t-2\gamma\left(\frac{1}{\alpha}t\right)^\beta+i\omega t\right]dt \tag{3.17}$$

The $\theta(\omega)$ and $M(\omega)$ can be obtained from $F(\omega)$ as:

$$\theta_P(\omega)=arctan\left\{\frac{IMAG[F(\omega)]}{REAL[F(\omega)]}\right\} \tag{3.18}$$

$$M_p(\omega)=\sqrt{\left(IMAG[F(\omega)]\right)^2+\left(REAL[F(\omega)]\right)^2} \tag{3.19}$$

The parameters of α, β, and γ can be determined from the best fit between model predicted values ($\theta_p(\omega)$ and $M_p(\omega)$) and experimental values ($\theta_M(\omega)$ and $M_M(\omega)$) as indicated by χ^2.

3.3.2 Decay Kinetics Analysis in Scattering Solution

As illustrated in Figure 3.2 (b), fluorescence measurements in the presence of tissue-like scattering need to take into account: (i) the propagation of excitation light, (ii) the fluorescence lifetime of the dye, and (iii) the propagation of the fluorescence light emitted by the dye before being detected. Therefore, the detected phase-shift and modulation ($\theta_M(\omega)$ and $M_M(\omega)$) depend upon the medium optical properties (μ_s' and μ_a) as well as the fluorescent decay kinetics. Previously we successfully employed the diffusion approximation to the radiative transfer equation to predict the fluorescence photon density measured with FD techniques (30,58,123,124,136). The details of the optical diffusion equation, the generated fluorescence photon density, and the relationships between the photon-density and the measurable quantities (θ_M and M_M) have been discussed in the previous papers (30,124,137). Below, a brief synopsis is provided.

3.3.2.1 Optical Diffusion Equation and Generated Fluorescence Photon Density

When light launches onto scattering solutions or tissue surface, the propagation of light is attenuated and scattered due to sample scattering and absorption. When photons of excitation light activate the fluorophores inside the sample, the generated fluorescence light is again attenuated and scattered due to the scattering and absorption of the sample. Figure 3.4 illustrates this physical process.

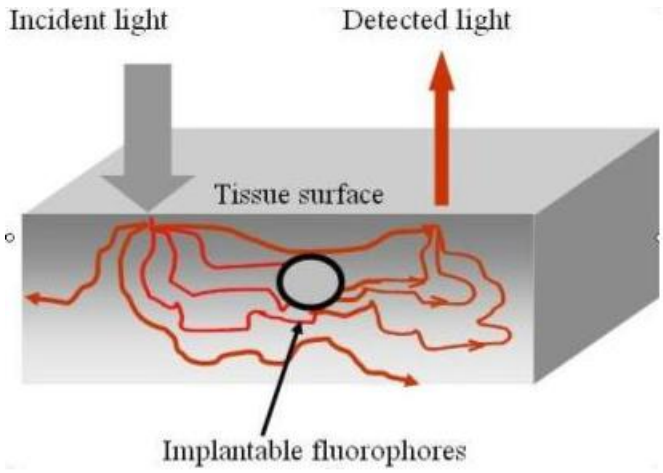

Figure 3.4. Illustration of fluorescence light propagation in scattering media. When scattered photons of the excitation light hit the fluorophores, the generated fluorescence light is again attenuated and scattered by the scattering media.

The following two coupled optical diffusion equation can be used to describe for the propagation of fluorescence light for a homogenous scattering media:

$$-D_x\nabla^2 U_x(\mathrm{r},\omega)+\left(\mu_{ax}+\frac{i\omega}{v}\right)U_x(\mathrm{r},\omega)=S_x(\mathrm{r},\omega) \tag{3.20}$$

$$-D_m\nabla^2 U_m(\mathrm{r},\omega)+\left(\mu_{\mathrm{am}}+\frac{\mathrm{i}\omega}{v}\right)U_m(\mathrm{r},\omega)=S_m(\mathrm{r},\omega) \tag{3.21}$$

Where the subscript $_x$ represents the excitation and the subscript $_m$ represents the emission. Accordingly μ_{ax} is the absorption coefficient at the excitation wavelength. μ_{am} is the absorption coefficient at the emission wavelength. μ_{axf} is the absorption coefficient owing to fluorophores at the excitation wavelength. v is the speed of light in the solution, $v=\frac{c}{n}$, n is the refractive index of the medium. D is the diffusion coefficient which is related to the isotropic scattering coefficient μ_s' and absorption coefficient μ_a,

through the relationship: $D = \left[3\left(\mu_a + \mu_s'\right)\right]^{-1}$. The diffusion coefficients at the excitation and emission wavelength are denoted by D_x and the D_m respectively. $S_x(r,\omega)$ is the excitation source term. $S_m(r,\omega)$ is the emission source term due to the generation of fluorescent photons based on the excitation photon density $U_x(r,\omega)$ weighted by fluorescence decay kinetics. $U_m(r,\omega)$ is generated fluorescence photon-density. The emission source in frequency domain for single, multi-, and stretched exponential decay kinetics and FRET exponential decay are:

$$S_m(r,\omega) = v\mu_{afx}\frac{1}{1-i\omega\tau}U_x(r,\omega)Q\zeta_m \tag{3.22}$$

$$S_m(r,\omega) = v\mu_{afx}\left(\sum_j \frac{a_j}{1-i\omega\tau_j}\right)U_x(r,\omega)Q\zeta_m \tag{3.23}$$

$$S_m(r,\omega) = v\mu_{afx}\left(\int_0^\infty I(t)_{st-\exp} exp(iwt)dt\right)U_x(r,\omega)Q\zeta_m \tag{3.24}$$

$$S_m(r,\omega) = v\mu_{afx}\left(\int_0^\infty exp\left[-\frac{1}{\alpha}t - 2\gamma\left(\frac{1}{\alpha}t\right)^\beta + i\omega t\right]dt\right)U_x(r,\omega)Q\zeta_m \tag{3.25}$$

where ζ_m is the detection efficiency factor of the system at the emission wavelength (which contains the system spectral response and the fluorophore spectral emission efficiency (30)). Q is the quantum efficiency of the fluorophore.

Upon using Equations 3.22-3.25, the generated fluorescence photon-density $U_m(r,\omega)$ can then be solved for single, multi- and stretched-exponential, and FRET decay kinetics in an infinite scattering medium:

$$U_{m,single}(r,\omega)=\frac{\mu_{afx}Q\xi_m S(\omega)}{4\pi\nu D_x D_m r}\left[\frac{1}{1+(\omega\tau)^2}\right]\{[A-B\omega\tau]+i[B+A\omega\tau]\} \tag{3.26}$$

$$U_{m,multi}(r,\omega)=\frac{\mu_{afx}Q\xi_m S(\omega)}{4\pi\nu D_x D_m r}\left\{(A+iB)\left(\sum_j \frac{a_j}{1-iw\tau_j}\right)\right\} \tag{3.27}$$

$$U_{m,stretched}(r,\omega)=\frac{\mu_{afx}Q\xi_m S(\omega)}{4\pi\nu D_x D_m r}\{(A+iB)\}\int_0^\infty\left(I(t)_{st-exp}exp(i\omega t)dt\right) \tag{3.28}$$

$$U_{m.FRET}(r,\omega)=\frac{\mu_{afx}Q\xi_m S(\omega)}{4\pi\nu D_x D_m r}\{(A+iB)\}\int_0^\infty\left(exp\left(-\frac{1}{\alpha}t-2\gamma\left(\frac{t}{\alpha}\right)^\beta+i\omega t\right)dt\right) \tag{3.29}$$

where $S(\omega)$ is the source strength (in photons per second). i is a complex number ($i=\sqrt{-1}$). The terms A and B are functions of optical properties (μ_{sx}', μ_{ax}, μ_{sm}' and μ_{am}), ν and ω (30,137).

$$A(r,\omega)=\frac{\eta(r,\omega)\xi+\zeta(r,\omega)\rho(\omega)}{\xi^2+[\rho(\omega)]^2} \tag{3.30}$$

$$B(r,\omega)=\frac{\zeta(r,\omega)\xi-\eta(r,\omega)\rho(\omega)}{\xi^2+[\rho(\omega)]^2} \tag{3.31}$$

$$\eta(r,\omega)=exp[-\beta_x(\omega)r]cos[\gamma_x(\omega)r]-exp[-\beta_m(\omega)r]cos[\gamma_m(\omega)r] \tag{3.32}$$

$$\zeta(r,\omega)=exp[-\beta_x(\omega)r]sin[\gamma_x(\omega)r]-exp[-\beta_m(\omega)r]sin[\gamma_m(\omega)r] \tag{3.33}$$

$$\xi = \frac{\mu_{am}}{D_m} - \frac{\mu_{ax}}{D_x} \tag{3.34}$$

$$\rho(\omega) = -\frac{\omega(D_x - D_m)}{\nu D_x D_m} \tag{3.35}$$

3.3.2.2 Relationships between Photon Density and Measurable Quantities (θ_M and m_M)

For fluorophores undergoing single-exponential decay kinetics, the relationship between fluorescence photon-density to the measured phase shift, θ_M, and modulation ratio M_M, are shown in the following Equations 3.36 and 3.37. For fluorophores undergoing multi-exponential, the measured phase shift, θ_M, and modulation ratio, M_M, are shown in following Equation 3.38 and 3.39.

$$\theta_{M,single}(r,\omega) = arctan\left[\frac{B + A\omega\tau}{A - B\omega\tau}\right] \tag{3.36}$$

$$m_{M,single}(r,\omega) = \sqrt{\frac{\left(\left(A - B\omega\tau\right)^2 + \left(B + A\omega\tau\right)^2\right)}{A}} \tag{3.37}$$

$$\theta_{M,multi}(r,\omega) = arctan\left(\frac{B\sum_j \frac{a_j}{1+\omega^2\tau_j{}^2} + A\sum_j \frac{a_j\omega\tau_j}{1+\omega^2\tau_j{}^2}}{A\sum_j \frac{a_j}{1+\omega^2\tau_j{}^2} - B\sum_j \frac{a_j\omega\tau_j}{1+\omega^2\tau_j{}^2}}\right) \tag{3.38}$$

$$m_{M,multi}(r,\omega) = \frac{\left\{\left[A\sum_j \frac{a_j}{1+\omega^2\tau_j{}^2} - B\sum_j \frac{a_j\omega\tau_j}{1+\omega^2\tau_j{}^2}\right]^2 + \left[B\sum_j \frac{a_j}{1+\omega^2\tau_j{}^2} + A\sum_j \frac{a_j\omega\tau_j}{1+\omega^2\tau_j{}^2}\right]^2\right\}^{\frac{1}{2}}}{A}$$

(3.39)

For fluorophores exhibiting stretched-exponential or FRET decay kinetics, numerical integration is needed to evaluate the integral in both equations 3.28 and 3.29.

The relationship between fluorescence photon-density to the measured phase shift θ_M and modulation ratio M_M can be obtained by substitution of equations 3.28 and 3.29 into equations 3.18 and 3.19.

4. MEASUREMENTS OF FRET IN A GLUCOSE-SENSITIVE AFFINITY SYSTEM WITH FREQUENCY-DOMAIN LIFETIME SPECTROSCOPY*

4.1 Introduction

Most quantitative measurements of FRET optical glucose sensors utilize intensity-based methods (24,40,44,48,52). Unfortunately, intensity measurements are functions of not only glucose concentration, but also of fluorophore concentration. The measurement of intensity may also be influenced by photobleaching as well as instrumentation response function. Furthermore, when used within tissues for in vivo sensing, the attenuation of intensity depends upon the varying optical properties of the tissue. As a consequence, intensity-based measurements of FRET for a clinically relevant and implantable glucose sensor would require frequent *in situ* calibrations (24). As an alternative method, time-dependent measurement techniques offer an opportunity to assess FRET affects not simply from the amount of light collected, but from the temporal decay kinetics. Both time- and frequency-domain fluorescence lifetime spectroscopy approaches enable direct time assessment of decay kinetics but both can also be impacted by photon "time-of-flight" in tissues.

* Part of this section is reproduced from "Measurements of FRET in a glucose-sensitive affinity system with frequency-domain lifetime spectroscopy," by Feng Liang, Tianshu Pan, and Eva Sevick-Muraca, *Photochemistry and Photobiology*, 2005, 81, 1386-1394. with the permission of the American Society for Photobiology.

Previously, we and others have demonstrated the ability to measure simple decay kinetics using frequency-domain approaches to assess the lifetime of fluorophores in tissue-like scattering solutions (30,123,124,136,137) as well as of fluorophores immobilized within hydrogels (58). The framework for extracting fluorophore decay kinetics from multiple scattered light is found in references (30,123,124,136,137). Yet to date, there have been no reports to extend quantitative, time-dependent FRET sensing under conditions of tissue-like scattering. There are, however, few reports in the literature which employ time-dependent techniques to monitor FRET of the ConA dextran affinity system in scatter-free solutions (50,53,132).

In the first use of time dependent measurements for FRET sensing found in the literature, Lakowicz and Maliwal (54) employed frequency-domain measurement of phase-shift to infer FRET changes associated with glucose binding to ConA. Using time-domain methods and a two-exponential decay model, Tolosa *et al*. (51) subsequently measured the average lifetime change in order to assess glucose concentration changes. Using the red-shifted FRET pair system interrogated with time domain measurements, Rolinski and his coworkers (50,53,102,110,111,132,138) used a Förster-type equation in order to extract the changes in the distribution of donor-acceptor distances as a function of glucose concentration and as a direct measure of the competitive binding between ConA and dextran. Their results represented the first use of time-dependent measurements to directly elucidate physical parameters which govern FRET decay kinetics.

In this work, we seek to apply FRET sensing using frequency-domain approaches in order to relate parameters from a Förster-type equation in a scatter-free medium for validation of the donor/acceptor ConA/dextran affinity system for characterization of competitive glucose binding prior to its immobilization for implantation in tissues. To date, FRET decay kinetics of the ConA/dextran affinity system have not been quantitatively analyzed from frequency-domain measurements. In the following, we first describe the affinity system, measurement approach, and decay kinetic analyses from frequency-domain measurements and then compare our results with those using time-domain measurements reported in the literature.

4.2 Materials and Methods

4.2.1 Donor-dextran/acceptor-ConA Affinity System.

The protein, ConA, conjugated with AF647 at a labeling ratio of 2.8, was purchased from Molecular Probes (Eugene, OR). MOPS (0.1 M, pH = 7.4) buffer consisting of 1mM Mn^{2+}, Ca^{2+}, and 2mM NaN_3 was used to dissolve the acceptor-ConA conjugate as it has been shown that Mn^{2+} and Ca^{2+} need to be present in the ConA solution to maintain the saccharide binding properties (139). The acceptor-ConA solution was then centrifuged to remove precipitates. The final acceptor-ConA concentration was determined by subtracting the weight of precipitate from the total weight of ConA. D-glucose (Sigma-Aldrich, St. Louis, MO) was dissolved into MOPS buffer solution at the concentration of 300 mg/mL and stored prior to experiments.

Amino dextran (MW 2 000 000; Helix Research Company, Springfield, OR) and AF568 carboxylic acid with succinimidyl ester (Molecular Probes, Eugene, OR) were conjugated following the Inman method (140). Briefly, prior to incubation of dextran with AF568 succinimidyl ester, 10 mg amino dextran was dissolved in 0.4 mL sodium bicarbonate buffer (pH = 8.3) and then vortexed continuously for 5 mins. AF 568 (1 mg) was dissolved in 0.1 mL DMSO (dimethyl sulfoxide, Sigma-Aldrich, St. Louis, MO) and then mixed with dextran solution. After 4 hrs incubation, the resulting conjugate was separated from the unreacted dye by overnight dialysis using Slide-A-Lyzer™ dialysis cassette (MWCO = 3 000; Pierce Inc. Rockford, IL). The AF568 to dextran ratio was demonstrated to be between 66 and 68 on the basis of the known dextran concentration, the assumption of 15% loss of dextran, and the AF568 excitation spectra. For simplification, in the remainder of this contribution, the dextran-donor or acceptor-ConA concentrations are denoted on the basis of moles of dextran or ConA.

4.2.2 Excitation and Emission Spectra.

Steady-state fluorescence measurements were made using a SPEX Fluorolog II spectrofluormeter (HORIBA Jobin Yvon Inc. Edison, NJ). The excitation wavelength was 568 nm and emission was collected from 588 nm to 720 nm in 2 nm increments and with a 1 sec integration time. The sample solution was held in semi-micro cells (Starna Cells Inc., Atascadero, CA) with right-angle observation and central illumination.

4.2.3 Frequency-domain Lifetime Spectroscopy Measurements.

Lifetime measurements were conducted with a frequency-domain lifetime spectroscopy system previously described (30,136). Briefly, a continuous wave (CW) light (568 nm) from a wavelength tunable Ar-Kr mixed gas laser (model 643, Melles Griot, Boulder, CO) was modulated by an external electro-optic modulator (EOM) (model 350-160, Conoptics, Danbury, CT). The photodetectors were two photomultiplier tubes (PMT, model H6573, Hamamatsu, Tokyo, Japan) that were gain-modulated by an amplified RF signal from a master frequency synthesizer (PTS310, PTS Inc., Littleton, MA). The master frequency synthesizer was phase locked to another slave frequency synthesizer (Marconi Instruments Signal Generator 2022A, Mountain View, CA) which drove the EOM at the same frequency plus an offset of 100 Hz for heterodyne detection. A portion of the incident excitation light was directed to a reference PMT which was outfitted with a long pass filter (LPF550, CVI laser, Albuquerque, NM) which slightly improved the measurement of the reference excitation signal. The sample PMT was outfitted with long pass filter (LPF500, CVI laser) and band-pass filter (600 nm, 8 nm FWHM, CVI laser) to collect the fluorescence light from the sample. For each sample of varying acceptor-ConA or glucose concentration, the phase-shift and modulation-ratio were taken at the sample PMT as a function of modulation frequency (45 to 135 MHz) and reported relative to the reference PMT. For the fluorophores employed, the useful modulation frequency range of 35-145 MHz enabled collection of sufficient data for evaluation of decay kinetics (30). The reference fluorophore of AF568 (with lifetime of 3.6 ns (141)) was used to correct the

instrumentation response function according to the methods described elsewhere (123). We measured the lifetime of free and conjugated AF568 and found that the AF568 lifetime remained constant at 3.6 nsec and was unchanged with conjugation.

4.2.4 Optimization of FRET Affinity System.

One of the advantages of the ConA-dextran system is the flexibility of (i) measuring either donor or acceptor emission, (ii) changing the donor-dextran concentration; and (iii) changing the acceptor-ConA concentration in order to change the sensitivity and sensing range (48,52,108). To optimize the AF568/AF647 dextran-ConA FRET system for maximum sensitivity to glucose concentrations ranging from 0 to 200 mg/dL and sensing range up to 700 mg/dL, we (i) evaluated changes in donor-dextran and acceptor-ConA fluorescence intensities as a function of glucose concentration up to 500 mg/dL in order to choose the most sensitive FRET measurement wavelength for monitoring changes in glucose, and once determined, (ii) assessed its emission intensity as a function of concentration in order to maximize measurement sensitivity and minimize attenuation owing to inner filter effects. Next, at the optimal concentration of the conjugated FRET dye, we evaluated the most sensitive concentration of the corresponding conjugated FRET dye needed to achieve the desired sensing range and sensitivity by monitoring the changes in phase-shift from frequency-domain lifetime spectroscopy. From all of these intensity and frequency-domain measurements, we determined the optimal emission wavelength as well as the optimal donor-dextran and acceptor-ConA concentrations for evaluating the FRET decay kinetics as described below.

4.2.5 Evaluations of FRET Decay Kinetics from Frequency-domain Measurement.

At the optimal donor-dextran concentration determined from the above procedures, aliquots of 46.24 μM acceptor-ConA solution were added in six increments to render the final optimal acceptor-ConA concentration determined from the above procedures. Thirty seconds after each aliquot addition, frequency-domain fluorescence lifetime measurements were conducted. Measurements were performed with duplicate samples and each measurement was conducted 4 times on each sample.

At the optimal donor-dextran and acceptor-ConA concentrations, aliquots of 300 mg/dL glucose solution were added in five increments to render a final glucose concentration of 224 mg/dL. Thirty seconds after each aliquot addition of glucose, frequency-domain fluorescence lifetime measurements were conducted. Measurements were performed with duplicate samples and each measurement was conducted 4 times on each sample.

In this study, we assumed FRET decay kinetics model follows the generalized Förster model as shown in Equation 3.8. By taking the Fourier transform of Equation 3.8 and taking the real and imaginary parts to predict the frequency-domain measurements of phase and amplitude modulation (26), the measurements can be related in terms of a function of α, β, and γ. These parameters were determined from the best fit between model predicted values (θ_P and M_P) and experimental values (θ_M and M_M) as indicated by χ^2 (142).

While Equation 3.8 was used to evaluate the FRET decay kinetics, we also evaluated the FRET changes in terms of an average lifetime, τ_{avg} (30).

4.3 Results

4.3.1 Donor and Acceptor Characterization

Figure 4.1 illustrates the excitation and emission spectra for the AF568 and the absorption and emission spectra for AF647 dye pairs. The Förster distance for the dye pair is 82 Å (141) and is larger than that for all other dye pairs previously reported in literature (4,5,10) as shown in Table 4.1. In addition, the molecular weight of both AF568 and AF674 is less than 1300 Da and more consistent with the "point dipole" assumption of Förster theory (99) than that of other studies employing high molecular weight dye pairs found in the literature (110,138). Finally, we found the Alexa Fluor dyes to be most photo-stable and pH insensitive, with good solubility in aqueous solutions (141). Table 4.1 presents the fluorescence properties of the AF568/AF647 donor-acceptor pair.

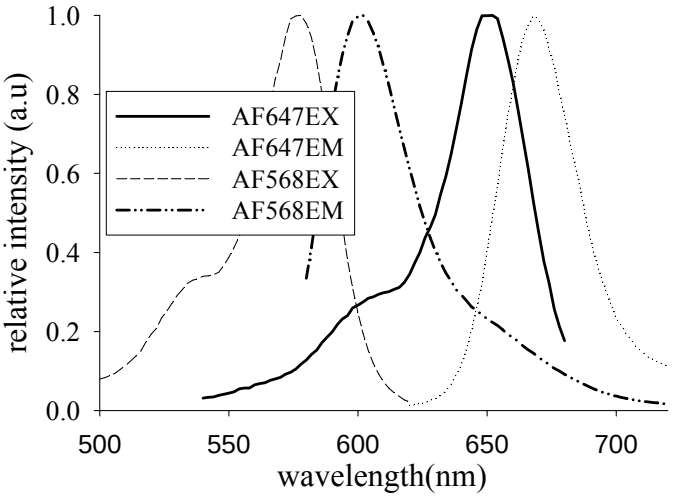

Figure 4.1. Normalized excitation (dashed line) and fluorescence (dashed dotted line) spectra of AF568-dextran (donor-dextran) and the normalized absorption (solid line) and fluorescence (dotted line) spectra of AF647-ConA (acceptor-ConA). For clarification and simplification, the donor or acceptor concentrations were denoted as the concentration of dextran or ConA in the entire dissertation.

Table 4.1. Fluorescence properties for different donor-acceptor FRET pairs used in our experiments and other literature:

D-A Pairs	Ex/Em(nm)	ϵ ($M^{-1}cm^{-1}$, peak value)[e]	τ (ns)	MW	R_0 (Å)	Labeling ratio
AF633 (D)	632/646	159000	3.2[d]	1200[e]	73[a]	1.6:1 = D: Con A
QSY21 (A)	704/NA	89600	NA	815[e]		6.1 = A: dextran
AF568 (D)	578/602	88,000	3.6[d]	791[e]	82[a]	66:1 = D: dextran
AF647 (A)	649/666	250,000	1.4[d]	1300[e]		2.8:1 = A: Con A
Cy5 (D)	646/664[b]	2.5×10^5	1.4[b]	1200[b]	35[b]	1:1 = D: Con A[b]
MIMG (A)	584/NA[b]	30,000	NA	NA		1.5: 1 =A: dextran[b]
APC (D)	650/670	2.4×10^6	1.8[c]	104,000[c]	59[c]	1.1:1 = D: Con A[c]
MG (A)	620/NA[c]	78500	NA	485[e]		1:1=A: dextran[b]
AF647 (D)	649/666	250000	1.4[d]	~1400[e]	80[a]	NA
QSY21 (A)	704/NA	89600	NA	815[e]		NA

[a] used PhotochemCAD software; [b]data were provided by Tolosa *et al.* (51);[c]data were provided by Rolinski *et al.* (50); [d]lifetime data were provided by Molecular Probes Inc; [e]extinction coefficient and molecular weight data were provided by Molecular Probes Inc. (141)

4.3.2 Optimization of the ConA and Dextran Affinity System

Figure 4.2 illustrates the donor fluorescence intensity (diamonds) and acceptor fluorescence intensity (squares) for a solution of 3.75×10^{-2} μM dextran-donor and 4.95 μM acceptor-ConA concentrations as a function of added glucose in the solution. The results show that as the glucose competitively replaces the dextran from ConA binding, the transfer of energy from the donor decreases resulting in increased donor fluorescence. Unexpectedly, but similar to the results obtained by Meadows and Shultz (108), the acceptor emission increased, due perhaps to reduction of self-quenching. Upon comparing the intensity change of donor and acceptor emission with varying glucose concentration, it is seen that the measurement at the donor emission wavelength has greater sensitivity to glucose concentration than measurement of the acceptor emission. For this reason, the donor fluorescence was monitored in all subsequent measurements.

Figure 4.3 is a plot of the donor fluorescence at 602 nm as a function of the donor-dextran concentration in the absence of acceptor or glucose. As the concentration of donor-dextran increases beyond 0.09 μM, fluorescence decreases. We hypothesize that this effect is owing to the inner filter effects which distort the fluorescence spectra at higher concentrations. It is also noteworthy that a limitation in the concentration of donor-dextran is reached in this free, non-immobilized system by precipitation of the conjugate due to a strong multivalency interaction (122). Consequently, the donor-dextran concentration in this affinity system should be 0.09 μM or lower for optimal measurement sensitivity. All subsequent measurements were conducted at a donor-dextran concentration of 0.09 μM or lower.

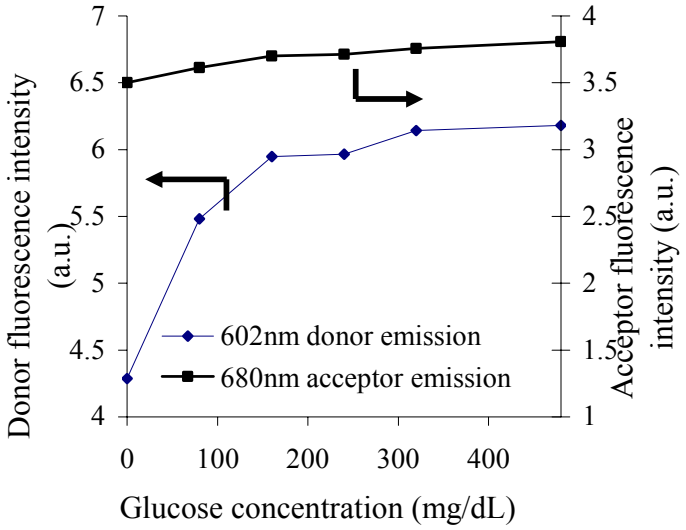

Figure 4.2. Donor (left) and acceptor (right) fluorescence intensity change (a.u.) at 602 and 680 nm resulting from excitation at 568 nm as a function of glucose concentration (mg/dL). The donor concentration was 0.0375 μM; and the acceptor concentration was 4.95 μM. Symbols denote measurements while the trend lines connect measurements.

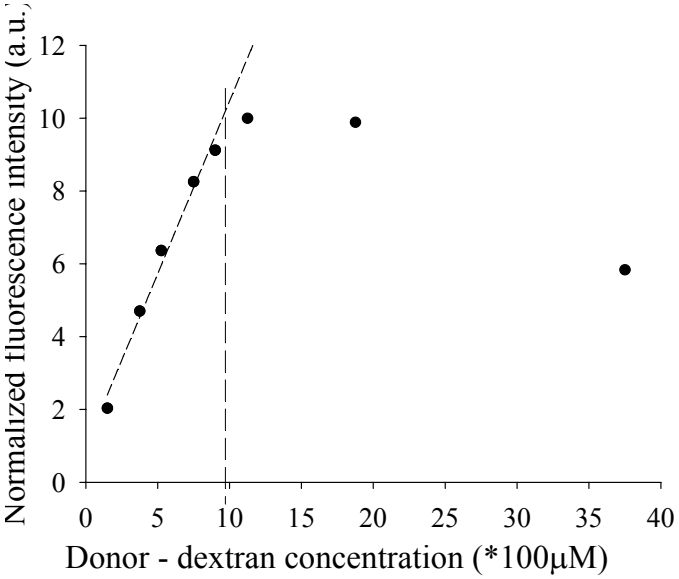

Figure 4.3. Normalized donor fluorescence intensity (a.u.) at 602 nm following excitation at 568 nm as a function of donor-dextran concentration (×100 μM). The symbols denote experimental measurements and the dotted line is the linear fit at low donor concentrations. At donor-dextran concentrations above 0.09 μM (denoted by dotted line), inner filter effects distort the fluorescence spectra.

Figure 4.4 illustrates an example of the phase-delay measured at 110 MHz of the donor fluorescence as a function of glucose concentration for two different acceptor-ConA concentrations of 4.95 and 8.25 μM at a constant donor-dextran concentration of 0.0375 μM. These results show that upon increasing the acceptor-ConA concentration from 4.95 (open circles) to 8.25 μM (closed circles), the glucose sensing range is expanded but with reduced sensitivity at the lower glucose concentration which might better detect the life-threatening hypoglycemia. Our findings differ from previous reports which show no change in sensitivity with increasing ConA concentration (48).

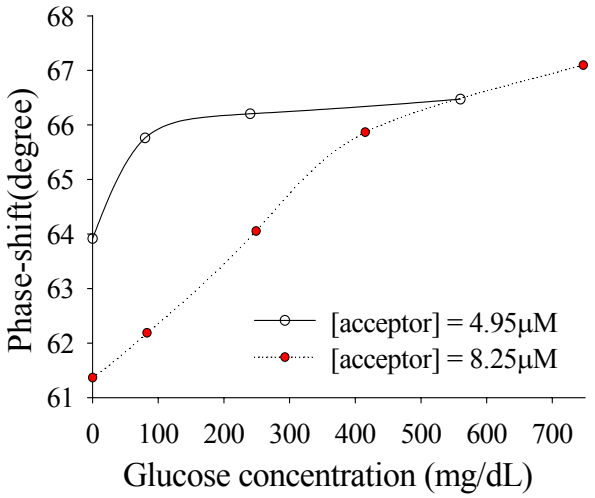

Figure 4.4. The phase-shift (degrees) at 110 MHz of donor emission at 600 nm in response to excitation at 568 nm as a function of glucose concentration (mg/dL). Symbols denote measurements for acceptor concentration of 4.95 μM (open circles) and 8.25 μM (filled circles) at a donor-dextran concentration of 0.0375 μM. The lines connecting the measurements indicate the trend lines.

4.3.3 FD Measurements of FRET Changes with Adding Acceptor-ConA and Glucose

Figure 4.5 and Figure 4.6 present the phase-shift and modulation-ratio of the donor emission as a function of modulation frequency for a solution with donor-dextran concentration of 0.09 μM with incremental concentrations of added acceptor-ConA. Error bars were calculated using the standard deviation of eight measurement results. Measurements were conducted with concentration ratios of acceptor-ConA to donor-dextran up to 118:1. As the concentration of acceptor-ConA increases, the binding of ConA to dextran (i) reduces the average distance between donor and acceptor molecules, (ii) increases energy transfer between the FRET pair, and (iii) reduces the lifetime of the

donor molecule. If one considers a mean lifetime change in which we used an average lifetime decay kinetics model ($\Delta\theta = \tan^{-1}(\omega\tau_0) - \tan^{-1}(\omega\tau_{avg})$ (26)), then a ~21% increase in donor lifetime (i.e. $(\tau_o - \tau_{avg})/\tau_o$) occurs when the acceptor-ConA concentration increases from 0 to 10.67 μM. Here we define τ_0 as the unquenched donor lifetime (3.6 ns) and $\bar{\tau}$ as the donor lifetime at certain acceptor-ConA concentration.

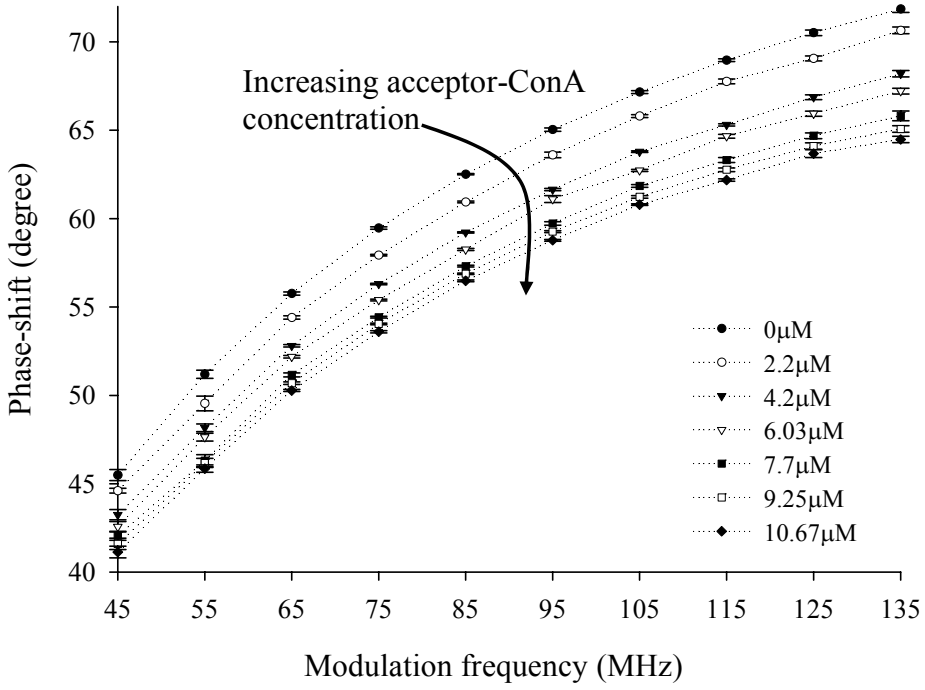

Figure 4.5. The phase-shift (degree) at 600 nm in response to excitation at 568 nm as a function of modulated frequency (MHz) with increasing acceptor-ConA concentrations as indicated in the legend. The symbols denote the average of n=8 measurements at various acceptor-ConA concentrations; the error bar denotes standard deviations; and the dotted line denotes a trend line. The donor-dextran concentration was 0.09 μM.

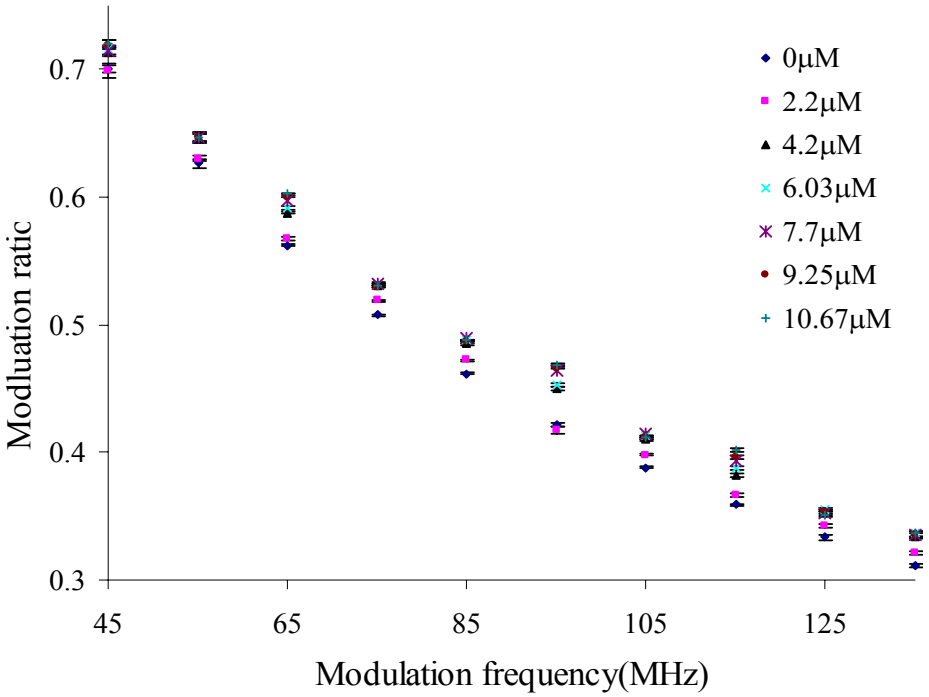

Figure 4.6. The modulation ratio at 600 nm in response to excitation at 568 nm as a function of modulated frequency (MHz) with increasing acceptor-ConA concentrations as indicated in the legend. The symbols denote the average of n=8 measurements at various acceptor-ConA concentrations; the error bar denotes standard deviations. The donor-dextran concentration was 0.09 μM.

In our second experimental step, glucose concentrations were increased to competitively replace the dextran binding to ConA and thus change the distance between the donor and acceptor in the system (50). Figure 4.7 and Figure 4.8 illustrate the phase-shift and modulation ratio of the donor emission as a function of modulation frequency at increasing glucose concentrations for a solution with donor-dextran concentration at 0.09 μM and the acceptor-ConA concentration at 10.67 μM. As the glucose concentration increases, dextran binding to ConA is displaced by glucose which (i) increases the average distance between donor and acceptor molecules, (ii) decreases

energy transfer between the FRET pair, and (iii) increases the lifetime of the donor molecule. If one considers a mean lifetime change, then a ~13% increase in donor lifetime occurs when the glucose concentration increases from 0 to 224 mg/dL. While the refractive index as well viscosity of highly concentrated ConA-dextran solution could impact decay kinetics (20,143,144), the influences of viscosity and refractive index change are negligible at the concentrations used herein. Based on the experimental results shown in Figure 4.7 and Figure 4.8, we extracted parameters α, β, and γ in the donor decay kinetics model using Equations 3.8 and 3.16.

4.3.4 FRET Decay Kinetics of Donor-dextran in Response to Increasing Acceptor-ConA and Glucose Concentrations

Figure 4.9 illustrates the parameter estimates of γ, β, and α as a function of acceptor-ConA concentration for the fluorescence lifetime phase-shift data presented in Figure 4.5 as well as the modulation ratio data presented in Figure 4.6. Figure 4.9(a) shows an increase in the parameter γ with increasing acceptor-ConA concentration consistent with enhanced FRET. Table 4.2 (a) lists the change of average donor lifetime, τ_{avg}, and parameter γ at increasing acceptor-ConA concentration. We find the percentage change of the mean lifetime ($\Delta\tau/\tau_0$~21%) is smaller than the percentage change of γ with increasing acceptor concentration (~70%, $\Delta\gamma/\gamma_{max}$, where γ_{max} is parameter value at 10.67 μM of acceptor-ConA concentration). Figure 4.9(b) demonstrates that parameter β does not appear to systematically vary with acceptor concentration, but differs from the values expected for freely diffusible donor and acceptor encountered in two and three dimensions (0.27 ± 0.18). Figure 4.9(c) also shows that the value of α does not vary

with acceptor concentration. The average value of α in Figure 4.9(c) is 3.76 ± 0.13 ns which is close to the unquenched lifetime of 3.6 ns. The small difference may be due to change of donor lifetime after conjugation with dextran.

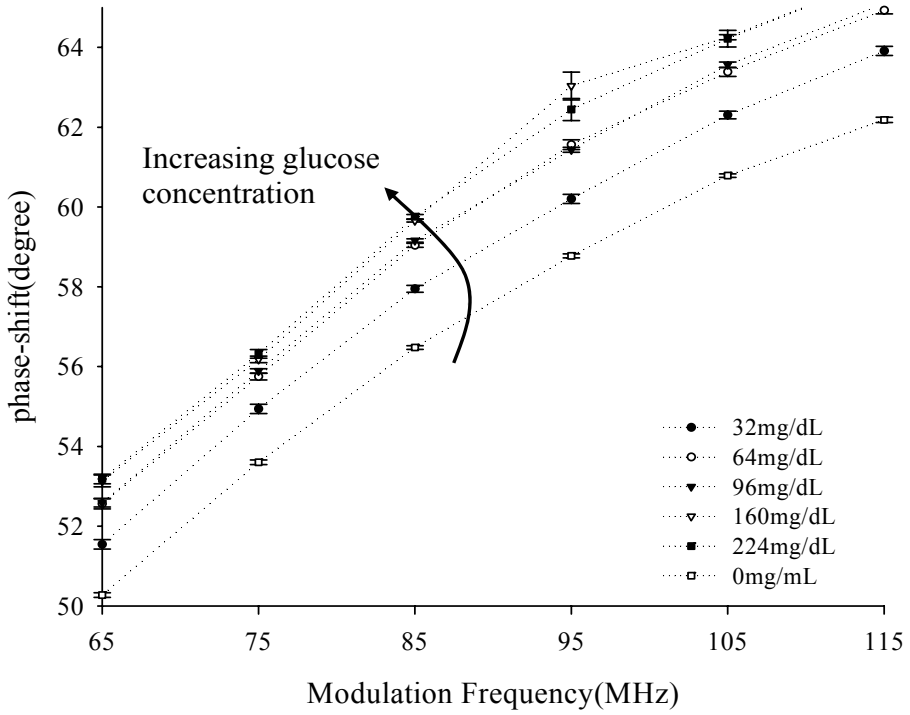

Figure 4.7. The phase-shift (degree) at 600 nm in response to excitation at 568 nm versus modulation frequency (MHz) as a function of increasing glucose concentration (mg/dL) as indicated in the legend. The symbols denote the average of n=8 measurements at various glucose concentrations; the error bar denotes standard deviations; and the short-dash line denotes a trend line. The donor-dextran concentration was 0.09 μM, and the acceptor-ConA concentration was 10.67 μM.

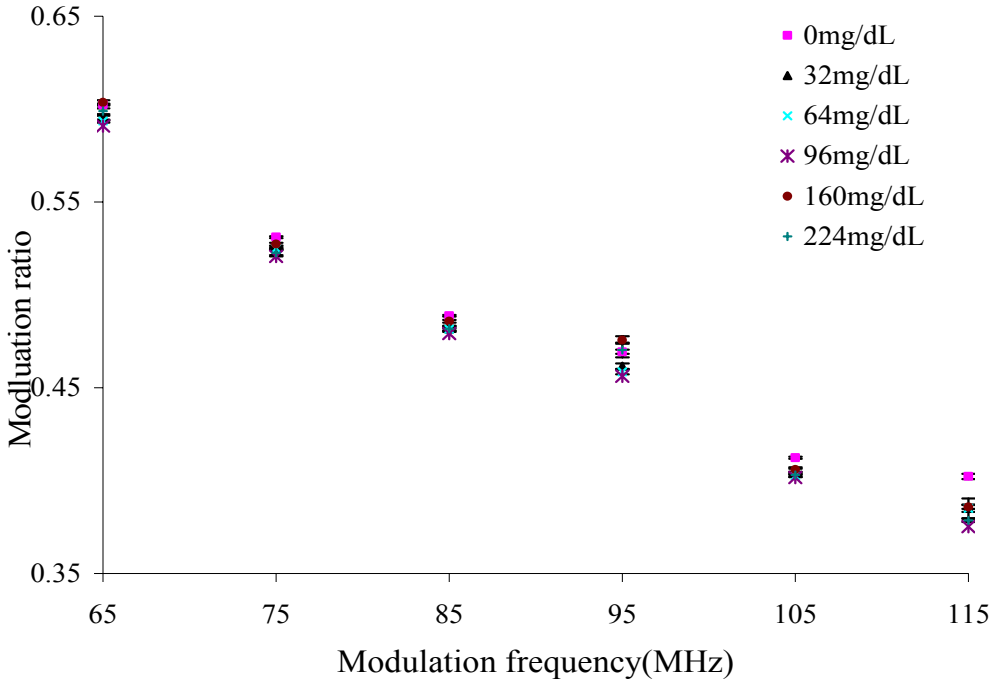

Figure 4.8. The modulation ratio at 600 nm in response to excitation at 568 nm versus modulation frequency (MHz) as a function of increasing glucose concentration (mg/dL) as indicated in the legend. The symbols denote the average of n=8 measurements at various glucose concentrations; the error bar denotes standard deviations. The donor-dextran concentration was 0.09 μM, and the acceptor-ConA concentration was 10.67 μM.

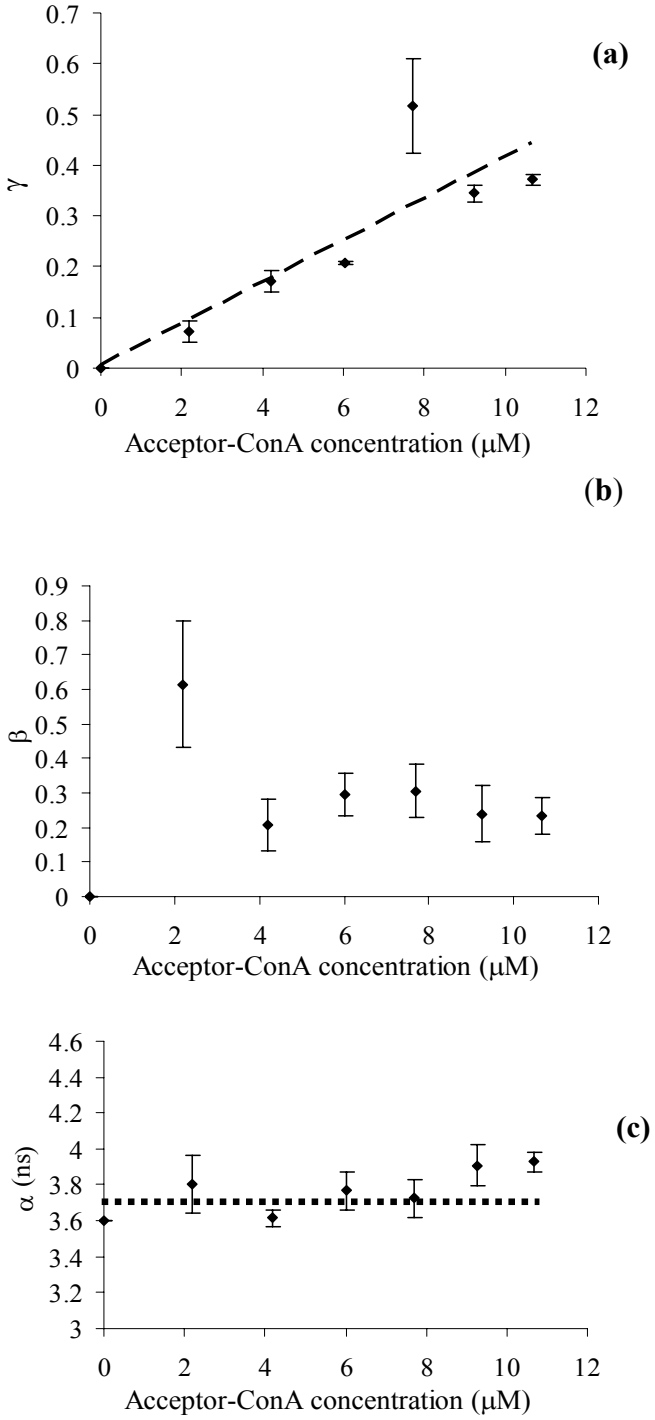

Figure 4.9. Parameter estimates of (a) γ (dimensionless), (b) β (dimensionless) and (c) α (ns) as a function of acceptor-ConA concentration, based on the concentration of dextran is equal to 0.09 μM. The symbols denote the average values calculated from calculated average phase-shifts and modulation-ratios. The error bars denote standard deviations determined from the standard deviations of phase-shifts and modulation-ratios. The dotted lines are the linear fits.

Table 4.2. Comparison of the change of donor average lifetime and the change of parameter γ with (a) increasing acceptor-ConA concentration; (b) increasing glucose concentration. Average lifetime values are calculated from phase-shift data, assuming single-exponential decay kinetics.

(a)

acceptor-ConA concentration (μM)	average lifetime (τ_{avg}, ns)	γ
0	3.60	0
2.20	3.39	0.07
4.20	3.12	0.17
6.03	3.02	0.21
7.70	2.89	0.52
9.25	2.84	0.35
10.67	2.79	0.37

(b)

glucose concentration (mg/dL)	average lifetime (τ_{avg}, ns)	γ
0	2.79	0.37
32	2.87	0.28
64	3.03	0.05
96	3.05	0.19
160	3.15	0.13
224	3.16	0.12

Figure 4.10 illustrates the parameter estimates of γ, β, and α as a function of glucose concentration for the fluorescence lifetime phase-shift data presented in Figure

4.7 as well as the modulation ratio data presented in Figure 4.8. Figure 4.10(a) shows that γ decreases with increasing glucose concentration, consistent with decreased FRET associated with competitive displacement of dextran from ConA. Table 4.2 (b) lists the average donor lifetime, τ_{avg}, and parameter γ at increasing glucose concentration. Upon comparing with the percentage change in mean lifetime ($\Delta\tau/\tau_0$~13%), one finds that the percentage change of γ with increasing glucose concentration from 0 to 224 mg/dL is approximately 67% ($\Delta\gamma/\gamma_{max}$). Figure 4.10(b) demonstrates that parameter β does not systematically vary with glucose concentration, but expectedly differs from the values expected for freely diffusible donor and acceptor encountered in two and three dimensions (0.30 ± 0.11). Apparently the dimensionality of the affinity system has been changed. However more experiments data are required to explain the change in β. The average value of the term α in Figure 4.10(c) is also 3.76 ± 0.18 ns, again consistent with the unquenched lifetime of the donor.

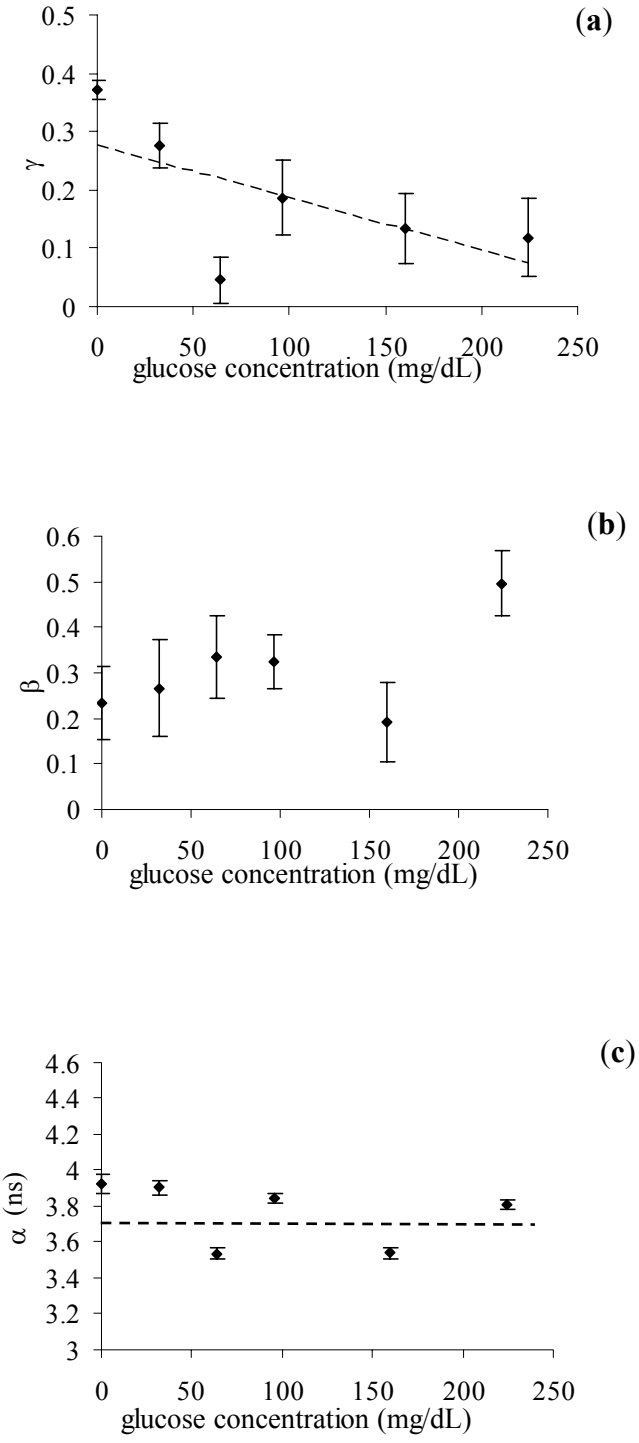

Figure 4.10. Parameter estimates of (a) γ (dimensionless), (b) β (dimensionless), and (c) α (ns) as a function of glucose concentration, based on the concentration of dextran is equal to 0.09 μM and the concentration of ConA is equal to 10.67 μM respectively. The symbols denote the average values calculated from calculated average phase-shifts and modulation-ratios. The error bars denote standard deviations determined from the standard deviations of phase-shifts and modulation-ratios. The dotted lines are the linear fits.

Both Figure 4.9 and Figure 4.10 show that parameter γ may be used to quantitatively measure the FRET effects. While phase-shift could be used to directly determine changes of glucose concentration as shown by others, we find that γ as opposed to phase-shift change at a single modulation-frequency (i.e. Figure 4.6) may increase the sensitivity of measurements of glucose concentration. Our observation is in agreement with Rolinski and coworkers (50). More results are needed to understand the changes in β, as the dimensionality of the pair distribution function of the conjugated acceptor and donor cannot be assumed to be a random in three-dimensions (50).

In contrast to previous reports by Rolinski *et al.* (50) in which they found binding equilibrium at long times after addition of MG-dextran to APC-ConA, we did not find a change of FRET decay kinetics with time using frequency-domain measurements 30 seconds after adding AF647-ConA to AF568-dextran. This observation indicates that the ConA-dextran complex forms immediately after addition as described by Tolosa, *et al.* (51). In another system employing Rhodamine 6G and MG as a FRET pair, Porter, *et al*. (145) also found rapid equilibrium of binding as indicated by FRET decay parameters. Thus, dynamic change of FRET in the APC-MG system seen by Rolinski, *et al*. (50), could indicate that the FRET between APC and MG is due not only to the binding of ConA to dextran, but perhaps due to interactions between APC and MG.

We also evaluated the existence of FRET effects between free AF568 and AF647 in solution and found none, again an inconsistent result compared to that reported by Rolinski *et al*. (138). Considering the smaller size and lower concentration of our donor/acceptor pair in comparison to the APC/MG FRET pair, this result is not

surprising. However our findings confirm the lack of molecular interaction between AF568 and AF647 that may have existed between free APC and MG (110).

4.4 Summary

We have shown that frequency-domain measurements can be used to extract FRET decay kinetic parameters to quantify glucose concentration using the ConA-dextran affinity system in a non-scattering solution over the range of 0 – 224 mg/dL. While using parameter γ could possibly provide better sensitivity for evaluating glucose concentration than the raw measurement of phase-shift, it is the simplicity of frequency-domain measurements which promises a potential, low-cost sensing instrument using long-lived fluorophores as proposed by others (146,147) as well as short-lived fluorophores whose lifetimes are on the same order of magnitude as the photon "time-of-flight" in tissues. In order to deploy frequency-domain techniques with an implantable ConA-dextran sensing device, the time delays attributable to the decay kinetics of the ConA-dextran fluorescence affinity system will need to be distinguished from photon "time-of-flights" that arise from the optical properties of tissue. Our work continues to accurately extract the kinetic decay parameters γ from multiply scattered donor fluorescence emanating from an implanted sensor in order to quantify glucose concentrations *in vivo*.

5. MICROSPHERE-BASED IMPLANTABLE OPTICAL SENSORS FOR PH*

5.1 Introduction

Optical methods offer unique opportunities for *in situ*, biomedical sensing of tissue analytes and metabolites owing to economics, avoidance of sample contamination, and in the case of fluorescence, exquisite sensitivity. Fluorescence lifetime spectroscopy techniques furthermore possess advantageous insensitivity to sensing fluorophore concentration, photobleaching, and instrument artifacts (142), yet have not been widely deployed as a means for ultrasensitive detection of analytes and toxins.

Fluorescence lifetime spectroscopy consists of exciting a fluorophore, whose lifetime is sensitive to an analyte (e.g. pH, Ca^{2+}, O_2, glucose, etc.) of interest, with intensity-modulated excitation light. Upon activation, the fluorophore remains in an excited state for a mean period of time known as its 'fluorescent lifetime' (τ) before relaxation to the ground state either non-radiatively, or radiatively through the release of a fluorescent photon. Owing to the picosecond/nanosecond lifetime of most fluorophores, the fluorescence signal generated in response to the intensity modulated excitation light is modulated at the same frequency as the excitation light, (i.e., in the order of 100 MHz), but is phase-shifted (θ) by as much as ninety degrees and amplitude-attenuated (M).

---

* Part of this section is reproduced in part with permission form "Fluorescence lifetime spectroscopy of a pH-sensitive dye encapsulated in hydrogel beads," by Eddy Kuwana, Feng Liang, and Eva Sevick-Muraca, *Biotechnology Progress*, 2004, 20, 1561-1566. Copyright 2004 American Chemical Society.

Typically, these frequency-domain or 'phase-modulation' measurements are conducted on diluted, non-scattering samples (54,125) and require a 'reference' measurement in order to account for temporal instrument artifacts (142). Fluorescence intensity and lifetime-based measurements are the basis of chemical sensor or 'minimally invasive' biosensor design employing exogenous fluorophores. These designs generally consist of fluorescent dye embedded within a polymer matrix or semi permeable membrane placed at the tip of an optical fiber (148-150). Immobilization of sensing fluorophores for *in vivo* diagnostics is necessary owing to their potential toxicity as well as the need to make repeated analyte/metabolite measurements. PEG-based polymers, which are potential candidates for immobilizing sensing fluorophores, have previously been investigated as *in vivo* protein drug delivery devices, preventive agents for post surgical adhesion formation, and biocompatible membranes over electrochemical sensors (151).

Russell *et al.* successfully synthesized optically transparent PEG hydrogel spheres in order to encapsulate a glucose sensitive FRET fluorophore system (40). They studied the FRET fluorescence intensity response from this immobilized system at various glucose concentrations in buffered solutions. However, intensity-based fluorescence measurements are susceptible to variations in fluorophore loading and when implanted *in situ* within tissues, they are sensitive to variations in tissue optical properties. Since fluorescence lifetime is an intrinsic property of the fluorophore molecule, it is insensitive to the fluorophore concentration and excitation source intensity. Nevertheless, determination of fluorescence lifetime in scattering media (such

as tissues) is distorted due to the "time-of-flight" associated with the migration of light. Hence, fluorescence lifetime spectroscopy of implantable sensors requires a model which accounts not only for fluorescence decay kinetics, but also photon propagation due to the tissue scattering.

In previous work, we have demonstrated the enhanced sensitivity of fluorescence lifetime spectroscopy in the presence of multiple scattering that occurs in the NIR regime by means of the FDPM technique (123). Specifically upon using a mixture of long lifetime DTTCI (1.33 ns) and shorter lived ICG (0.5 ns) dyes, we demonstrated that the small differences in frequency-domain or phase-modulation measurements of phase-shift and amplitude-attenuation of generated fluorescence light can be amplified by the presence of multiple scattering caused by tissue mimicking scattering. Furthermore, upon adapting a coupled photon diffusion equation to describe (i) the stochastic excitation and emission light propagation and (ii) the kinetics of fluorescence generation, we have demonstrated the ability to measure fluorescence lifetime from phase-shift measurements in multiply scattering solution. In another study, we have demonstrated the proof of principle by successfully obtaining average lifetime in tissue-like scattering solutions of a pH sensing fluorophore, carboxy seminaphthofluorescein-1 (C-SNAFL-1) (136). In this present study, we seek to develop implantable biosensor consisting of C-SNAFL-1 immobilized in PEG hydrogel and perform fluorescence lifetime measurement within multiply scattering solutions.

5.2 Materials and Methods

5.2.1 Dyes and Solutions

The pH sensitive fluorescence dye, C-SNAFL-1 ester was obtained form Molecular Probes (Eugene, OR) and used as received. C-SNAFL-1 has been shown to exhibit single-exponential and two-exponential decay kinetics at solution pH of 4.9 and 9.3, respectively (125). MOPS (3-(N-morpholino) propanesulfonic, Sigma-Aldrich, Milwaukee, WI) buffer solution was used to condition the sample pH, and in the case of measurements within a scattering medium, polystyrene (dialyzed Dow 788, particle size 143 ± 22 nm, Dow Chemical Co., Midland, MI) was added. By employing different MOPS salt concentrations, we varied the pH between 7 and 9 in both dilute MOPS (non-scattering) and MOPS/polystyrene (scattering) solutions, while 5 mM buffer strength was maintained. Carboxy seminaphthofluorescein-2 (C-SNAFL-2) (Molecular Probes, Eugene, OR) dissolved in PBS buffer at pH 4.9 (± 0.1) was employed as a reference dye for phase-modulation measurements in the non-scattering solutions.

We conjugated SNAFL to a sugar binding protein, ConA, which was covalently bond to PEG prior to photopolymerization to form hydrogel beads containing the immobilized pH sensing fluorophore.

Poly(ethylene glycol) diacrylate (PEG-DA) with a molecular weight of 575; 2-hydroxy-2-methylpropiophenone (HMP, photoinitiator); Trimethylolpropane triacrylate (TPT, crosslinker); ConA (Type V); and DMSO were obtained from Sigma-Aldrich (Milwaukee, WI). Acryl-PEG-NHS (α-acryloyl ω-N-hydroxysuccinimidyl ester of PEG-propionic acid) with a molecular weight of 3400 was obtained from Nektar

Therapeutics (Birmingham, AL). Light and heavy paraffin oil and n-heptane were purchased from Fisher Scientific Inc. (Pittsburgh, PA). All the reagents were used as received. Phosphate-buffered saline (PBS, 1L, pH=7.2) consisted of 8 g NaCl, 0.2 g KCl, 1.44 g Na_2HPO_4 and 0.24 g KH_2PO_4. Sodium bicarbonate buffer (NaB, 1L, titrated with HCl until pH=8.3) consisted of 8.4 g $NaHCO_3$ and 29.2 g of NaCl.

5.2.2 Synthesis of SNAFL-ConA

The primary reagents for SNAFL-ConA conjugate consist of C-SNAFL-1 ester and ConA. Prior to incubation, 10 mg of ConA was dissolved in 1 mL NaB (continuous shaking for 20 mins) and 1mg of C-SNAFL-1 ester was dissolved in 0.1mL DMSO. The conjugation performed was similar to Haugland by mixing the dissolved ConA and C-SNAFL-1 ester and incubating the mixture at room temperature for 4 hrs (141). SNAFL-ConA (labeling ratio was approximately 5) was produced due to the ester-amine reaction between ester of C-SNAFL-1 with the lysine present in ConA (141).

5.2.3 Immobilization of SNAFL-ConA into Clear PEG Hydrogel

The synthesis protocol for SNAFL immobilized in PEG was similar to that used by Russell *et al*. (40). The primary reagents for immobilization of SNAFL-ConA in optically transparent PEG hydrogel (SNAFL-ConA-PEG) consisted of SNAFL-ConA, acryl-PEG-NHS, PEG-DA, TPT, and HMP. The procedure to prepare the precursor solution was as follows: (i) SNAFL-ConA solution and 24 mg of Acryl-PEG-NHS were added to 8mL PEG-DA and the resultant mixtures were dissolved for 2 hrs while shaking (Daigger shaker, model 22406A, Vernon Hills, IL). The ester of acryl-PEG-

NHS reacted with the lysine present in SNAFL-ConA; (ii) 160 μL HMP and 960 μL TPT were added and the solution was mixed and shaken for another 30 mins; and (iii) the resulting precursor solution was then extruded through a 26G syringe needle (10 mL, Becton Dickinson, Franklin Lakes, NJ) using a syringe pump (model 100, KDScientific, New Hope, PA). Compressed air was sprayed upon the solution droplets and to break the droplets apart into finer droplets. The fine droplets fell into a bath of 1L mineral oil mixture (volumetric ratio of light oil to heavy oil was 1 to 3). The light and heavy oil mixtures were used to prevent agglomeration at the bottom section of the bath and to avoid long exposure to UV light (EFOS Ultacure 100SS Plus, output of 20 W/cm^2) at the top section. The photo-initiator photo-fragmented upon exposure to the UV light resulting in the production of highly reactive radicals. These radicals induced gelation of the PEG chains into a hydrogel network by activating the acrylate groups. Exposure to UV light was limited to seconds to minimize exposure and to complete polymerization as the precursor droplets descended down the mineral oil. The resulting PEG spheres (SNAFL-PEG) were then rinsed with heptane and PBS. The size of the particle can be controlled by proper adjustments of syringe pump volumetric rate and compressed air spray pressure. The set-up for the polymerization process is shown in Figure 5.1.

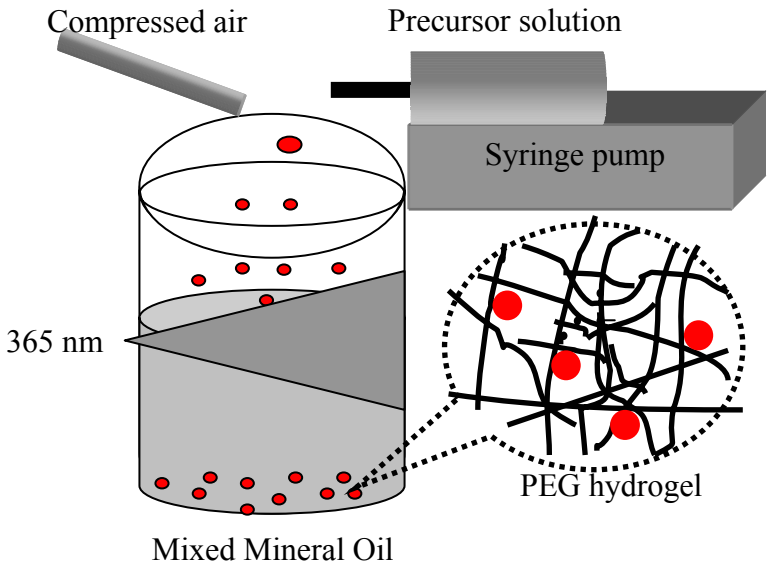

Figure 5.1. Hydrogel preparation set-up where droplets of precursor solution were extruded through a syringe pump, sprayed with compressed air resulting into fine droplets that fell into mineral oil bath, and photopolymerized upon exposure to UV light at 365nm.

Approximately 200 mL of SNAFL-PEG beads (35% void fraction) were produced. The average diameter of the hydrogel particles was found to be 160 μm (Figure 5.2), as measured by a random sampling of 300 microsphere beads using Nikon microscope (Optiphot2-UD, Nikon, Melville, NY) equipped with stage micrometer. The hydrogel product was then repetitively washed and dialyzed (in PBS) every 12 hours for a period of 3 days to remove the un-reacted SNAFL dye present in the hydrogel. After a period of 10 days submersion in PBS, less than 1% of leakage in the SNAFL-PEG was found based on spectra intensity comparison between the hydrogel and the supernatant. The degree of penetrant diffusivities into cross-linked PEG hydrogel networks depends

upon the cross-linker concentration, size of PEG microspheres, and size of the penetrant molecules (42,152).

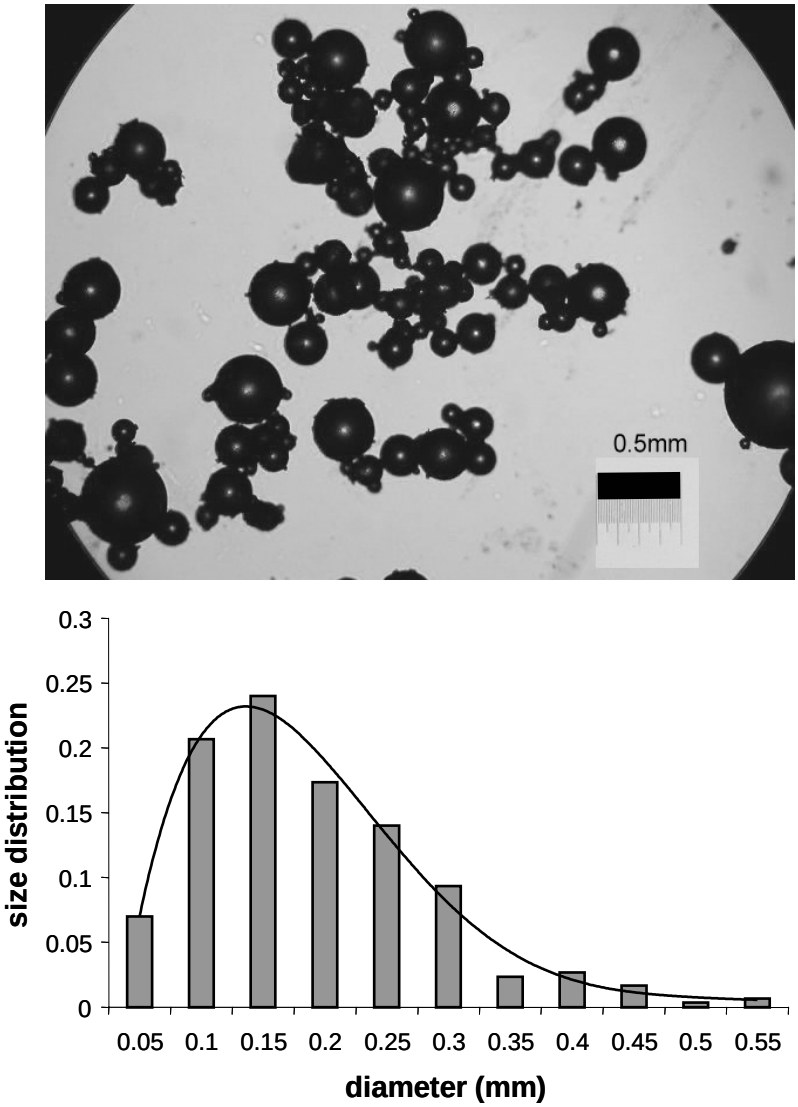

Figure 5.2. (Top figure) PEG microspheres under Nikon microscope and (Bottom figure) size distribution of the PEG microspheres. The bars in the size distribution plot indicate the fraction of the 300 randomly sampled beads with the corresponding diameter size. The line plot suggests that a normal size distribution with positive skew was attained.

In addition to SNAFL-PEG, we also prepared additional PEG hydrogels without SNAFL. The gel samples for measurements in polystyrene scattering solutions consisted of 115 mL of SNAFL-PEG beads mixed with 85 mL PEG beads. Measurements in scattering polystyrene solutions were conducted within 200 mL sample containing 0.5% (by volume) polystyrene and MOPS buffers at various, measured pH values (7.7, 8.2, and 8.8). Prior to performing measurements at a particular pH value, the hydrogels were washed with DI water and rinsed with the corresponding pH buffer. Excess of liquid was removed by vacuum filtration flask setup before addition of polystyrene and MOPS buffer having the desired pH value.

5.2.4 Phase Shift and Modulation Measurements

Measurements were performed using the FDPM method, as described elsewhere. (30,123) Briefly, a continuous wave (CW) light from a wavelength tunable Ar-Kr mixed gas laser (Model 643; Melles Griot, Boulder, Colorado) at 514 or 647 nm wavelengths was modulated by an external electro-optic modulator (EOM) (Model 350-160, Conoptics, Danbury, CT) at modulation frequencies between 10 and 130 MHz. The detectors consisted of two photomultiplier-tubes (PMT, Model H6573, Hamamatsu, Tokyo Japan) which were gain-modulated by a second oscillator for heterodyne operation.

The PMT's were outfitted with focusing lens assemblies as well as neutral-density (CVI Laser, Albuquerque, NM) and narrow-bandpass interference filters (10 nm FWHM, CVI Laser) in order to optimize the amount of light detected at the incident wavelengths for excitation and emission measurements. In addition, a long pass filter

(LPF 550, CVI Laser) was used to collect fluorescence in response to illumination at 514 nm for measurement of fluorescence phase and modulation ratio (θ_M and M_M) in scattering and non-scattering solutions.

5.2.5 Measurements in Non-scattering Solutions

For measurements in non-scattering solutions, light at 514 nm was used and fluorescence light was detected at right angles to the sample at 650 nm. The fluorescent phase-shift and modulation-ratio (θ_f and M_f) of SNAFL-PEG submerged in MOPS buffer at differing pH, were measured as a function of modulation frequency (10 to 130 MHz). To correct for the instrument response, lifetime determination from phase-shift and modulation-ratio measurements in non-scattering solutions required 0.5 μM of carboxy seminaphthofluorescein-2 (C-SNAFL-2) in PBS buffer at pH 4.9 (±. 0.1) as a reference. The lifetime of C-SNAFL-2 at pH 4.9 is known to be 4.59 ns (125).

The phase-shift and modulation-ratio (θ_M and M_M) of a dye that exhibits multi-exponential decay kinetics in non-scattering media are functions of multi-exponential decay parameters as follows:

$$\theta(\omega) = \tan^{-1}\left(\frac{\sum_j^n \frac{a_j \omega \tau_j^{\,2}}{\left(1+\omega^2 \tau_j^{\,2}\right)}}{\sum_j^n \frac{a_j \tau_j}{\left(1+\omega^2 \tau_j^{\,2}\right)}}\right) \tag{5.1}$$

$$M(\omega) = \left[\left(\frac{\sum_j^n \frac{a_j \omega \tau_j^{\,2}}{\left(1+\omega^2 \tau_j^{\,2}\right)}}{\sum_j^n a_j \tau_j}\right)^2 + \left(\frac{\sum_j^n \frac{a_j \tau_j}{\left(1+\omega^2 \tau_j^{\,2}\right)}}{\sum_j^n a_j \tau_j}\right)^2\right]^{\frac{1}{2}} \tag{5.2}$$

where a_j is a pre-exponential factor representing the fractional contribution to the time-resolved decay of the component with a lifetime τ_j. For the case of two-exponential, n is equal to 2. The values of a_j and τ_j for a given sample can be estimated from measurements of phase-shift $\theta(\omega)$ and modulation-ratio $M(\omega)$ by minimizing χ^2, which is the error-weighted sum of the squared deviations between the measured and predicted values (142). The Nelder-Mead method (153) can be used in order to minimize χ^2 with respect to the parameters a_j and τ_j.

5.2.6 Measurements in Scattering Solutions

For fluorescence measurements in scattering polystyrene solutions, fluorescence light at 650 nm was collected from a submerged fiber optic (1000 μm diameter, Thorlabs, Newton, NJ) located 1 cm and 1.6 cm away from a submerged fiber optic delivery of

modulated excitation light at 514 nm (123). The multiplexing method described by Mayer *et al.* (30) was performed to eliminate instrument response functions for fluorescence measurements in the polystyrene scattering solutions. Unlike non-scattering measurements of lifetime, no reference dye was required. In our study, the response time of SNAFL-PEG for changes of pH from 7.6 to 8.6 was found to be approximately 5 mins.

In addition, using the same submerged collection and delivery fiber optics, measurements of phase-delay and amplitude-attenuation were made following illumination at both the excitation wavelength at 514 nm (θ_x and M_x) and emission wavelength (θ_m and M_m) at 650 nm. Measurements were conducted as a function of modulation frequency as the distance between the illuminating and collecting fiber optics, (Δr), varied between 1.2 cm to 1.6 cm. From these measurements, the optical properties of the scattering samples at the excitation (μ_{ax} and μ'_{sx}) and emission wavelength (μ_{am} and μ'_{sm}) were determined for each scattering solution (123).

The relationship between phase-shift θ_M detected at position r relative to the incident point of excitation light and average lifetime τ_{avg}^{scat} of the sensing fluorophore has been derived from the optical diffusion equation in an infinite medium, and is shown as Equation 5.3:

$$tan\theta_f(r,\omega) = \frac{B + A\omega\tau_{avg}^{scat}}{A - B\omega\tau_{avg}^{scat}} \tag{5.3}$$

where the terms A and B are defined as Equations 3.30-3.35.

5.3 Results and Discussions

Figure 5.3 shows the spectra of C-SNAFL-1 ester, SNAFL-ConA, and SNAFL-PEG in PBS (pH 7.2) were obtained by SPEX FLUOROLOG II (HORIBA Jobin Yvon Inc., Edison, NJ). The excitation spectrum was obtained with emission monochromator set at 650 nm; while in the case of emission spectra, the excitation monochromator was stationed at 514 nm. While C-SNAFL-1 ester and SNAFL-ConA spectra are similar, SNAFL-PEG spectra are shifted to longer wavelengths.

5.3.1 Fluorescence Multi-exponential Decay in Non-scattering Solutions

The θ_M and M_M values of SNAFL-PEG in non-scattering solutions are plotted in Figure 5.4 and 5.5 on pages 104 and 105 as a function of solution pH. Similar to the free SNAFL, the decrease in phase and increase in modulation with increasing pH values is due to the increased relative contribution of the short-lived or de-protonated dye species at longer wavelengths (136). It was found that the two-exponential decay kinetic model adequately fit the data. The average lifetime for two-exponential fits, τ_{avg}, was calculated from the regressed parameters a_j and τ_j from the following relationship:

$$\tau_{avg} = \frac{a_1 \tau_1^{\,2}}{a_1 \tau_1 + a_2 \tau_2} + \frac{a_2 \tau_2^{\,2}}{a_1 \tau_1 + a_2 \tau_2} \tag{5.4}$$

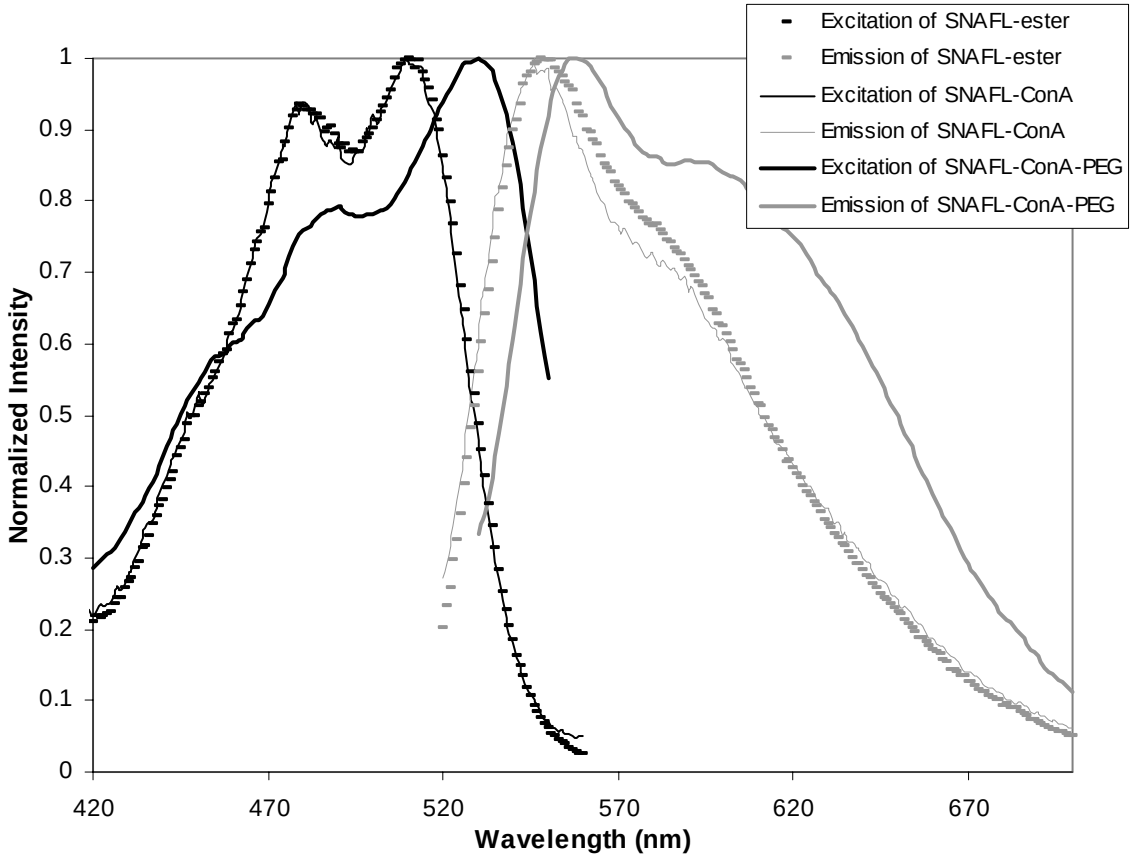

Figure 5.3. Excitation (emission at 570 nm) and emission (excitation at 514 nm) spectra of C-SNAFL-1 ester, SNAFL-ConA, and SNAFL-PEG in PBS (pH 7.2).

5.3.2 Model Predictions of Multi-exponential Lifetime Decay in Scattering Polystyrene Solutions

The θ_M and M_M values of immobilized SNAFL-PEG in buffer/polystyrene solutions are plotted in Figure 5.4 and Figure 5.5. The plots show a similar trend with pH as those observed in absence of scattering. However, comparison of scattering and non-scattering plots shows that scattering contributes significantly to the phase-shift and modulation-ratio values. The change in phase-shift and amplitude-attenuation with pH

was found in presence of scattering to be between 2 and 2.5 times larger than those changes in absence of scattering. This result is consistent with our previous study using free SNAFL-1 (136) in scattering and non-scattering solutions.

Comparison of non-scattering and scattering data also shows that scattering contributes significantly to the phase-shift values. The solid lines in Figure 5.4 and Figure 5.5 denote the predictions using the two-exponential decay model incorporating the time delay of τ_{avg} and the regressed optical properties from excitation and emission measurements. The plots show that the predicted values of θ_M and M_M exhibit the same trend as that shown by the experimental data.

Since the fluorescence data measured in the presence of scattering are in good agreement with the average lifetime model, fluorescence lifetime sensing of dyes exhibiting multiple decays may be performed by obtaining the average lifetime. For the experimental scattering systems studied herein, the average lifetime of fluorescent dyes in scattering solutions can be most accurately predicted when the modulation frequency is in the order of 100 MHz. It should be noted that consistent results were obtained (also shown in Table 5.1 as τ_{avg}^{scat} (repeat)) when the experiment was repeated using the same hydrogels after one month storage at 5^{o}C, confirming the reversibility and stability of immobilized C-SNAFL-1 dye in PEG hydrogels. Approximately within two months of storage, less fluorescence signal could be detected and lifetime measurements were no longer repeatable.

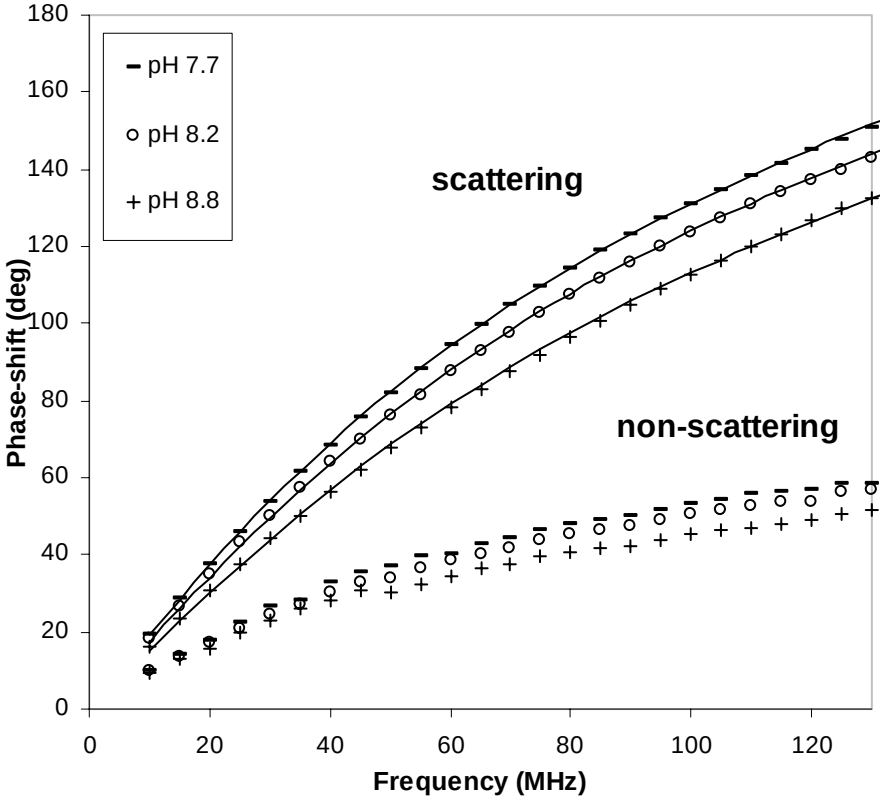

Figure 5.4. The values of fluorescence phase-shift, as a function of modulation frequency for SNAFL-PEG, where the plots in each figure consist of corrected experimental measurements (dotted lines) in non-scattering (bottom) and scattering solution (top) at various pH, and those predicted by the propagation model incorporating average lifetime (solid lines). Samples were excited at 514 nm and the emission was observed at 650 nm.

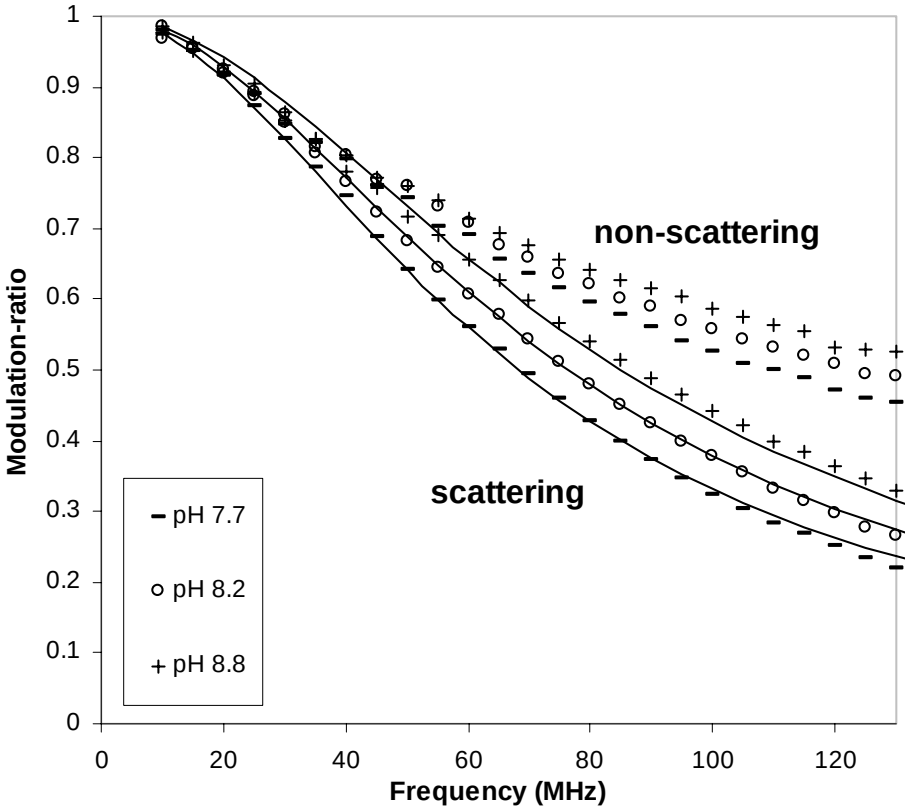

Figure 5.5. The values of modulation-ratio, as a function of modulation frequency for SNAFL-PEG, where the plots in each figure consist of corrected experimental measurements (dotted lines) in non-scattering (bottom) and scattering solution (top) at various pH, and those predicted by the propagation model incorporating average lifetime (solid lines). Samples were excited at 514 nm and the emission was observed at 650 nm.

It should be noted that in the absence of scattering, sub-nanosecond lifetime detection is difficult at these low modulation frequencies (10-130 MHz). The presence of scattering however, magnifies the measured phase-shift value, and hence increases the sensitivity of lifetime sensing at low modulation frequencies, given that the optical

properties of the medium can be accurately predicted. Figure 5.6 depicts the fluorescence phase-shift values at different pH for both non-scattering and scattering measurement at 100 MHz. The figure confirms that measurements in presence of scattering were not only magnified, but resulted in better resolution compared to those in absence of scattering. Table 5.1 shows average lifetime values τ_{avg}^{scat} that were recovered from phase-shift data acquired in presence of scattering, at 100 MHz using Equation 5.3. The values are in agreement with the values of τ_{avg} obtained from phase-shift measurements of C-SNAFL-1 in MOPS (non-scattering).

Table 5.1. Average lifetime values calculated from phase-shift data (τ_{avg}^{scat}) and from the repeated experimental data (τ_{avg}^{scat} (repeat)) in presence of scattering, assuming two-exponential decay kinetics, at a fixed frequency of 100 MHz, in comparison with the values obtained in dilute non-scattering solutions (τ_{avg}).

pH	τ_{avg} ± 0.05 (ns)	τ_{avg}^{scat} ± 0.05 (ns)	τ_{avg}^{scat} ± 0.05 (ns) (repeat)
7.7	2.89	2.86	2.91
8.2	2.73	2.69	2.69
8.8	2.50	2.47	2.49

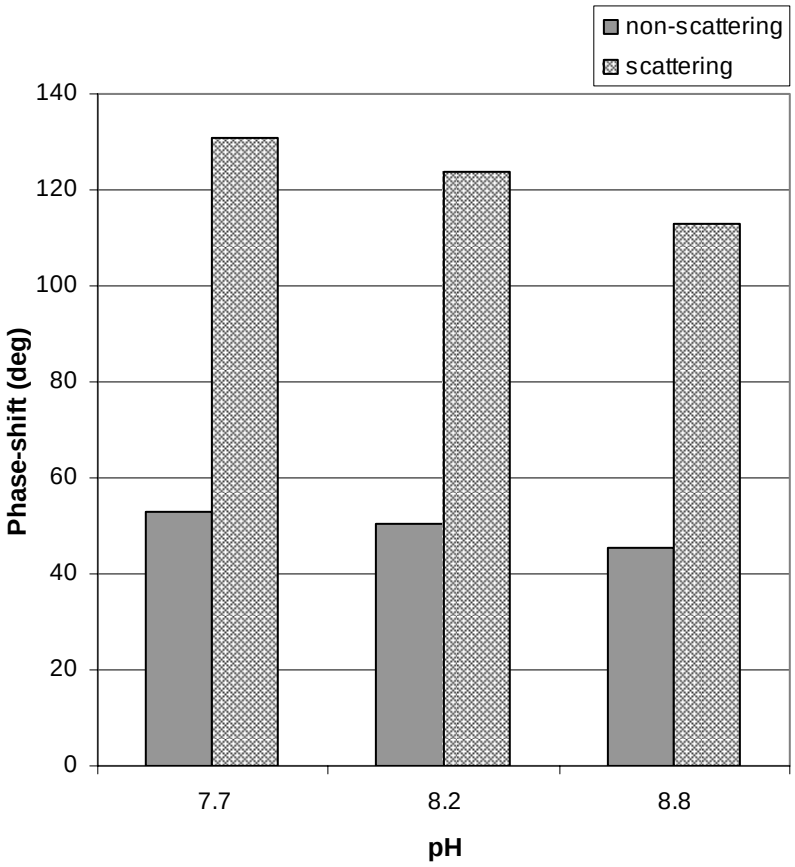

Figure 5.6. Average standard deviation of phase-shift data in non-scattering and scattering, calculated over a range of modulation frequencies from 30 to 130 MHz in 5 MHz increments with 3 measurements replicates experiment, at each pH value.

5.4 Summary

We have demonstrated, for the first time, the applicability of FDPM for fluorescence lifetime spectroscopy of immobilized fluorophore in multiply scattering solutions. The propagation of excitation and fluorescence light of a pH sensing dye, C-SNAFL-1, immobilized within a PEG hydrogel, in scattering polystyrene solution could be well predicted from the average lifetime. As a result, the measurement approach for conducting NIR fluorescence lifetime spectroscopy of immobilized dyes by means of light propagation model for is greatly simplified. In addition, owing to the stability of the immobilized fluorescence sensor as well as the reliability of fluorescence lifetime measurement, the method presented in this study may provide a new approach for analyte or toxin screening.

6. MONTE CARLO MODELING OF FLUORESCENCE PHOTON MIGRATION IN MICROSPHERE-BASED IMPLANTABLE SENSORS

6.1 Introduction

Many efforts to develop noninvasive glucose sensors have focused upon microsphere-based implantable fluorescent optical sensors. In this schema, (i) a glucose competitive binding ConA-dextran affinity system, or(ii) glucose oxidase and an oxygen-sensitive fluorophore are either chemically immobilized into the microsphere network or attached on the microsphere surface and then confined inside a sealed dialysis membrane (38,42,44). The microspheres protect the fluorophore from interaction with other possible interfering substances from blood plasma or interstitial fluids. They also increase the stability of affinity or glucose oxidase system and reduce potential toxicity by compartmentalizing the toxic dyes. The microspheres applied in previous studies were PEG hydrogel (40), alginate-poly-L-lysine (119), Sephadex (43), Sepharose (44), polystyrene (46), and polyelectrolyte-coated alginate microparticles (55,115).

Table 6.1 provides a cumulative summary of microsphere-based fluorescent optical sensors for glucose measurements. All these studies used intensity-based fluorescence measurements. However, other studies and our previous studies showed that lifetime measurements can provide an alternative measurement that might be advantageous over intensity measurements in several ways (30). The lifetime-measurements are not influenced by several confounding factors, such as: (i) variation of

immobilized fluorophore concentrations; (ii) fluorophore photobleaching; and (iii) instrumentation response function. In our study, fluorescence lifetime measurements are carried out by using FDPM techniques (154). Briefly, an intensity sinusoidally modulated laser light source is launched onto the surface of tissue or tissue-mimicking phantoms through an optical fiber. Then the light is scattered and absorbed due to the absorption and scattering of the media. The generated fluorescence light is again scattered and absorbed. Finally the detected fluorescence signal through a detecting optical fiber is phase-delayed and amplitude attenuated relative to the incident excitation light. The phase-shift and amplitude are the measured quantities as shown in Figure 3.2.

In the first use of FDPM techniques for microsphere-based implantable sensor, we immobilized a pH sensitive dye into PEG hydrogel via ester-amine reaction and then placed the PEG microparticles (average particle size 160μm) into tissue-mimicking phantoms (58). Measurements of phase-shift and amplitude of the multiply scattered fluorescent light were successfully obtained as a function of modulation frequency of the incident excitation light. The results showed that at the presence of tissue scattering and absorption, the measured phase-shift value was magnified while the amplitude was decreased. Since the experiments were carried out in a large volume of tissue-mimicking phantom comparing with the size of PEG microparticles, a couple optical diffusion equations were applied to account for the photon propagation and to extract the lifetime change of this pH sensor.

Table 6.1. Review of literature involving microsphere-based fluorescence glucose sensor

Reference	Material	Indicating fluorophore	Particle size, diameter	Immobilized system	Wavelength (ex/em),nm	Comments
Russell *et al.* (1999) (40)	PEG	FITC	2 mm	FITC-ConA/TRITC-dextran	488/500-660	demonstrated entrapment of FRET affinity system into PEG-based hydrogel
McShane *et al* (2000) (41)	PEG	FITC	N/A	FITC-ConA/TRITC-dextran	488/500-600	demonstrated a fiber-optic system for delivery and collection of intensity signal
McShane *et al* (2000) (155)	PEG	FITC	N/A	FITC-ConA/TRITC-dextran	N/A	demonstrated Monte Carlo simulation result of light propagation through human skin with an implantable fluorescent sensor
Russell *et al* (2000) (119)	Poly-L-lysine and calcium alginate	FITC	2.5-3.5 mm	FITC-Succinyl-ConA/TRITC-dextran	488/>500	demonstrated the use of calcium alginate gel and poly-L-lysine coating for entrapment of ConA/dextran
Ballerstadt and Shultz (2000) (43)	Sephadex G200 and G150 with hollow fiber memberane (MWCO 10000)	Alexa488	20-50 μm	Alexa488-ConA/Safranin O/Pararosanilin	488/520	demonstrated the use of Sephadex and dialysis membrane
Xu *et al* (2002) (97)	PEBBLE nanoparticles	$Ru[dpp(SO_3Na)_2]_3Cl_2$	45 nm	GOX/ $Ru[dpp(SO_3Na)_2]_3Cl_2$/Oregon Green 488-dextran	488 nm/>550	demonstrated the use of PEEBLEs incorporating GOX, oxygen sensitive fluorophores, and oxygen-insensitive fluorophores for intracellular glucose imaging. The study used ratiometric measurement

Table 6.1 Continued.

Reference	Material	Indicating fluorophore	Particle size, diameter	Immobilized system	Wavelength (ex/em),nm	Comments
Ballerstadt *et al* (2004) (113)	Sephadex G200 and G150 with cellulose membranes (MWCO 6000-8000)	Alexa647	20-50 μm	Alexa647-ConA	633/670	demonstrated increasing stability of ConA by immobilization of it on Sephadex, temperature influence, photobleaching activities of this sensor
Ballerstadt *et al* (2004) (44)	Sepharose with hollow dialysis fiber (o.d.215 μm, wall thickness 20 μm	Alexa647	45-165 μm	Alexa647-ConA/QSY21-dextran	647/670	demonstrated the use of long wavelength dye and immobilized ConA within Sepharose beads
Chinnayelka and McShane (2004) (55)	Layer-by-layer (LbL) self-assembling polyelectrolyte microsphere	FITC	5 μm	FITC-ConA/TRITC-dextran	488/500-600	demonstrated the use of LbL self-assembling multiple-layer polyelectrolyte microsphere for immobilization of ConA-dextran affinity system
Rossi *et al* (2004) (156)	Fe_3O_4 nanoparticles	$Ru(phen)_3$	20 nm	GOX/$Ru(phen)_3$	460/610	demonstrated the use of magnetite nanoparticle entrapping the GOX and oxygen-sensitive dyes. The study showed improved stability of GOX

Table 6.1 Continued.

Reference	Material	Indicating fluorophore	Particle size, diameter	Immobilized system	Wavelength (ex/em),nm	Comments
Yadavalli *et al* (157)(2005)	PEG	FITC	~100 μm	FITC-dextran/TRITC-ConA	488/>500	demonstrated MC simulation results for predicting optimum hydrogel optical properties, e.g. sphere size, gel chemistry, and scattering anisotropy
Chinnayelka and McShane (83)(2005)	Polyelectrode	FITC	2.2-5.8 μm	FITC-apo-GOX/TRITC-dextran	488 />500	demonstrated the use of apoenzymes encapsulated into polyelectrolyte microbeads
Brown *et al* (38)(2005)	Polyelectrode coated calcium alginate	Ru(dpp)/Alexa488	20-30 μm	Alexa488/Ru(dpp)/GOX	460/500-640	demonstrated experimental results of calcium alginate microsphere entrapping oxygen-sensitive fluorophore and GOX
Brown and McShane (47)(2006)	Polyelectrode coated calcium alginate	Ru(dpp)/Alexa488	N/A	Alexa488/Ru(dpp)/GOX	460 nm/500-640	demonstrated a two-substrate math model for predicting the impact of several sensor parameters, e.g. sphere size, film thickness
Chinnayelka and McShane (115)(2006)	LbL-polyelectrode	Cy5	5 μm	Cy5-apo-GOX/TRITC-dextran	543/560-725	demonstrated the use of long wavelength Cy5 dye to replace previous FITC dye

In an actual implant of glucose sensing microparticles, Pishko and his coworkers showed that implanted polystyrene particles (15 μm in diameter) could be fairly dense packed in a small area at the dermis using insulin needles to inject (157). The implanted microparticles were randomly distributed but closely packed between the dermis and epidermis. The detected fluorescence light signal was influenced not only by the tissue scattering and absorption but also by the microsphere optical properties. Other parameters, such as particle volume fraction, particle size, particle refractive index, and particle configuration, also impacted the measurements.

There are two unique features that exist in this implantable sensing system involving micrometer-sized particles:

(i) Light propagation in this sensing area has two different speeds. Outside microspheres, light travels at a velocity of c/n_{tis}, where n_{tis} is the refractive index of the tissue or tissue phantom; inside microspheres, light travels at a velocity of c/n_{par}, where n_{par} is the refractive index of the microspheres. Table 6.2 lists the refractive index difference between different skin layers and polymer microspheres. Figure 6.1 illustrates the scheme of light propagation in ensemble of these densely packed microspheres.

(ii) The particle size of implantable microspheres (d_p) is much larger than the wavelength of incident light (λ). It is well known that the near-infrared light has the potential to penetrate the skin deeply owing to the low absorption of blood, melanin, and water. The wavelength of incident light used in this implantable sensor is preferably around 600-900 nm (27). However, the size of microspheres may be from several

micrometers to several millimeters (40,157). When particle size is 20 or more times larger than the wavelength, geometric optics may be used to account for light propagation (158). In contrast to the use of Mie theory for small particles (159), where $d_p << \lambda$, geometric optics can be used to describe light propagation when $d_p > \lambda$.

Table 6.2. The refractive index of different skin layers, polymer microspheres and TiO_2.

Name of layer/polymer microsphere	**Refractive index (*n*)**
stratum corneum	1.5 (160)
living epidermis	1.34 (160)
papillary dermis	1.4 (160)
upper blood net dermis	1.39 (160)
reticular dermis	1.4 (160)
deep blood net dermis	1.38 (160)
subcutaneous fat	1.44 (160)
PEG microsphere	1.37 (155) or 1.57 (157)
polystyrene microsphere	1.59 (161)
titanium dioxide (TiO_2) particle	2.4 (162)

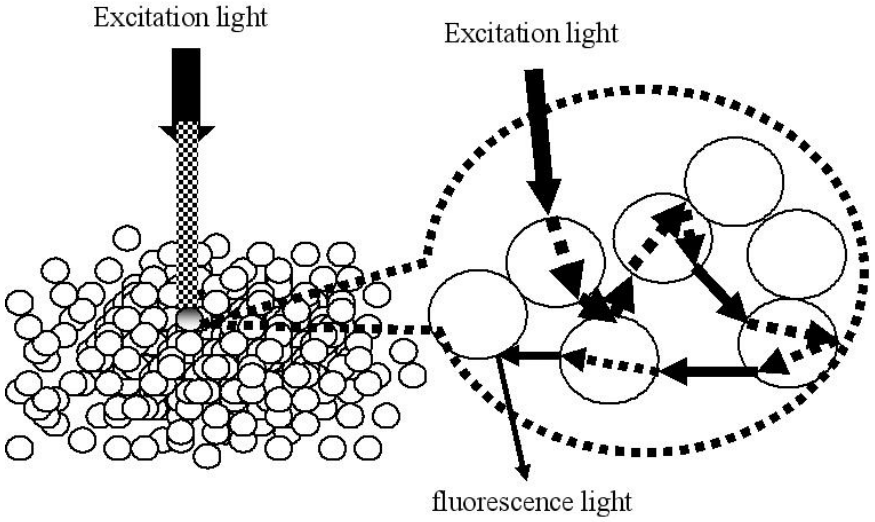

Figure 6.1. Illustration of light propagation in large, densely-packed microspheres with significant refractive index difference with skin layers. The light speed in the microspheres is c/n_{par}, where n_{par} is the refractive index of the microspheres; while outside microspheres, light travels at a velocity of c/n_{tis}, where n_{tis} is the refractive index of the tissue or tissue-mimicking media. The reflection and refraction of light on the boundary follow geometric optics rules.

Monte Carlo computational methods have been applied to a number of problems in light propagation problems where analytical solutions are not available due to complex geometries or boundary conditions as shown in Figure 6.1. McShane and his coworkers applied MC modeling for time-invariant light propagation in an implanted slab of polymer sensor (155). Their model was simply based upon a multi-layered MC code by Wang *et al.*(163) with added fluorescence generation into the program. An eight-layer skin tissue model is used in the simulation. Instead of considering as individual microspheres, the implanted sensor was modeled as a homogenous slab layer of polymer between epidermis and dermis. The output fluorescence intensity was recorded as a function of tissue and sensor optical properties, and thickness of tissue and

of sensor layers. The spatial distribution of the fluorescence intensity signal was also investigated. Even though no experimental results were compared with the generated MC results, the simulation provided useful information for designing an appropriate optical detection system. Yadavalli and his coworkers first developed a MC model to address the impact of microsphere characteristics such as particle size, scattering, fluorescent concentration on detected fluorescence intensity signal (157). They experimentally measured the PEG microsphere isotropic scattering and absorption coefficients using an integrating sphere. The microsphere packing followed a strict Face Centered Cubic (FCC) configuration with volume fraction of 0.74. The time-invariant MC model considered: (i) the light propagation inside and outside the particle; (ii) generated fluorescence light inside the particle; and (iii) reduced fluorescence photon weight after FRET. The model was again not validated by experimental results. Moreover, the refractive index difference between inside and outside microsphere sensor was not addressed.

In this contribution, we describe a novel MC simulation that takes into account: (ii) two different light propagation speeds; (ii) geometric optics; and (iii) fluorescence lifetime within the implantable sensing system. The MC simulation tracks the time-resolved light propagation of both excitation and fluorescence light, and transforms the results into the frequency-domain using Fourier transform. As will be shown herein, FDPM experimental measurements of randomly packed resin particles confirm the simulation results of excitation light propagation. This MC simulation was then used to examine the impact of particle physical properties and fluorophore lifetime on the

measurable fluorescence signals in frequency-domain, namely PS and amplitude (AC). The MC simulation employed a random packed microsphere configuration which was generated from a dynamic simulation (161).

The organization of this section is as follows: In the Materials and Methods section, the new MC model for time-resolved light propagation is described in detail. Then the FDPM experimental set-up using resin microspheres for validation of the MC model is presented. In the Results section, we first present experimental results which validated the MC simulation of excitation light propagation. Then, the influences of particle size, volume fraction, refractive index, fluorescence lifetime on simulated frequency-domain measurements are presented and discussed.

6.2 Materials and Methods

6.2.1 Phantom and Microsphere Structure for MC Simulation

For the purpose of simulation and experimental validation, the microspheres were packed into a cubic volume (4.3 cm×1 cm×1 cm). The size of the cubic is same as the cuvette (Starna Cells Inc., Atascadero, CA). The packing structure was generated by a dynamic simulation program which was developed by Pan *et al.* (161) and described elsewhere by Yang and his coworkers (164,165). Briefly, in this dynamic simulation code, the Newton's second law of motion was solved numerically to track the translational and rotational motion of each numbered particle as it interacted with surrounding neighboring particles. Subsequently, the randomly packed particle structure at equilibrium was used to generate different particle configurations with varying

volume fractions and/or particle sizes by uniform expansion as described elsewhere (166). It was well accepted that simulation of 1024 microspheres with periodic boundary condition could provide a statistically stable structure (165). Based upon the generated microsphere structure, we simulated 4000 microspheres within a $40d_p \times 10d_p \times 10d_p$ cubic with periodic boundary conditions along x, y, and z directions.

6.2.2 Descriptions of the MC Model with Geometric Optics

Our MC model was modified from a previous MC model which tracked the excitation photon trajectories in an infinite and densely packed powder bed (161,166). The code for the Monte Carlo simulations was programmed in Fortran 77 and executed with a SUSE Linux operating system. An infinitely narrow beam with 10^8 photons was launched in each simulation conducted on an AMD dual-CPU and dual-core Opteron 2.8GHz workstation with 8GB RAM. For 10^9 photons, the computational time was around 1.2×10^6 seconds.

In the MC simulation, the information about a photon includes: (i) the photon position vector ($\vec{r}$), (ii) its direction ($\vec{v}$), (iii) its photon weight (w), (iv) net propagation time (t), and (v) the refractive index of the medium on which the photon is located (n_{tis} or n_{par}). The program tracked the photon trajectories one by one. A flowchart outlining the simulation is presented in Figure 6.2. Briefly, the process of tracking a photon package is described below.

Each excitation photon package, with unity weight, is launched on the surface of the cubic phantom. The step size, *s* of the photon is decided by (i) the photon moving

direction , $\vec{v}$, (ii) positions of random-packed microspheres, and (iii) the boundary of the phantom.

For both excitation and fluorescence photons, when the photon moves to the surface of a particle, the program decides whether the photon undergoes reflectance or refraction at each boundary. The probability for reflection is determined from the Fresnel's reflection coefficient $R(\theta_i)$:

$$R(\theta_i) = \frac{1}{2}\left[\frac{sin^2(\theta_i - \theta_t)}{sin^2(\theta_i + \theta_t)} + \frac{tan^2(\theta_i - \theta_t)}{tan^2(\theta_i + \theta_t)}\right] \tag{6.1}$$

where the subscripts $_i$ and $_t$ denotes the incidence and transmission. θ_i and θ_t are the angles of incidence and transmission of photon on the boundary of particle, respectively.

The angle θ_t is obtained from the Snell's law:

$$\sin\theta_t = \frac{n_i}{n_t}\sin\theta_i \tag{6.2}$$

The random number generator used the routine *ran2* described by Press *et al.* (153), which provides more than 2×10^{18} random numbers. The separately generated random numbers (ς_1- ς_4) between 0.0 and 1.0 were used to decide:

(i) Whether the photon underwent reflectance or refraction. If $\varsigma_1 < R(\theta_i)$, then the photon undergoes the reflection on the boundary. Otherwise, the photon underwent the refraction;

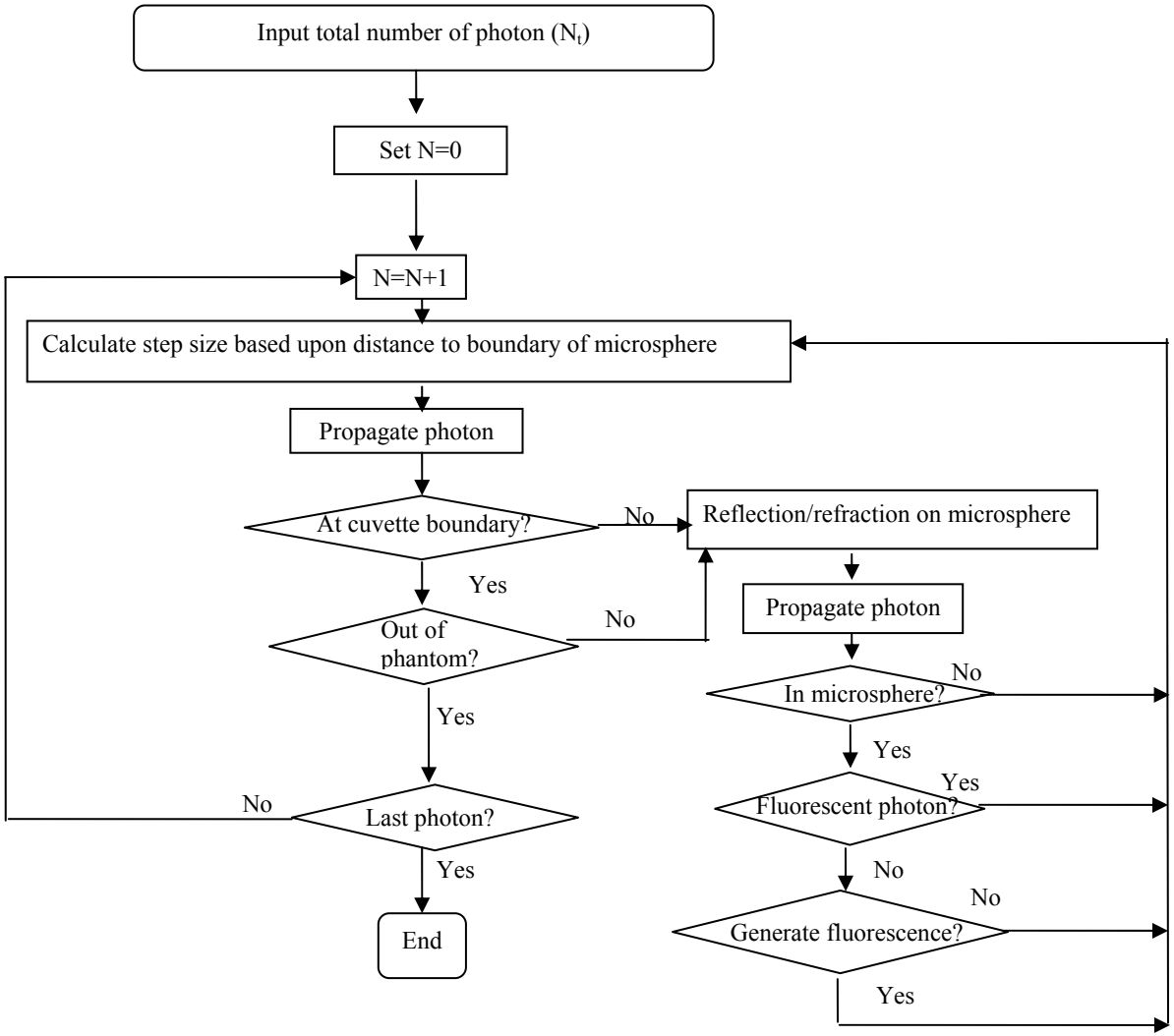

Figure 6.2. Flowchart of MC simulation

(ii) Whether an excitation photon is relabeled as a fluorescence photon when inside the microsphere. If $\varsigma 2 < P$, then the excitation photon is relabeled as fluorescence photon, where P is probability of fluorescence generation (range from 0 to 1). Otherwise, the photon maintains it identity as excitation photon. The probability, P, is the function of quantum efficiency of the fluorophore, Q; the extinction coefficients owing to fluorophores at the excitation wavelength, ξ_{axf}; and the fluorophore concentration within the microsphere *[C]* (167):

$$P = Q \exp\left(-\xi_{axf}\left[C\right]s\right) \tag{6.3}$$

(iii) The time delay t_d during the process of fluorescence is given by (168).

$$t_d = -\ln\left(\varsigma_3\right)\tau_{avg} \tag{6.4}$$

where the average fluorescence lifetime is defined as τ_{avg};

(iv) The propagation direction of the generated fluorescence photon. Since fluorescence is isotropic, there is no preferential direction. The random number ς_4 is used to provide the isotropic fluorescence photon propagation:

$$\mu_x = sin\left(\varsigma_4\pi\right)cos\left(\varsigma_4\pi\right) \tag{6.5}$$

$$\mu_y = sin\left(\varsigma_4\pi\right)sin\left(\varsigma_4\pi\right) \tag{6.6}$$

$$\mu_z = cos\left(\varsigma_4\pi\right) \tag{6.7}$$

This simulation makes the following major assumptions which are applicable to previous experimental results of implantable, microsphere-based fluorescence sensors (40,58):

(i) The fiber optic light source is modeled as an infinite-narrow, unidirectional collimated source. The source light is launched perpendicularly onto the phantom surface. However, our program can simulate arbitrary direction of incident light as well;

(ii) The fluorophores are immobilized inside the microsphere. There is no free fluorophore or fluorophore conjugates in the surrounding medium;

(iii) The absorption from the surrounding tissue is much less than the absorption of the microsphere. Therefore the influence of absorption from the surrounding tissue is not addressed in this treatment.

(iv) The photon weight, w, after each i[th] scattering step is attenuated by (161)

$$\left(\Delta \ln w\right)_i = \begin{bmatrix} -\mu_{a,x,m} \cdot \dfrac{c}{n_{par}} \cdot t_i & \text{in the particle} \\ 0 & \text{in the surrounding medium} \end{bmatrix} \tag{6.8}$$

where the subscript $_{x,m}$ represents excitation and emission. The term μ_a is the absorption coefficient, and t_i, represents the "time-of-flight" associated with the photon scattering step length;

(v) The average lifetime of fluorophore, τ_{avg}, is used in the simulation; and

(vi) The generated fluorophore photon can not be used to regenerate another fluorescent photon.

As shown in Figure 6.3, every surface of the cubic phantom is divided into 10×10 elements. The MC simulation stores the location, time, position, and weight of both excitation and fluorescence photons that reach each detection element.

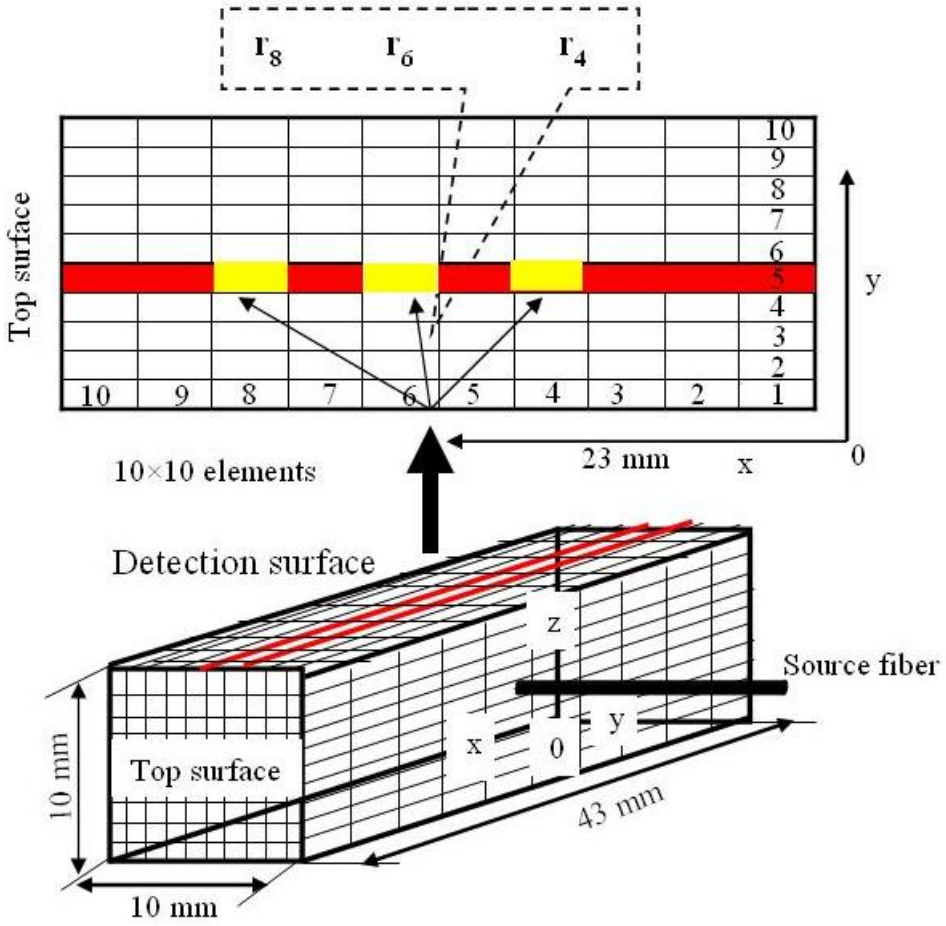

Figure 6.3. Schematic of the phantom for implantable cubic phantom used in MC simulation. The dimension of the phantom is 43×10×10 mm^3. In the MC code, each of the six surfaces on the cubic phantom is divided into 10×10 elements. MC simulation stores the detected both excitation and fluorescence photons with the "time-of-flight" of photon that reach each element. Particularly, PS and AC at elements (1,5) to (10,5) on the detection surface as shown in the top figure are analyzed. The source-detector distance for three positions (positions 4, 6, and 8) are r_4≈10.7 mm, r_6≈7.22 mm, r_8≈12 mm.

6.3 Experimental Section

6.3.1 Materials

Resin microspheres were chosen for the validation experiment because they have spherical shape and are nearly mono-disperse. Resin samples were obtained from Bio-Rad Lab (type AG 1-X8, Hercules, CA) without modification. Figure 6.4 illustrates the micrographs of resin samples under a Nikon microscope (Optiphot2-UD, Nikon, Melville, NY). The average diameter of the dry microspheres was found to be 74 μm (Figure 6.5). Table 6.3 lists the physical properties of resin microspheres used in this study. The absorption coefficient for random close packing (RCP) of resin microspheres was calculated from six times' measurements in a large container (volume> 150mL) using FDPM measurements described by Sun *et al*. (154).

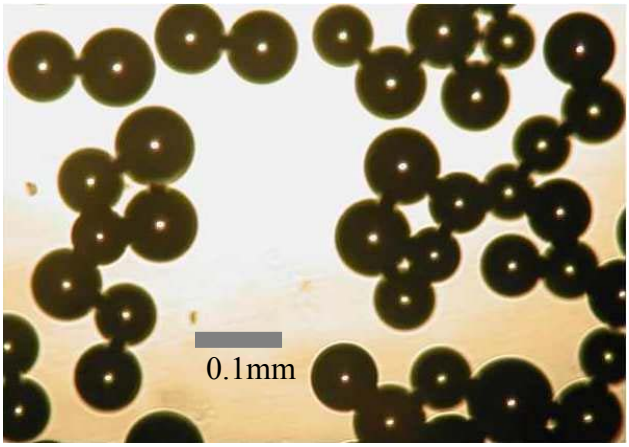

Figure 6.4. Resin microspheres under Nikon microscope. The average particle size is 74 μm ±4 μm as found by measuring 300 randomly sampled beads.

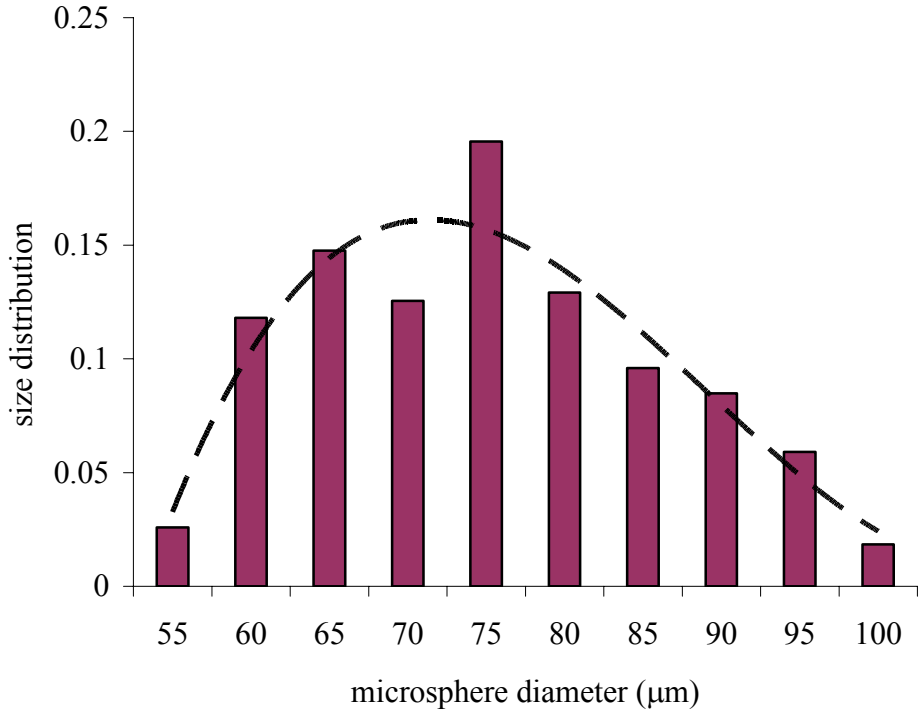

Figure 6.5. Size distribution of the resin microspheres. The bars in the size distribution indicate the fraction of the 300 randomly sampled particles with the corresponding diameter size. The line plot suggests that a normal size distribution was attained.

Table 6.3. Details of physical properties of resin samples

Name	Shape	Average size (μm)	Refractive index	Absorption coefficient for RCP (cm^{-1})	Volume fraction for RCP
resin	Spherical	74	1.59 (161)	0.0129	0.64 (161,169)

6.3.2 Phantom for Implantable Optical Sensors

A glass cuvette (Starna Cells Inc., Atascadero, CA, dimension 4.3×1×1cm) was covered with black tape on all the surfaces except the area for the source and detection fibers as shown in Figure 6.6. Resin microspheres are densely packed in the cuvette.

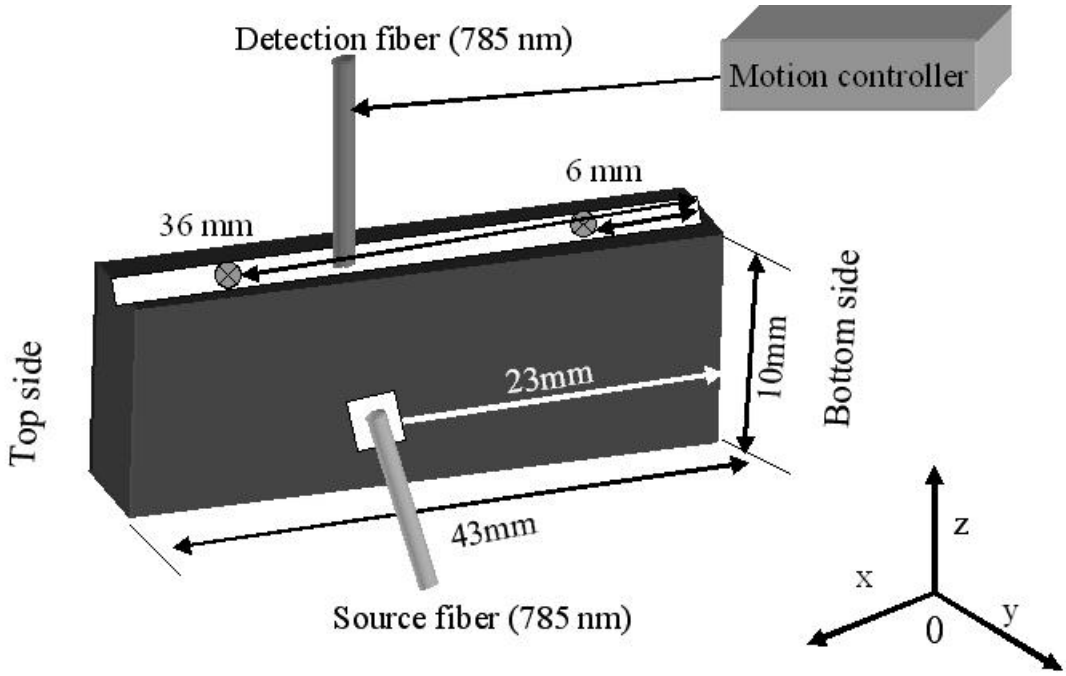

Figure 6.6. Schematic of source and detection fibers' position on the phantom. The source fiber is located in the center of the surface with 23mm distance to the bottom of the cuvette. The detection fiber moves alone the middle line on the detection surface from 2.8 mm to 32.3 mm in increments of 0.5 mm.

6.3.3 FDPM Experiments

The MC simulations were validated using resin measurements were conducted with a FDPM system previously described (159,170). Briefly, intensity modulated light which is emitted from a 785 nm Laser diode (Model# DL7140-201, Thorlabs Inc., Newton, NJ) was directed to a beamsplitter (660-1000 nm, Newport, Irvine, CA). A portion of incident light was directed to a reference PMT (R928, Hamamatsu, Japan) through a 1000 μm-diameter multimode optical fiber (Thorlabs, Inc.), which was outfitted with a band-pass filter (785nm, CVI Laser, Albuquerque, NM). The sampling beam was delivered to the surface of the cubic phantom with a source fiber which

touched the surface perpendicularly. The light propagated through the densely packed resin microspheres and was collected with a detection fiber on the detection surface which was 90˚ from the source fiber as shown in Figures 6.6 and 6.7. The sample signal then passed through a sample PMT (R928, Hamamatsu) which is also outfitted with a 785 band-pass filter. Using a motion controller (ESP300, Newport), the detection fiber was moved on the detection surface in increments of 0.5 mm from 6 mm to 36 mm to the bottom side as shown in Figure 6.6. The sample and reference PMTs were operated at the same modulation frequency plus an offset of 100 Hz for heterodyne detection. Two frequency synthesizers (Marconi Instruments, Mountain view, CA) were phase-locked and provided the modulation frequency for the laser diode and the reference and detection PMTs. The phase-shift and modulation-ratio were taken as a function of modulation frequency (70-100 MHz with a step-size of 5 MHz). Labview 7.0 (National Instruments, Austin, TX) was used to communicate with GPIB card (National instruments) and data acquisition hardware. Six experiments were performed to collect the θ, AC, and DC values. The physical meanings of the θ, AC, and DC are described in section 3.3. The standard deviations of acquired θ, AC, and DC were less than 1% for all the measurements.

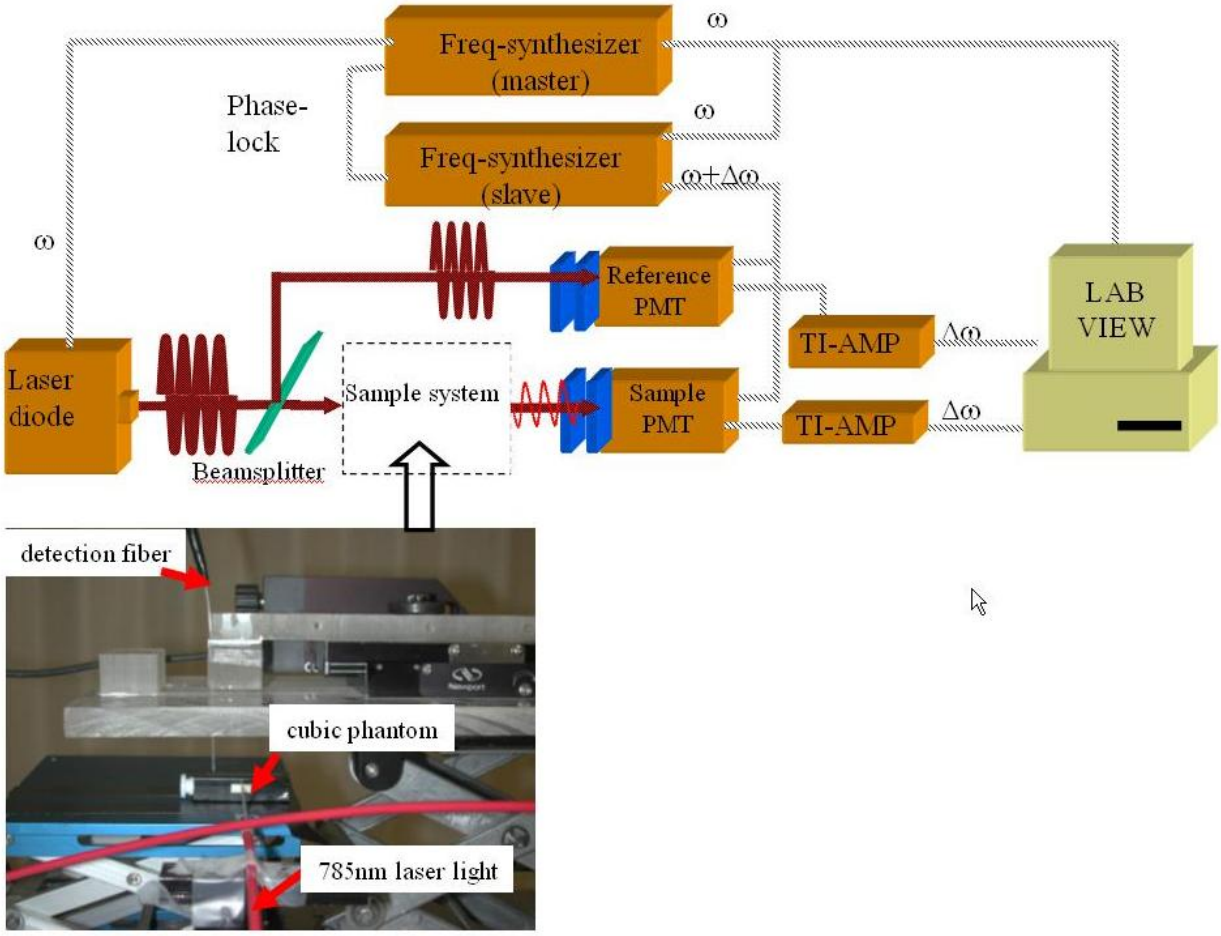

Figure 6.7. (Top) Schematic of FDPM instrumentation set up. (Bottom) picture of the set-up for resin measurements.

6.4 Results and Discussions

6.4.1 FDPM Experimental Validation of the MC Model

Figure 6.8 and Figure 6.9 illustrate the phase-shifts (top figure) and AC (bottom figure) versus the detector position on the detection surface at four different modulation frequencies (70 MHz and 100 MHz, 80 MHz and 90 MHz) for both FDPM experimental and MC simulation results. The amplitude ACs are normalized by the maximum amplitude AC in the elements from the element (1,5) to (10,5) at each modulation frequency. That location of minimum phase shift and maximum amplitude corresponds to the shortest source-detector distance (7.07 mm). If one recalls the physical meaning of the excitation phase shift, $\theta_x(\omega)$, it is related to the mean "time-of-flight" $\langle t \rangle$ (171). It then follows that:

$$\theta_x(\omega) \approx \omega \langle t_x \rangle \propto \omega \frac{r_{s-d}}{\bar{v}} \tag{6.9}$$

where $\langle t_x \rangle$ is the mean transit time of excitation photons from the source to the detector. The term $r_{s\text{-}d}$ is separation distance between source and detection fiber. The term $\bar{v}$ is the mean speed of photon. Hence the phase shift increases with $r_{s\text{-}d}$ as shown in both MC simulation and FDPM experimental results.

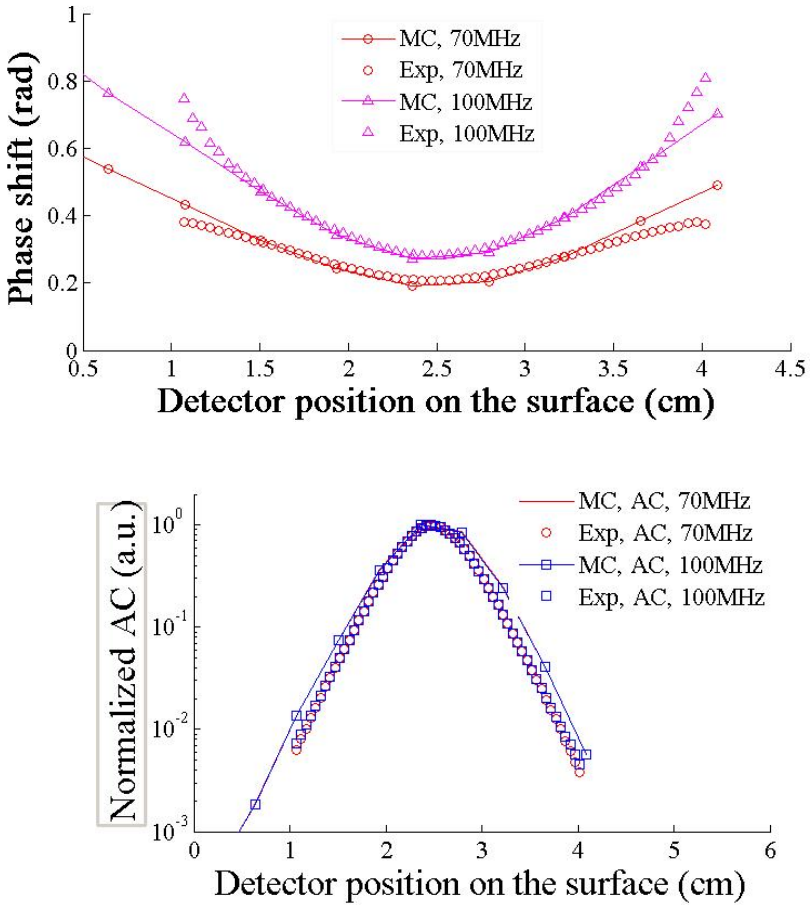

Figure 6.8. (Top) Excitation Phase-shifts and amplitudes at different modulation frequency (70 MHz and 100MHz) as the function of detector position on the detection surface (shown in Figure 6.6). The symbols without lines denote the FDPM experiments results. The lines with symbols denote the MC simulation results. The simulated amplitude AC is normalized by the maximum amplitude AC at each modulation frequency.

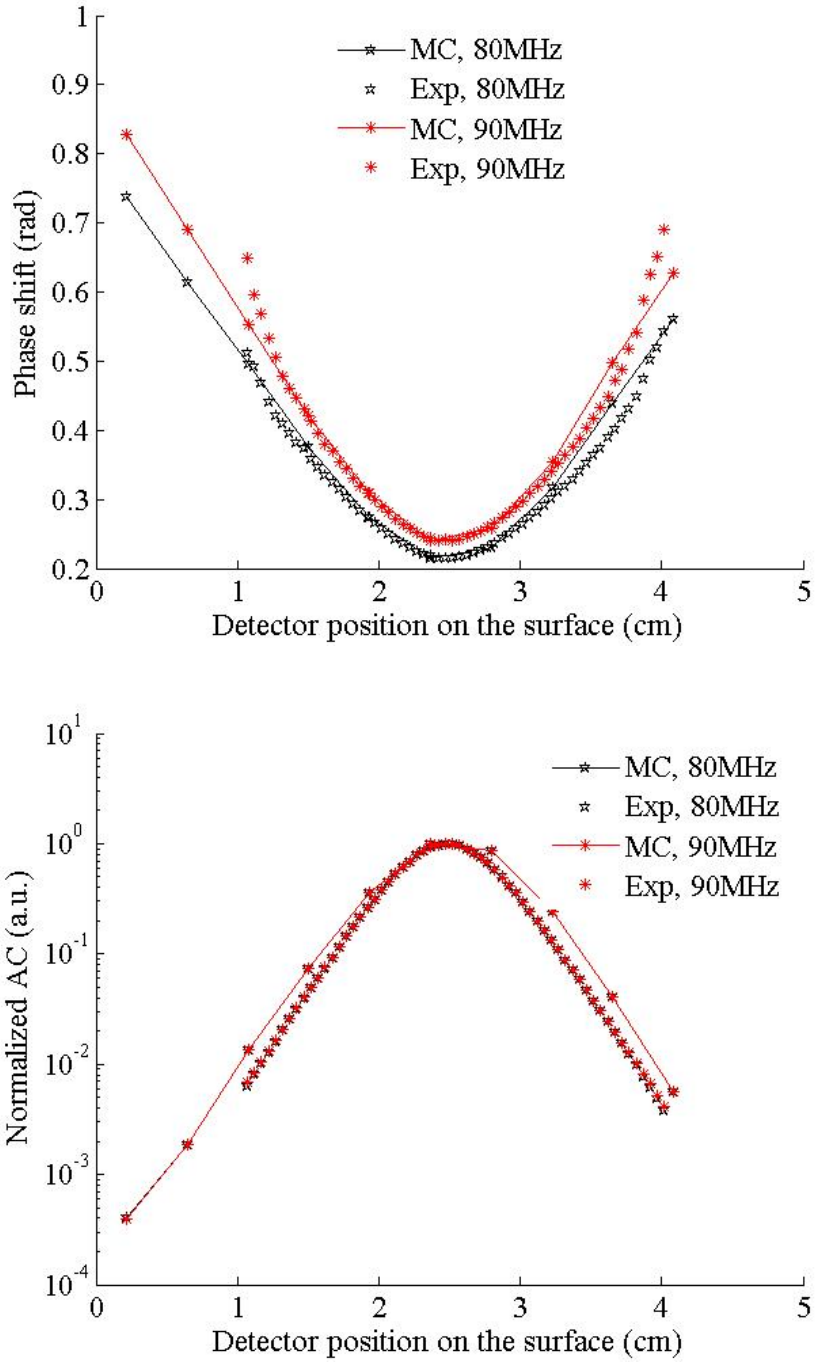

Figure 6.9. (Top) Excitation Phase-shifts and amplitudes at different modulation frequency (70 MHz and 100MHz) as the function of detector position on the detection surface (shown in Figure 6.6). The symbols without lines denote the FDPM experiments results. The lines with symbols denote the MC simulation results. The simulated amplitude AC is normalized by the maximum amplitude AC at each modulation frequency.

To evaluate the difference between MC simulation and FDPM experimental results, we define the phase shift deviation, $\delta\theta_x$ which is calculated as:

$$\Delta\theta_x = \theta_x(FD) - \theta_x(MC) \tag{6.10}$$

where $\theta_x(FD)$ is the FDPM experimental results and $\theta_x(MC)$ is MC simulation results with a cubic spline interpolation scheme decided by the Matlab (Mathworks Inc. Natick, MA). Figure 6.10 shows the change of $\delta\theta_x$ (degree) at different modulation frequencies (70-100MHz) as the function of sixty detector positions on the surface. When detector position was within the range of 1.5-3.5 cm, the $\delta\theta_x$ is less than 1 degree. Table 6.4 demonstrates that the mean $\delta\theta_x$ values at each modulation frequency are 0.3076, 0.7856, 0.9366, and 1.0254 degrees respectively and overall average of $\delta\theta_x$ is only 0.7638°. Figure 6.11 presents the AC_x deviation, δAC_x between the MC simulation and FDPM experimental results.

$$\delta AC_x = [AC_x(FD) - AC_x(MC)]/AC_x(FD) \times 100\% \tag{6.11}$$

When detector position was moved between 1.8 cm and 3.1 cm on the detection surface as shown in Figure 6.3, the δAC_x was less than 40%. Table 6.4 demonstrates that the mean δAC_x values at each modulation frequency are 39.75%, 43.48%, 44.47%, 41.46%, and 42.29% respectively and overall average of δAC_x is 42%.

The differences between MC simulation and FDPM experimental results may result from: (i) the MC simulation model assumes the resin microspheres are monodisperse but in reality, as shown in Figure 6.5, the resin particle exists a normal size- distribution ; (ii) the MC simulation model assumes the surface of the microsphere

are perfectly smooth. However, the resin is made of polystyrene divinylbenzene and is not perfectly smooth on the surface. Therefore the directions for refraction and reflection of each photon package could be a different between the MC simulation and the real packing of the microsphere; (iii) the MC simulation model assumes a perfect uniform volume fraction within the phantom but this might not be realistic; (iv) PS and AC are obtained with a Fourier Transform program using a numerical integration method which approximates the Fourier integral (153).

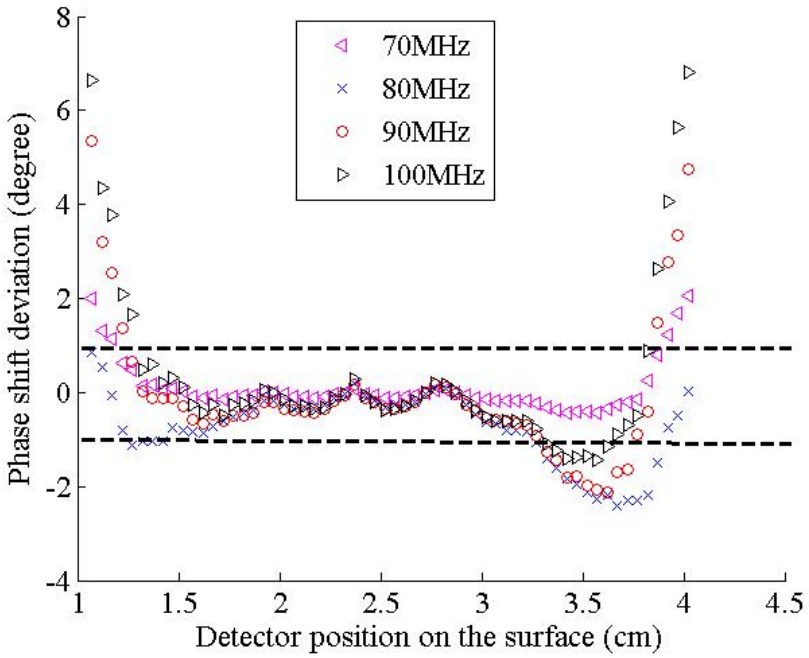

Figure 6.10. Phase shift deviation $\delta\theta$ (degree) at different modulation frequencies (70-100MHz) as the function of sixty detector position on the surface. $\delta\theta=\theta(FD)-\theta(MC)$. The mean $\delta\theta$ values at each modulation frequency are 0.3076, 0.7856, 0.9366, and 1.0254 degree respectively. The overall average of $\delta\theta$ is 0.7638 as shown in Table 6.4.

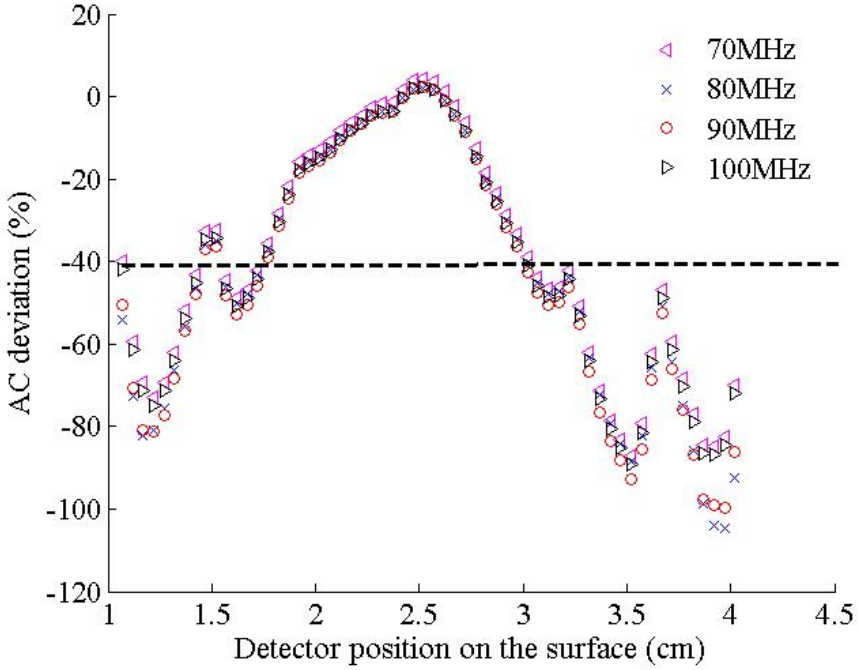

Figure 6.11. AC deviation δAC (%) at different modulation frequencies (70-100MHz) as the function of sixty detector position on the surface. $\delta AC=[AC(FD)-AC(MC)]/AC(FD)$. The mean δAC values at each modulation frequency are 39.75%, 43.48%, 44.47%, and 41.46% respectively. The overall average of δAC is 42.29% as shown in Table 6.4.

Table 6.4. List of averages of δPS and δAC at different modulation frequencies.

	Modulation frequency (MHz)				
deviation average	70	80	90	100	overall average
$\delta\theta$ (degree)	0.3076	0.7856	0.9366	1.0254	0.7638
δAC (%)	41.75	43.48	44.47	41.46	42.29

6.4.2 MC Computational Results for Fluorescence

6.4.2.1 Influence of Microsphere Size

Figures 6.12 and 6.13 show that the fluorescence phase shift θ_f and AC_f versus microsphere size ranging from 26 μm to 180 μm in the cubic phantom at different detection positions and different modulation frequencies. Other simulation conditions are listed in Table 6.5, where f_v is the volume fraction which is equal to the ratio of volume of packed microspheres to the total volume of the cubic phantom (4.3 cm^3). P is the probability for generation of fluorescence. τ_{avg} is the average of lifetime of the fluorophores.

As particle diameter increases, θ_f decreases while AC_f increases. Under this simulation condition, when particle diameter changes from 26 to 100 μm, a ~27-49% decrease in θ_f occurs. When particle size is more than 100 μm, only 5.8%~13% decrease in θ_f occurs. Interestingly, Figure 6.14 demonstrates that θ_f can be described to be proportional to $1/sqrt(d_{par})$. One may recall that the isotropic scattering coefficient μ'_s for microspheres with large particle size ($d_{par} >> \lambda$) is proportional to the d_{par} (172,173):

$$\mu_s^{'} \propto \left(\frac{1}{d_{par}} \right) \tag{6.12}$$

Our pervious FDPM experiments validated the linear relationship between μ'_s and d_{par} (172). The θ_f may be derived from the solution of the coupled fluorescence diffusion equations as:

$$\theta_f \propto \sqrt{\mu_a \mu_s'} \cdot f\left(\mu_a, \omega, \bar{v}, r_{s-d}, \tau, Q\right) \tag{6.13}$$

where $\bar{v}$ is the mean photon speed. The phase shift can be further related to d_{par} from equations 6.12 and 6.13:

$$\theta_f \propto {}^{1}\!\Big/\!_{sqrt\left(d_{par}\right)} \tag{6.14}$$

The MC simulation results in Figure 6.14 validate the linear relationship between θ_f and $1/sqrt(d_{par})$. As we know from Mie theory, particles with size larger than λ will scatter less and hence, scattering coefficients become minimal. Figure 6.13 illustrates the fluorescence amplitude AC_f increases linearly with the particle diameter.

Table 6.5. Simulation conditions for the study of particle size influence on θ_f and amplitude AC_f.

f_v	P	τ_{avg} (ns)	n_{tis}	n_{par}	$\mu_{a,\,par,\,x}$ (cm^{-1})	$\mu_{a,\,par,m}$ (cm^{-1})
0.64	0.5	1.4	1.33	1.59	0.02	0.02

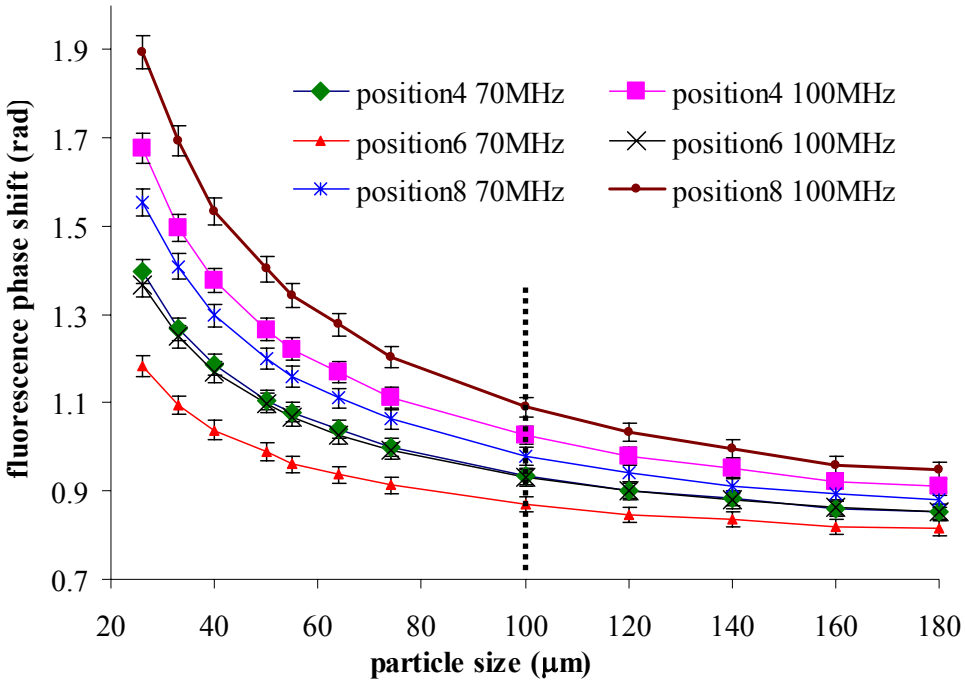

Figure 6.12. Simulation results of fluorescence phase shift θ_f (radius) versus microsphere diameter (μm) at different detection position and different modulation frequencies (MHz). The symbols represent simulation results whereas the trend lines connect simulation results. The error bars denote the uncertainty in simulation for 10^8 photons. The uncertainty was calculated as the standard deviation of the simulation results of three data sets each containing 10^8 photons.

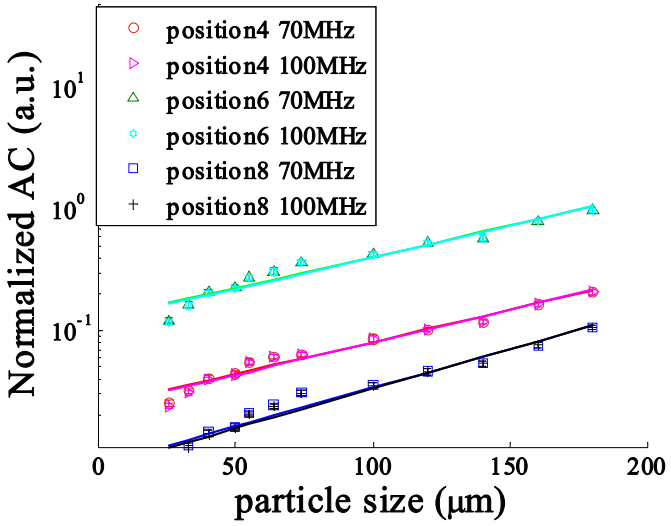

Figure 6.13. Simulation results of normalized fluorescence amplitude AC_f (a.u) versus microsphere diameter (μm) at different detection positions and different modulation frequencies (MHz). The simulated amplitude AC is normalized by the maximum amplitude AC at each modulation frequency. The symbols represent simulation results whereas the solid lines are the linear fits. The uncertainty in simulation for 10^8 photons is 2%.

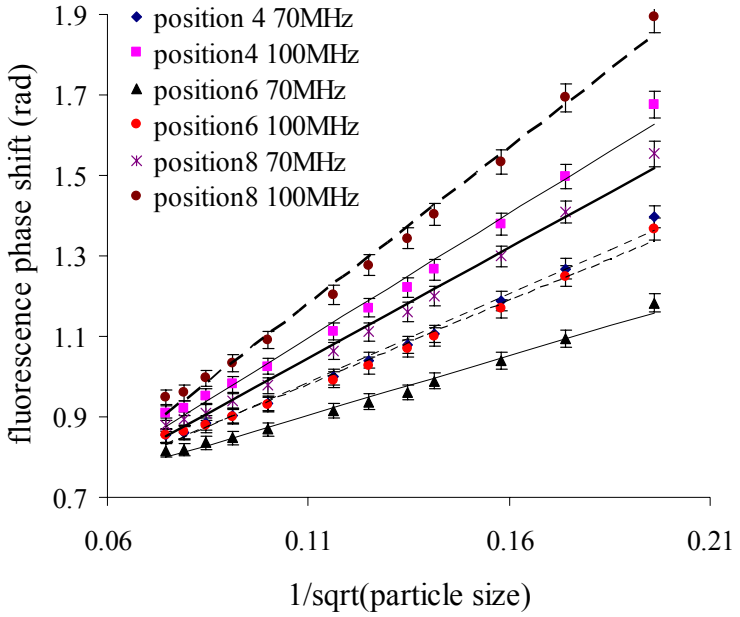

Figure 6.14. Simulation results of fluorescence phase shift θ_f (radius) as a function of 1/sqrt (d_{par} (in diameter, μm)) at different detection position and different modulation frequency (MHz). The symbols represent simulation results whereas the dotted lines are the linear fits. The error bars denote the uncertainty in simulation for 10^8 photons.

6.4.2.2 Influence of Refractive Index of Microspheres

Figures 6.15 and 6.16 illustrated θ_f and AC_f change as a function of refractive index of microspheres ranging from 1.37 to 2.4 at a modulation frequency of 100 MHz. The simulation conditions are listed in Table 6.6.

Table 6.6. Simulation conditions for the study of refractive index influence on θ_f and amplitude AC_f.

	d_{par} (μm)	f_v	P	τ_{avg} (ns)	n_{tis}	$\mu_{a,\,par,\,x}$ (cm^{-1})	$\mu_{a,\,par,m}$ (cm^{-1})	frequency (MHz)
1	74	0.64	0.5	1.4	1.00	0.02	0.02	100
2	160	0.4	0.1	1.4	1.33	0.02	0.02	100
3	26	0.2	0.1	1.4	1.33	0.02	0.02	100

As the refractive index increases, the θ_f increases linearly while the AC_f decreases in all three simulation cases. Under a theoretical analysis of θ_f, we already know from Equation 6.9:

$$\theta_f(\omega) \approx \omega\langle t\rangle + tan^{-1}\omega\langle\tau_{avg}\rangle = \frac{\omega\langle l\rangle}{\bar{v}} + tan^{-1}\omega\langle\tau_{avg}\rangle \tag{6.15}$$

where $\langle l\rangle$ is the mean path length of collected fluorescence photon, which is a function of volume fraction, f_v ,and particle diameter, d_{par} (161). τ_{avg} is the average lifetime of the fluorophore.

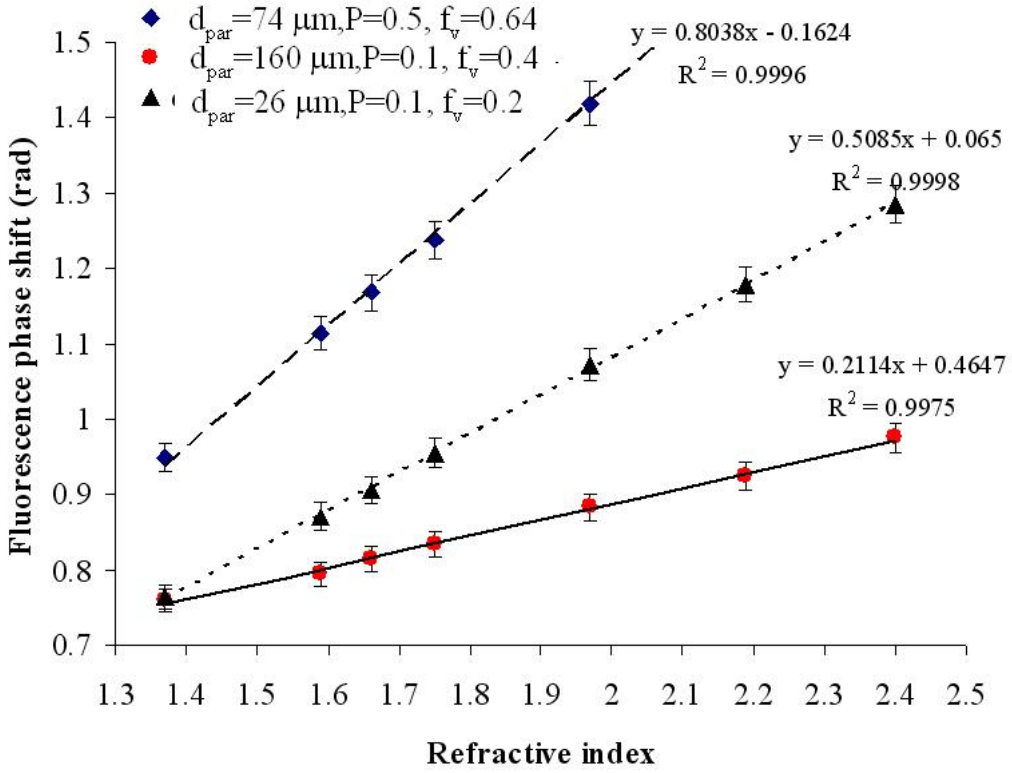

Figure 6.15. Simulation results of fluorescence phase shift θ_f (radius) as a function of refractive index of microspheres at 100MHz and at detection position 4. The symbols represent simulation results whereas the dotted lines are the linear fits. The error bars denote the uncertainty in simulation for 10^8 photons. The uncertainty was calculated as the standard deviation of the simulation results of three data sets each containing 10^8 photons.

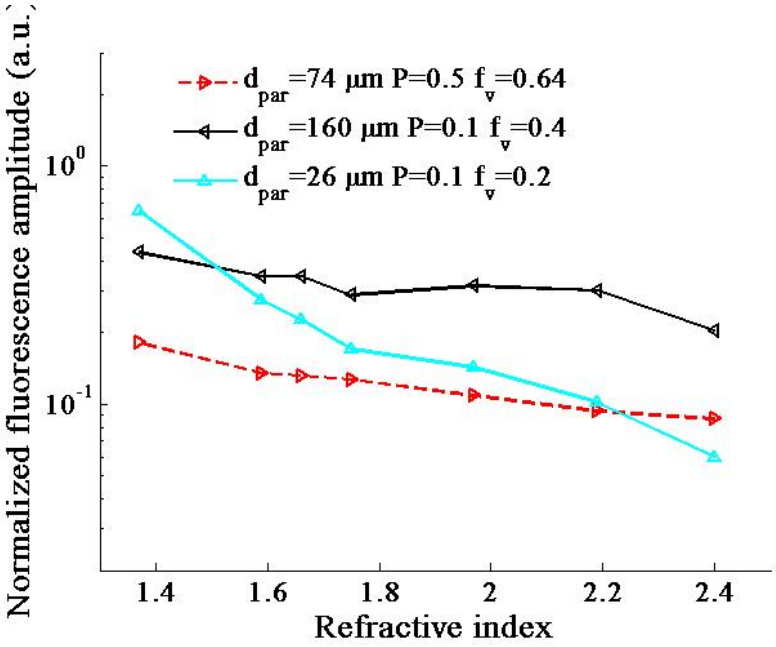

Figure 6.16. Simulation results of normalized fluorescence amplitude AC_f (a.u.) as a function of refractive index of microspheres at 100MHz and at detection position 4. The simulated amplitude AC is normalized by the maximum amplitude AC. The symbols represent simulation results whereas the lines connecting the symbols indicate the trend lines.

The mean "time-of-flight" $<t>$ is equal to (174):

$$\langle t \rangle = \langle t_x \rangle + \langle t_m \rangle \tag{6.16}$$

where $<t_x>$ is the mean "time-of-flight" of excitation photon which propagates from the source to an immobilized fluorophore inside the microsphere, and $<t_m>$ is the mean "time-of-flight" of fluorescence photon which propagates from the fluorophore to the detector.

Then θ_f can be further expanded from Equation 6.16 as:

$$\theta_f(\omega) \approx \frac{\omega\langle l\rangle}{\alpha_{tis}\frac{c}{n_{tis}} + \alpha_{par}\frac{c}{n_{par}}} + tan^{-1}\omega\langle\tau_{avg}\rangle$$
$$\approx \frac{\omega\langle l\rangle}{\alpha_{tis}\frac{c}{n_{tis}} + \alpha_{par}\frac{c}{n_{tis}}\left[1 - \frac{(n_{par} - n_{tis})}{n_{tis}}\right]} + tan^{-1}\omega\langle\tau_{avg}\rangle$$
$$\approx \frac{\omega\langle l\rangle}{\alpha_{tis}\frac{c}{n_{tis}}}\left[1 + \frac{\alpha_{par}}{n_{tis}}(n_{par} - n_{tis})\right] + tan^{-1}\omega\langle\tau_{avg}\rangle \quad (6.17)$$

where c is the light speed in vacuum. α_{tis} and α_{par} are prefactors representing the fractional contribution to the average speed, $\bar{v}$ from the surrounding medium and microsphere, respectively. The sum of α_{tis} and α_{par} is equal to unity. As we can see from Equation 6.17, there is a linear relationship between the refractive index, n_{par}, and θ_f which can be used to explain the results in Figure 6.15. It may be recalled that the higher the refractive index, a stronger scattering effect arises from the microspheres. Therefore the fluorescence amplitude AC_f decreases with increasing refractive index.

6.4.2.3 Influence of Volume Fraction

Figures 6.17 and 6.18 present the θ_f and AC_f change as a function of volume faction of microspheres ranging from 0.1 to 0.64 at modulation frequency of 70 and 100 MHz (in Figure 6.18). The simulation conditions are listed in Table 6.7.

Table 6.7. Simulation conditions for the study of volume fraction influence on θ_f and amplitude AC_f.

	d_{par} (μm)	P	τ_{avg} (ns)	n_{tis}	n_{par}	$\mu_{a,\,par,\,x}$ (cm^{-1})	$\mu_{a,\,par,m}$ (cm^{-1})
1	74	0.05	1.4	1.00	1.59	0.02	0.02

When the refractive index is fixed, θ_f increases but AC_f decreases with increasing volume fraction of the microspheres in the cubic phantom. In a previous study, a quantitative relationship between μ_s' and f_v has been shown as (166):

$$\mu_s' = \frac{1}{d_{par}}\left(a_1 \cdot f_v + a_2 \cdot f_v^2\right) \tag{6.18}$$

where parameters a_1 and a_2 are decided by n_{par}. Accordingly, increasing f_v will increase the isotropic scattering coefficient. Correspondingly, the increase of θ_f with f_v can be explained with Equation 6.13.

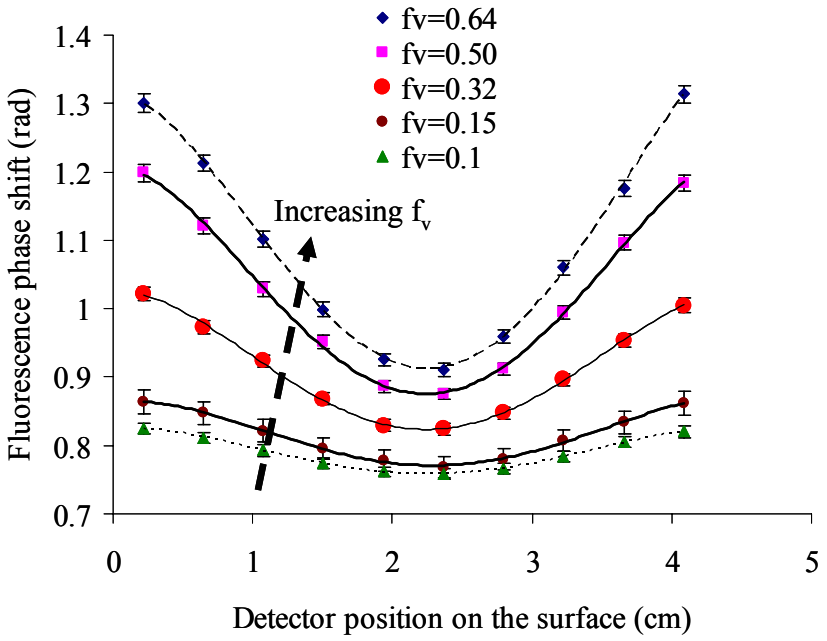

Figure 6.17. Simulation results of θ_f at different detector positions with increasing volume fraction of microspheres in the cubic phantom at modulation frequency of 70 MHz. The symbols denote the simulation results and the lines connecting the symbols denote the trend lines. The error bars represent 1% simulation uncertainty for 10^8 photons.

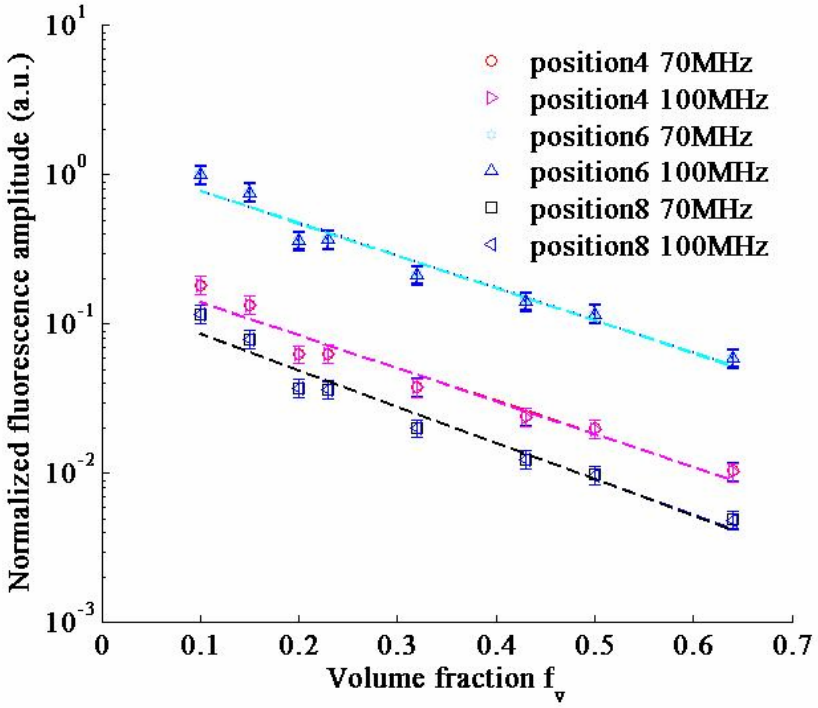

Figure 6.18. Simulation results of AC_f at the function of volume fraction of microspheres in the cubic phantom at modulation frequency of 70 and 100 MHz. The simulated amplitude AC is normalized by the maximum amplitude AC at each modulation frequency. The symbols denote the simulation results and the lines denote the linear fits. The error bars represent 2% simulation uncertainty for 10^8 photons.

6.4.2.4 Influence of Fluorescence Average Lifetime

Figures 6.19 and 6.20 demonstrate the influence of fluorophore average lifetime on the θ_f and AC_f. The simulation conditions are listed in Table 6.8. As the fluorophore average lifetime increases, θ_f increases and AC_f decreases. In the presence of the microspheres, the values of θ_f are magnified by the presence of the microspheres as shown in Figure 6.19. It has been shown in equation 6.15 that θ_f consists three contributions from (i) "time-of-flight" of excitation photons; (ii) time-delay caused by

the lifetime of the excited fluorophore; and (iii) "time-of-flight" of emission photons (174). For the established ConA-dextran affinity system in Section 4, the donor average lifetime change is from 2.79 to 3.16 ns as glucose concentration increases from 0 to 224 mg/dL. The corresponding $\Delta\theta_f$ *(=*θ_f*(224 mg/dL)-*θ_f*(0 mg/dL))* at 100MHz with or without scattering is 0.05 radiuses (=2.9˚) based on the results in Figure 6.19. The presence of scattering doesn't provide better sensitivity for $\Delta\theta_f$.

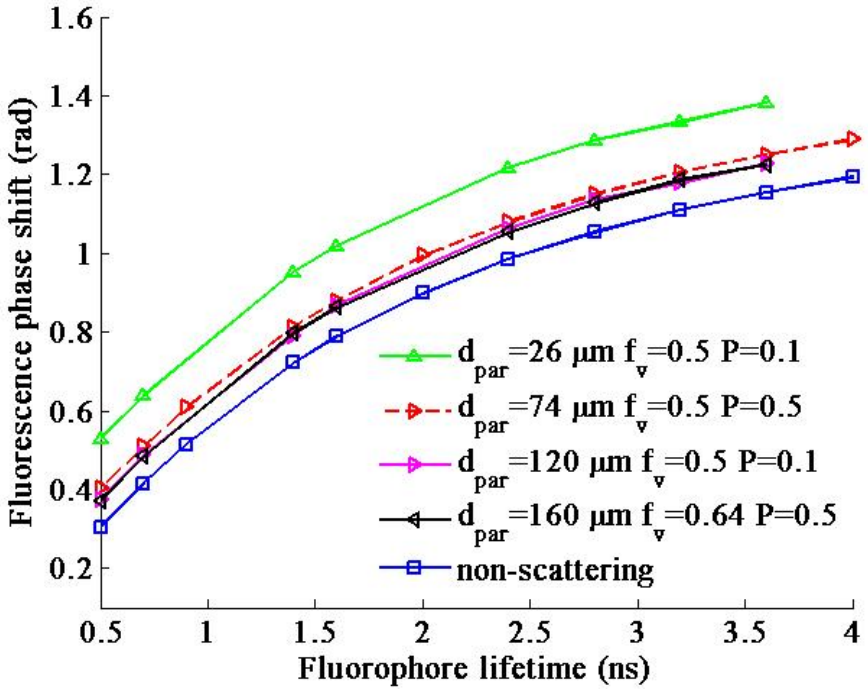

Figure 6.19. Simulation results of fluorescence phase shift θ_f (radius) as a function of fluorophore average lifetime at 100 MHz and detection position 4. The symbols represent simulation results whereas the lines connecting the symbols are the trend lines.

Table 6.8. Simulation conditions for the study of the influence of fluorophore lifetime on θ_f and amplitude AC_f.

	d_{par} (μm)	f_v	P	n_{tis}	n_{par}	$\mu_{a,\,par,\,x}$ (cm^{-1})	$\mu_{a,\,par,m}$ (cm^{-1})	*frequency* (MHz)
1	26	0.5	0.1	1.33	1.59	0.02	0.02	100
2	74	0.5	0.5	1.33	1.59	0.02	0.02	100
3	120	0.5	0.1	1.33	1.59	0.02	0.02	100
4	160	0.64	0.5	1.33	1.59	0.02	0.02	100

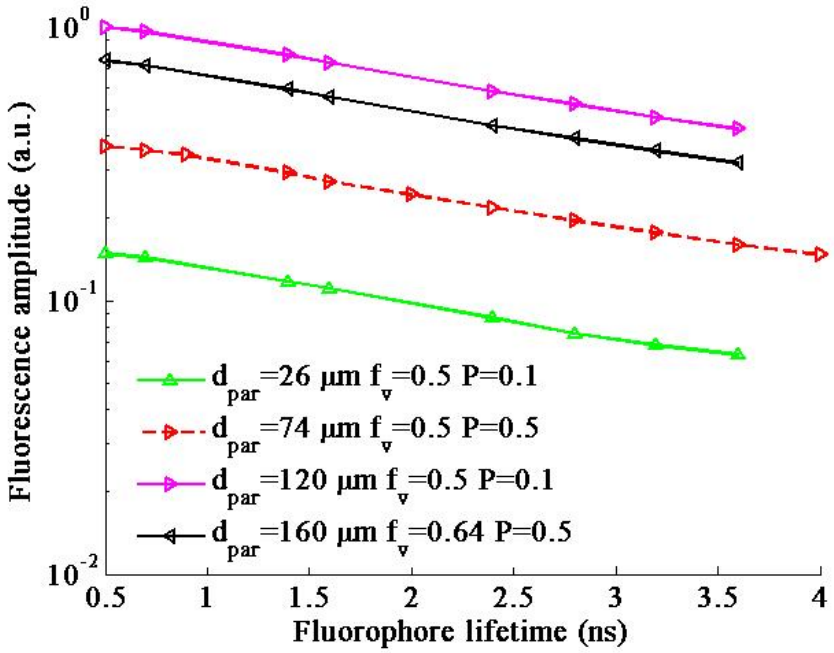

Figure 6.20. Simulation results of normalized fluorescence amplitude AC_f (a.u.) as a function of fluorophore average lifetime at 100MHz modulation frequency and detection position 4. The symbols represent simulation results whereas the lines connecting the symbols indicate the trend lines.

6.5 Summary

We have shown that, a new Monte Carlo simulation for time-resolved light propagation at microsphere-based implantable sensors in a three-dimension cubic phantom. The validity of this model for the excitation light propagation has been demonstrated using a single-pixel FDPM system. Comparison of experimental results and simulation data has shown that (i) our MC model could predict the PS and AC change well; (ii) the mean phase-shift deviation was 0.736°; and (iii) the mean AC deviation was 42%. The model was then applied to investigate the influence of several design parameters on surface detected PS and AC. The parameters included the optical and physical properties of the microsphere: (i) the microsphere diameter; (ii) volume fraction; and (iii) refractive index. We also found that even though the sensitivity of PS change in presence of scattering was the same as the value without scattering, the values of PS were magnified due to the scattering effects. Our work may provide, for the first time, a preliminary basis for designing implantable, microsphere-based optical sensors for lifetime measurements.

7. CONCLUSIONS AND FUTURE WORK

7.1 Conclusions

Microsphere-based implantable optical sensors are promising for future development of a continuous glucose sensing technique. In this work, we tried to develop a new prototype of an implantable fluorescent glucose sensor using FD measurements. The research was carried out into three directions:

(i) We developed a new glucose sensitive ConA-dextran affinity system using long wavelength Alexa Fluor dyes. The glucose sensing range by change of phase-shift could reach up to 750 mg/dL, which is within the physiological range. For the first time, we analyzed the decay kinetics of this FRET system using results from FD measurements. We found that parameter γ in the generalized Förster model provided better sensitivity for evaluating glucose concentration than the raw phase-shift data. Most importantly, our work extended the simple, low-cost FD instrumentation to a potential, powerful "weapon" for ultra-sensitive glucose sensing in the future.

(ii) We experimentally investigated the feasibility of FD lifetime spectroscopy in tissue-mimicing scattering phantom with implantable microsphere-based sensor. We chose a well-characterized pH sensor, C-SNAFL-1, to test the feasibility. Following bioconjugation reactions and photopolymerization, self-made poly(ethylene glycol) microspheres encapsulating the pH fluorophores were prepared and characterized. The FDPM measurements in a phantom with 0.5% polystyrene as scatters showed that: (i) the phase-shifts in presence of scattering were magnified compared with those in

absence of scattering; and (ii) the average fluorophore lifetime, τ_{avg}, which was extracted from measurements using optical diffusion theory, could be used to quantitatively measure pH change.

(iii) A new Monte Carlo model was developed and experimentally validated for time-resolved light propagation in microsphere-based sensors. The model accounted for the refractive index mismatch between the polymeric beads and the surrounding media. Geometric optics was used to trace photon tracks instead of Mie theory due to the large size of the microsphere compared to the wavelength of incident light. Using this model, the influence of particle size, volume fraction, refractive index, and fluorophore lifetime on phase-shift signal was presented. This model may provide an effective tool for future design of implantable microsphere-based sensors.

7.2 Future Work

Future work focusing on translating the FD lifetime spectroscopy into animal studies includes:

(i) Designing a new FRET glucose-sensitive affinity system which either attaches on polymer microspheres surface or is encapsulated into polymer beads.

(ii) Developing FD measurements in non-scattering solution that could be carried out to test the phase-shift response to glucose concentration change. The glucose sensing range may be adjusted by changing the composition of the affinity system as shown in section 4.2.4. The stability, reversibility, and time response of the system would be evaluated.

(iii) FD measurements in a tissue-mimicking scattering phantom should be evaluated out to show the feasibility of quantitative glucose sensing.

Lastly, (iv) the injection of microsphere sensors into a pig skin tissue should be performed. Glucose monitoring using FD lifetime spectroscopy should be examined.

REFERENCES

1. Klonoff, D. C. (2005) Continuous glucose monitoring - roadmap for 21st century diabetes therapy. *Diabetes Care* **28,** 1231-1239.

2. Sieg, A., R. H. Guy, and M. B. Delgado-Charro (2005) Noninvasive and minimally invasive methods for transdermal glucose monitoring. *Diabetes Technol. Ther.* **7,** 174-97.

3. Calne, R. (2005) Cell transplantation for diabetes. *Philos. Trans. R. Soc. Lond. B Biol. Sci.* **360,** 1769-74.

4. Assady, S., G. Maor, M. Amit, J. Itskovitz-Eldor, K. L. Skorecki, and M. Tzukerman (2001) Insulin production by human embryonic stem cells. *Diabetes* **50,** 1691-1697.

5. Renard, E. (2002) Implantable closed-loop glucose-sensing and insulin delivery: the future for insulin pump therapy. *Curr. Opin. Pharmacol.* **2,** 708-716.

6. Pickup, J. C., and G. Williams (2003) *Textbook of Diabetes.* Blackwell Science, London.

7. McNichols, R. J., and G. L. Cote (2000) Optical glucose sensing in biological fluids: an overview. *J. Biomed. Opt.* **5,** 5-16.

8. Cote, G. L., and R. J. McNichols (2003) Glucose diagnostics. In *Biomedical Photonics Handbook* (Edited by T. Vo-Dinh), pp. 1-19. CRC Press, New York, NY.

9. Shamoon, H., H. Duffy, N. Fleischer, S. Engel, P. Saenger, M. Strelzyn, and C. Siebert (1993) The effect of intensive treatment of diabetes on the development and progression of long-term complications in insulin-dependent diabetes-mellitus. *New. Engl. J. Med.* **329,** 977-986.

10. Pickup, J. C., F. Hussain, N. D. Evans, and N. Sachedina (2005) In vivo glucose monitoring: the clinical reality and the promise. *Biosens. Bioelectron.* **20,** 1897-902.

11. Heinemann, L., and T. Koschinsky (2002) Continuous glucose monitoring: an overview of today's technologies and their clinical applications. *Int. J. Clin. Pract. Suppl.* **11,** 75-9.

12. Malin, S. F., T. L. Ruchti, T. B. Blank, S. N. Thennadil, and S. L. Monfre (1999) Noninvasive prediction of glucose by near-infrared diffuse reflectance spectroscopy. *Clin. Chem.* **45,** 1651-1658.

13. Hull, E. L., M. N. Ediger, A. H. T. Unione, E. K. Deemer, M. L. Stroman, and J. W. Baynes (2004) Noninvasive, optical detection of diabetes: model studies with porcine skin. *Opt. Express* **12,** 4496-4510.

14. Arnold, M. A. (1996) Non-invasive glucose monitoring. *Curr. Opin. Biotech.* **7,** 46-49.

15. Berger, A. J., T. W. Koo, I. Itzkan, G. Horowitz, and M. S. Feld (1999) Multicomponent blood analysis by near-infrared Raman spectroscopy. *Appl. Optics* **38,** 2916-2926.

16. Aslan, K., J. R. Lakowicz, and C. D. Geddes (2004) Nanogold plasmon resonance based glucose sensing. *Anal. Biochem.* **330,** 145-55.

17. Aslan, K., J. R. Lakowicz, and C. D. Geddes (2004) Tunable plasmonic glucose sensing based on the dissociation of Con A-aggregated dextran-coated gold colloids. *Anal. Chim. Acta* **517,** 139-144.

18. Svitel, J., A. Dzgoev, K. Ramanathan, and B. Danielsson (2000) Surface plasmon resonance based pesticide assay on a renewable biosensing surface using the reversible concanavalin A monosaccharide interaction. *Biosens. Bioelectron.* **15,** 411-415.

19. Cameron, B. D., and G. L. Cote (1997) Noninvasive glucose sensing utilizing a digital closed-loop polarimetric approach. *IEEE T. Bio-Med. Eng.* **44,** 1221-1227.

20. Kohl, M., M. Cope, M. Essenpreis, and D. Bocker (1994) Influence of glucose-concentration on light-scattering in tissue-simulating phantoms. *Opt. Lett.* **19,** 2170-2172.

21. Maier, J. S., S. A. Walker, S. Fantini, M. A. Franceschini, and E. Gratton (1994) Possible correlation between blood-glucose concentration and the reduced scattering coefficient of tissues in the near-Infrared. *Opt. Lett.* **19,** 2062-2064.

22. Kohl, M., M. Essenpreis, and M. Cope (1995) The influence of glucose-concentration upon the transport of light in tissue-simulating phantoms. *Phys. Med. Biol.* **40,** 1267-1287.

23. Larin, K. V., M. Motamedi, T. V. Ashitkov, and R. O. Esenaliev (2003) Specificity of noninvasive blood glucose sensing using optical coherence tomography technique: a pilot study. *Phys. Med. Biol.* **48,** 1371-1390.

24. Khalil, O. S. (2004) Non-invasive glucose measurement technologies: an update from 1999 to the dawn of the new millennium. *Diabetes Technol. Ther.* **6,** 660-697.

25. Wickramasinghe, Y., Y. Yang, and S. A. Spencer (2004) Current problems and potential techniques in in vivo glucose monitoring. *J. Fluoresc.* **14,** 513-520.

26. Lakowicz, J. R. (1999) *Principles of Fluorescence Spectroscopy.* Kluwer Academic/Plenum Publishers, New York, NY.

27. Richards-Kortum, R., and E. Sevick-Muraca (1996) Quantitative optical spectroscopy for tissue diagnosis. *Annu. Rev. Phys. Chem.* **47,** 555-606.

28. Thompson, R. B., and J. R. Lakowicz (1993) Fiber optic pH sensor based on phase fluorescence lifetimes. *Anal. Chem.* **65,** 853-856.

29. Draxler, S., and M. E. Lippitsch (1995) PH sensors using fluorescence decay time. *Sensor Actuat. B-Chem.* **29,** 199-203.

30. Mayer, R. H., J. S. Reynolds, and E. N. Sevick-Muraca (1999) Measurement of the fluorescence lifetime in scattering media lay frequency-domain photon migration. *Appl. Optics* **38,** 4930-4938.

31. Lippitsch, M. E., J. Pusterhofer, M. J. P. Leiner, and O. S. Wolfbeis (1988) Fibre-optic oxygen sensor with the fluorescence decay time as the information carrier. *Anal. Chim. Acta.* **205,** 1-6.

32. Lakowicz, J. R., and H. Szmacinski (1993) Fluorescence lifetime-based sensing of ph, Ca-2(+), K+ and glucose. *Sensor. Actuat. B-Chem.* **11,** 133-143.

33. Takahashi, A., P. Camacho, J. D. Lechleiter, and B. Herman (1999) Measurement of intracellular calcium. *Physiol. Rev.* **79,** 1089-1125.

34. Rolinski, O. J., and D. J. S. Birch (1999) A fluorescence lifetime sensor for Cu(I) ions. *Meas. Sci. Technol.* **10,** 127-136.

35. Thompson, R. B., and M. W. Patchan (1995) Lifetime-based fluorescence energy-transfer biosensing of zinc. *Anal. Biochem.* **227,** 123-128.

36. Sevick-Muraca, E. M., and C. L. Burch (1994) Origin of phosphorescence signals reemitted from tissues. *Opt. Lett.* **19,** 1928-1930.

37. Albisser, A. M., B. S. Leibel, T. G. Ewart, Z. Davidovac, C. K. Botz, and W. Zingg (1974) An artificial endocrine pancreas. *Diabetes* **23,** 389-96.

38. Brown, J. Q., R. Srivastava, and M. J. McShane (2005) Encapsulation of glucose oxidase and an oxygen-quenched fluorophore in polyelectrolyte-coated calcium alginate microspheres as optical glucose sensor systems. *Biosens. Bioelectron.* **21,** 212-216.

39. Mellott, M. B., K. Searcy, and M. V. Pishko (2001) Release of protein from highly cross-linked hydrogels of poly(ethylene glycol) diacrylate fabricated by UV polymerization. *Biomaterials* **22,** 929-941.

40. Russell, R. J., M. V. Pishko, C. C. Gefrides, M. J. McShane, and G. L. Cote (1999) A fluorescence-based glucose biosensor using concanavalin A and dextran encapsulated in a poly(ethylene glycol) hydrogel. *Anal. Chem.* **71,** 3126-3132.

41. McShane, M. J., R. J. Russell, M. V. Pishko, and L. G. Cote (2000) Glucose monitoring using implanted fluorescent microspheres. *IEEE Eng. Med. Biol.* **19,** 36-45.

42. Russell, R. J., A. C. Axel, K. L. Shields, and M. V. Pishko (2001) Mass transfer in rapidly photopolymerized poly(ethylene glycol) hydrogels used for chemical sensing. *Polymer* **42,** 4893-4901.

43. Ballerstadt, R., and J. S. Schultz (2000) A fluorescence affinity hollow fiber sensor for continuous transdermal glucose monitoring. *Anal. Chem.* **72,** 4185-4192.

44. Ballerstadt, R., A. Gowda, and R. McNichols (2004) Fluorescence resonance energy transfer-based near-infrared fluorescence sensor for glucose monitoring. *Diabetes Technol. Ther.* **6,** 191-200.

45. Lyandres, O., N. C. Shah, C. R. Yonzon, J. T. Walsh, M. R. Glucksberg, and R. P. Van Duyne (2005) Real-time glucose sensing by surface-enhanced Raman spectroscopy in bovine plasma facilitated by a mixed decanethiol/mercaptohexanol partition layer. *Anal. Chem.* **77,** 6134-6139.

46. Blagoi, G., N. Rosenzweig, and Z. Rosenzweig (2005) Design, synthesis, and application of particle-based fluorescence resonance energy transfer sensors for carbohydrates and glycoproteins. *Anal. Chem.* **77,** 393-399.

47. Brown, J. Q., and M. J. McShane (2006) Modeling of spherical fluorescent glucose microsensor systems: design of enzymatic smart tattoos. *Biosens. Bioelectron.* **21,** 1760-1769.

48. Schultz, J. S., and G. Sims (1979) Affinity sensors for individual metabolites. *Biotechnol. Bioeng. Symp.* **9,** 65-71.

49. Schultz, J. S., S. Mansouri, and I. J. Goldstein (1982) Affinity sensor - a new technique for developing implantable sensors for glucose and other metabolites. *Diabetes Care* **5,** 245-253.

50. Rolinski, O. J., D. J. S. Birch, L. J. McCartney, and J. C. Pickup (2000) A time-resolved near-infrared fluorescence assay for glucose: opportunities for trans-dermal sensing. *J. Photoch. Photobio. B* **54,** 26-34.

51. Tolosa, L., H. Malak, G. Raob, and J. R. Lakowicz (1997) Optical assay for glucose based on the luminescence decay time of the long wavelength dye Cy5 (TM). *Sensor. Actuat. B-Chem.* **45,** 93-99.

52. Ballerstadt, R., and J. S. Schultz (1997) Competitive-binding assay method based on fluorescence quenching of ligands held in close proximity by a multivalent receptor. *Anal. Chim. Acta* **345,** 203-212.

53. McCartney, L. J., J. C. Pickup, O. J. Rolinski, and D. J. S. Birch (2001) Near-infrared fluorescence lifetime assay for serum glucose based on allophycocyanin-labeled concanavalin A. *Anal. Biochem.* **292,** 216-221.

54. Lakowicz, J. R., and B. Maliwal (1993) Optical sensing of glucose using phase-modulation fluorometry. *Anal. Chim. Acta.* **271,** 155-164.

55. Chinnayelka, S., and M. J. McShane (2004) Glucose-sensitive nanoassemblies comprising affinity-binding complexes trapped in fuzzy microshells. *J. Fluoresc.* **14,** 585-595.

56. Zhu, H. G., R. Srivastava, J. Q. Brown, and M. J. McShane (2005) Combined physical and chemical immobilization of glucose oxidase in alginate microspheres improves stability of encapsulation and activity. *Bioconjugate Chem.* **16,** 1451-1458.

57. Liang, F., T. S. Pan, and E. M. Sevick-Muraca (2005) Measurements of FRET in a glucose-sensitive affinity system with frequency-domain lifetime spectroscopy. *Photochem. Photobiol.* **81,** 1386-1394.

58. Kuwana, E., F. Liang, and E. M. Sevick-Muraca (2004) Fluorescence lifetime spectroscopy of a pH-sensitive dye encapsulated in hydrogel beads. *Biotechnol. Progr.* **20,** 1561-1566.

59. Alexeev, V. L., A. C. Sharma, A. V. Goponenko, S. Das, I. K. Lednev, C. S. Wilcox, D. N. Finegold, and S. A. Asher (2003) High ionic strength glucose-sensing photonic crystal. *Anal. Chem.* **75,** 2316-2323.

60. Holtz, J. H., J. S. W. Holtz, C. H. Munro, and S. A. Asher (1998) Intelligent polymerized crystalline colloidal arrays: Novel chemical sensor materials. *Anal. Chem.* **70,** 780-791.

61. Graaff, R., J. G. Aarnoudse, J. R. Zijp, P. M. A. Sloot, F. F. M. Demul, J. Greve, and M. H. Koelink (1992) Reduced light-scattering properties for mixtures of spherical-particles - a simple approximation derived from Mie calculations. *Appl. Optics* **31,** 1370-1376.

62. Bruulsema, J. T., J. E. Hayward, T. J. Farrell, M. S. Patterson, L. Heinemann, M. Berger, T. Koschinsky, J. Sandahl-Christiansen, and H. Orskov (1997) Correlation between blood glucose concentration in diabetics and noninvasively measured tissue optical scattering coefficient. *Opt. Lett.* **22,** 190-192.

63. Tuchin, V. V. (2005) Optical clearing of tissues and blood using the immersion method. *J. Phys. D Appl. Phys.* **38,** 2497-2518.

64. Larin, K. V., M. S. Eledrisi, M. Motamedi, and R. O. Esenaliev (2002) Noninvasive blood glucose monitoring with optical coherence tomography - A pilot study in human subjects. *Diabetes Care* **25,** 2263-2267.

65. Cote, G. L. (2001) Noninvasive and minimally-invasive optical monitoring technologies. *J. Nutr.* **131,** 1596s-1604s.

66. Arimoto, H., M. Tarumi, and Y. Yamada (2003) Temperature-insensitive measurement of glucose concentration based on near infrared spectroscopy and partial least squares analysis. *Opt. Rev.* **10,** 74-76.

67. Burmeister, J. J., and M. A. Arnold (1999) Evaluation of measurement sites for noninvasive blood glucose sensing with near-infrared transmission spectroscopy. *Clin. Chem.* **45,** 1621-1627.

68. Khalil, O. S. (1999) Spectroscopic and clinical aspects of noninvasive glucose measurements. *Clin. Chem.* **45,** 165-177.

69. Heinemann, L., G. Schmelzeisen-Redeker, and N.-I. T. Force (1998) Non-invasive continuous glucose monitoring in Type I diabetic patients with optical glucose sensors. *Diabetologia* **41,** 848-854.

70. Koschinsky, T., and L. Heinemann (2001) Sensors for glucose monitoring: technical and clinical aspects. *Diabetes-Metab. Res.* **17,** 113-123.

71. Alivisatos, P. (2004) The use of nanocrystals in biological detection. *Nat. Biotechnol.* **22,** 47-52.

72. Alexeev, V., A. Sharma, I. Lednev, C. Wilcox, D. Finegold, and S. A. Asher (2002) Intelligent polymerized crystalline colloidal array photonic crystal glucose sensors. *Abstr. Pap. Am. Chem. S.* **224,** U116-U116.

73. Alexeev, V. L., S. Das, D. N. Finegold, and S. A. Asher (2004) Photonic crystal glucose-sensing material for noninvasive monitoring of glucose in tear fluid. *Clin. Chem.* **50,** 2353-2360.

74. Kinnunen, M., and R. Myllyla (2005) Effect of glucose on photoacoustic signals at the wavelengths of 1064 and 532 nm in pig blood and intralipid. *J. Phys. D Appl. Phys.* **38,** 2654-2661.

75. MacKenzie, H. A., H. S. Ashton, S. Spiers, Y. C. Shen, S. S. Freeborn, J. Hannigan, J. Lindberg, and P. Rae (1999) Advances in photoacoustic noninvasive glucose testing. *Clin. Chem.* **45,** 1587-1595.

76. Ye, K. M., and J. S. Schultz (2003) Genetic engineering of an allosterically based glucose indicator protein for continuous glucose monitoring by fluorescence resonance energy transfer. *Anal. Chem.* **75,** 3451-3459.

77. Tolosa, L., I. Gryczynski, L. R. Eichhorn, J. D. Dattelbaum, F. N. Castellano, G. Rao, and J. R. Lakowicz (1999) Glucose sensor for low-cost lifetime-based sensing using a genetically engineered protein. *Anal. Biochem.* **267,** 114-120.

78. Hsieh, H. V., Z. A. Pfeiffer, T. J. Amiss, D. B. Sherman, and J. B. Pitner (2004) Direct detection of glucose by surface plasmon resonance with bacterial glucose/galactose-binding protein. *Biosens. Bioelectron.* **19,** 653-660.

79. D'Auria, S., and J. R. Lakowicz (2001) Enzyme fluorescence as a sensing tool: new perspectives in biotechnology. *Curr. Opin. Biotech.* **12,** 99-104.

80. D'Auria, S., P. Herman, M. Rossi, and J. R. Lakowicz (1999) The fluorescence emission of the apo-glucose oxidase from Aspergillus niger as probe to estimate glucose concentrations. *Biochem. Bioph. Res. Co.* **263,** 550-553.

81. D'Auria, S., N. Di Cesare, Z. Gryczynski, I. Gryczynski, M. Rossi, and J. R. Lakowicz (2000) A thermophilic apoglucose dehydrogenase as nonconsuming glucose sensor. *Biochem. Bioph. Res. Co.* **274,** 727-731.

82. D'Auria, S., N. DiCesare, M. Staiano, Z. Gryczynski, M. Rossi, and J. R. Lakowicz (2002) A novel fluorescence competitive assay for glucose determinations by using a thermostable glucokinase from the thermophilic microorganism Bacillus stearothermophilus. *Anal. Biochem.* **303,** 138-144.

83. Chinnayelka, S., and M. J. McShane (2005) Microcapsule biosensors using competitive binding resonance energy transfer assays based on apoenzymes. *Anal. Chem.* **77,** 5501-5511.

84. Chinnayelka, S., and M. J. McShane (2004) Resonance energy transfer nanobiosensors based on affinity binding between apo-enzyme and its substrate. *Biomacromolecules* **5,** 1657-1661.

85. Wang, W., X. M. Gao, and B. H. Wang (2002) Boronic acid-based sensors. *Curr. Org. Chem.* **6,** 1285-1317.

86. James, T. D., K. R. A. S. Sandanayake, and S. Shinkai (1994) Novel photoinduced electron-transfer sensor for saccharides based on the interaction of boronic acid and amine. *J. Chem. Soc. Chem. Comm.* 477-478.

87. James, T. D., K. R. A. S. Sandanayake, and S. Shinkai (1996) Saccharide sensing with molecular receptors based on boronic acid. *Angew. Chem. Int. Edit.* **35,** 1911-1922.

88. James, T. D., K. R. A. S. Sandanayake, R. Iguchi, and S. Shinkai (1995) Novel saccharide-photoinduced electron-transfer sensors based on the interaction of boronic acid and amine. *J. Am. Chem. Soc.* **117,** 8982-8987.

89. Camara, J. N., J. T. Suri, F. E. Cappuccio, R. A. Wessling, and B. Singaram (2002) Boronic acid substituted viologen based optical sugar sensors: modulated quenching with viologen as a method for monosaccharide detection. *Tetrahedron Lett.* **43,** 1139-1141.

90. DiCesare, N., and J. R. Lakowicz (2001) Evaluation of two synthetic glucose probes for fluorescence-lifetime-based sensing. *Anal. Biochem.* **294,** 154-160.

91. DiCesare, N., and J. R. Lakowicz (2001) A new highly fluorescent probe for monosaccharides based on a donor-acceptor diphenyloxazole. *Chem. Commun.* 2022-2023.

92. Badugu, R., J. R. Lakowicz, and C. D. Geddes (2003) A glucose sensing contact lens: A non-invasive technique for continuous physiological glucose monitoring. *J. Fluoresc.* **13,** 371-374.

93. Aslan, K., J. Zhang, J. R. Lakowicz, and C. D. Geddes (2004) Saccharide sensing using gold and silver nanoparticles - A review. *J. Fluoresc.* **14,** 391-400.

94. Medintz, I. L., A. R. Clapp, H. Mattoussi, E. R. Goldman, B. Fisher, and J. M. Mauro (2003) Self-assembled nanoscale biosensors based on quantum dot FRET donors. *Nat. Mater.* **2,** 630-638.

95. Clapp, A. R., I. L. Medintz, J. M. Mauro, B. R. Fisher, M. G. Bawendi, and H. Mattoussi (2004) Fluorescence resonance energy transfer between quantum dot donors and dye-labeled protein acceptors. *J. Am. Chem. Soc.* **126,** 301-10.

96. Barone, P. W., S. Baik, D. A. Heller, and M. S. Strano (2005) Near-infrared optical sensors based on single-walled carbon nanotubes. *Nat. Mater.* **4,** 86-U16.

97. Xu, H., J. W. Aylott, and R. Kopelman (2002) Fluorescent nano-PEBBLE sensors designed for intracellular glucose imaging. *Analyst* **127,** 1471-7.

98. Monson, E., M. Brasuel, M. Philbert, and R. Kopelman (2003) PEBBLE Nanosensors for in vitro Bioanalysis. In *Biomedical Photonics Handbook* (Edited by T. Vo-Dinh), pp. 1-14. CRC Press, New York, NY.

99. Meer, B. W. V. D., G. Coker, and S.-Y. S. Chen (1994) *Resonance Energy Transfer: Theory and Data.* VCH Publishers, New York, NY.

100. Du, H., R. C. A. Fuh, J. Z. Li, L. A. Corkan, and J. S. Lindsey (1998) PhotochemCAD: A computer-aided design and research tool in photochemistry. *Photochem. Photobiol.* **68,** 141-142.

101. Wu, P. G., and L. Brand (1994) Resonance energy-transfer - methods and applications. *Anal. Biochem.* **218,** 1-13.

102. Rolinski, O. J., D. J. S. Birch, L. J. McCartney, and J. C. Pickup (2001) Fluorescence nanotomography using resonance energy transfer: demonstration with a protein-sugar complex. *Phys. Med. Biol.* **46,** N221-N226.

103. Breusegem, S. Y., N. P. Barry, A. C. Mackinnon, X. Y. Lin, B. D. Williams, E. Gratton, and R. M. Clegg (2002) Protein interactions in C. elegans muscle attachment structures studied in vivo by fluorescence resonance energy transfer (FRET). *Biophys. J.* **82,** 491a-492a.

104. Rice, K. G. (2001) Application of fluorescence resonance energy transfer to analyze carbohydrates. *Anal. Biochem.* **297,** 117-122.

105. Ha, T. (2001) Single-molecule fluorescence resonance energy transfer. *Methods* **25,** 78-86.

106. Ko, S., and S. A. Grant (2003) Development of a novel FRET method for detection of Listeria or Salmonella. *Sensor Actuat. B-Chem.* **96,** 372-378.

107. Meadows, D., and J. S. Schultz (1988) Fiber-optic biosensors based on fluorescence energy-transfer. *Talanta* **35,** 145-150.

108. Meadows, D. L., and J. S. Schultz (1993) Design, manufacture and characterization of an optical-fiber glucose affinity sensor-based on an homogeneous fluorescence energy-transfer assay system. *Anal. Chim. Acta.* **280,** 21-30.

109. Tolosa, L., H. Szmacinski, G. Rao, and J. R. Lakowicz (1997) Lifetime-based sensing of glucose using energy transfer with a long lifetime donor. *Anal. Biochem.* **250,** 102-108.

110. Rolinski, O. J., C. Mathivanan, G. Mcnaught, and D. J. S. Birch (2004) Structural information on nanomolecular systems revealed by FRET. *Biosens. Bioelectron.* **20,** 424-430.

111. Rolinski, O. J., D. J. S. Birch, L. J. McCartney, and J. C. Pickup (2001) Sensing metabolites using donor-acceptor nanodistributions in fluorescence resonance energy transfer. *Appl. Phys. Lett.* **78,** 2796-2798.

112. Arimori, S., M. L. Bell, C. S. Oh, and T. D. James (2002) A modular fluorescence intramolecular energy transfer saccharide sensor. *Org. Lett.* **4,** 4249-4251.

113. Ballerstadt, R., A. Polak, A. Beuhler, and J. Frye (2004) In vitro long-term performance study of a near-infrared fluorescence affinity sensor for glucose monitoring. *Biosens. Bioelectron.* **19,** 905-914.

114. Ibey, B. L., H. T. Beier, R. M. Rounds, G. L. Cote, V. K. Yadavalli, and M. V. Pishko (2005) Competitive binding assay for glucose based on glycodendrimer-fluorophore conjugates. *Anal. Chem.* **77,** 7039-7046.

115. Chinnayelka, S., and M. J. McShane (2006) Glucose sensors based on microcapsules containing an orange/red competitive binding resonance energy transfer assay. *Diabetes Technol. Ther.* **8,** 269-78.

116. Meadows, D. L., and J. S. Schultz (1991) A molecular-model for singlet singlet energy-transfer of monovalent ligand receptor interactions. *Biotechnol. Bioeng.* **37,** 1066-1075.

117. Bittiger, H., and H. P. Schnebli (1976) *Concanavalin A as a Tool.* John Wiley & Sons, New York, NY.

118. Guyton, A. C., and J. E. Hall (1996) *Textbook of Medical Physiology.* W.B. Saunders, Philadelphia, PA.

119. Russell, R. J., M. Pishko, C. C. Gefrides, and G. L. Cote (1998) A fluorescent glucose assay using poly-L-lysine and calcium alginate microencapsulated

TRITC-succinyl-Concanavalin A and FITC-dextran. *Proc. IEEE-EMBS* **20,** 2858-2861.

120. Bambot, S., J. R. Lakowicz, and G. Rao (1995) Potential applications of life-time-based, phase-modulation fluorometry in bioprocess and clinical monitoring. *Trends Biotechnol.* **13,** 195-195.

121. Neely, W. B. (1960) Dextran: structure and synthesis. *Adv. Carbohydr. Chem.* **15,** 341-69.

122. Gestwicki, J. E., C. W. Cairo, L. E. Strong, K. A. Oetjen, and L. L. Kiessling (2002) Influencing receptor-ligand binding mechanisms with multivalent ligand architecture. *J. Am. Chem. Soc.* **124,** 14922-14933.

123. Kuwana, E., and E. M. Sevick-Muraca (2002) Fluorescence lifetime spectroscopy in multiply scattering media with dyes exhibiting multiexponential decay kinetics. *Biophys. J.* **83,** 1165-1176.

124. Hutchinson, C. L., T. L. Troy, and E. M. Sevick-Muraca (1996) Fluorescence-lifetime determination in tissues or other scattering media from measurement of excitation and emission kinetics. *Appl. Optics* **35,** 2325-2332.

125. Szmacinski, H., and J. R. Lakowicz (1993) Optical measurements of pH using fluorescence lifetimes and phase-modulation fluorometry. *Anal. Chem.* **65,** 1668-1674.

126. Wlodarczyk, J., and B. Kierdaszuk (2003) Interpretation of fluorescence decays using a power-like model. *Biophys. J.* **85,** 589-598.

127. Hirayama, S., Y. Sakai, K. P. Ghiggino, and T. A. Smith (1990) The application of a simple deconvolution method to the analysis of stretched exponential fluorescence decay functions. *J. Photoch. Photobio. A* **52,** 27-38.

128. Grant, S. A., R. C. Stringer, S. Studer, D. Lichlyter, and C. L. Lorenzen (2005) Viability of a FRET dual binding technique to detect calpastatin. *Biosens. Bioelectron.* **21,** 438-444.

129. Huber, D. L. (1979) Donor fluorescence at high trap concentration. *Phys. Rev. B* **20,** 5333-5338.

130. Gosele, U., M. Hauser, U. K. A. Klein, and R. Frey (1975) Diffusion and long-range energy-transfer. *Chem. Phys. Lett.* **34,** 519-522.

131. Klafter, J., and A. Blumen (1985) Direct energy-transfer in restricted geometries. *J. Lumin.* **34,** 77-82.

132. Rolinski, O. J., and D. J. S. Birch (2000) Determination of acceptor distribution from fluorescence resonance energy transfer: Theory and simulation. *J. Chem. Phys.* **112,** 8923-8933.

133. Rolinski, O. J., and D. J. S. Birch (2002) Structural sensing using fluorescence nanotomography. *J. Chem. Phys.* **116,** 10411-10418.

134. Birch, D. J. S., and O. J. Rolinski (2001) Fluorescence resonance energy transfer sensors. *Res. Chem. Intermediat.* **27,** 425-446.

135. Rolinski, O. J., D. J. S. Birch, L. J. McCartney, and J. C. Pickup (2000) A method of determining donor-acceptor distribution functions in Forster resonance energy transfer. *Chem. Phys. Lett.* **324,** 95-100.

136. Kuwana, E., and E. M. Sevick-Muraca (2003) Fluorescence lifetime spectroscopy for pH sensing in scattering media. *Anal. Chem.* **75,** 4325-4329.

137. Cerussi, A. E., J. S. Maier, S. Fantini, M. A. Franceschini, W. W. Mantulin, and E. Gratton (1997) Experimental verification of a theory for the time-resolved fluorescence spectroscopy of thick tissues. *Appl. Optics* **36,** 116-124.

138. Rolinski, O. J., D. J. S. Birch, L. J. McCartney, and J. C. Pickup (1999) Fluorescence resonance energy transfer from allophycocyanin to malachite green. *Chem. Phys. Lett.* **309,** 395-401.

139. Becker, J. W., G. N. Reeke, J. L. Wang, B. A. Cunningham, and G. M. Edelman (1975) Covalent and 3-Dimensional Structure of Concanavalin-A .3. Structure of Monomer and Its Interactions with Metals and Saccharides. *J. Biol. Chem.* **250,** 1513-1524.

140. Luby-Phelps, K. (1989) Preparation of fluorescently labeled dextrans and ficolls. *Methods Cell. Biol.* **29,** 59-73.

141. Haugland, R. P. (2002) *Handbook of Fluorescent Probes and Research Products.* Molecular Probes, Eugene, OR.

142. Lakowicz, J. R., E. Gratton, G. Laczko, H. Cherek, and M. Linkeman (1984) Analysis of fluorescence decay kinetics from variable-frequency phase-shift and modulation data. *Biophys. J.* **45,** A34-A34.

143. Ehwald, R., R. Ballerstadt, and H. Dautzenberg (1996) Viscosimetric affinity assay. *Anal. Biochem.* **234,** 1-8.

144. Ballerstadt, R., and R. Ehwald (1994) Suitability of aqueous dispersions of dextran and Concanavalin A for glucose sensing in different variants of the affinity sensor. *Biosens. Bioelectron.* **9,** 557-567.

145. Porter, G., and C. J. Tredwell (1978) Picosecond time resolved energy-transfer between Rhodamine 6g and Malachite Green. *Chem. Phys. Lett.* **56,** 278-282.

146. Lakowicz, J. R., F. N. Castellano, J. D. Dattelbaum, L. Tolosa, G. Rao, and I. Gryczynski (1998) Low frequency modulation sensors using nanosecond fluorophores. *Anal. Chem.* **70,** 5115-5121.

147. Gryczynski, Z., I. Gryczynski, and J. R. Lakowicz (2003) Fluorescence-sensing methods. *Method Enzymol.* **360,** 44-75.

148. Draxler, S., and M. E. Lippitsch (1996) Time-resolved fluorescence spectroscopy for chemical sensors. *Appl. Optics* **35,** 4117-4123.

149. Rosenzweig, Z., and R. Kopelman (1996) Analytical properties and sensor size effects of a micrometer-sized optical fiber glucose biosensor. *Anal. Chem.* **68,** 1408-1413.

150. Neubauer, A., D. Pum, U. B. Sleytr, I. Klimant, and O. S. Wolfbeis (1996) Fibre-optic glucose biosensor using enzyme membranes with 2-D crystalline structure. *Biosens. Bioelectron.* **11,** 317-325.

151. West, J. L., and J. A. Hubbell (1995) Photopolymerized hydrogel materials for drug-delivery applications. *React. Polym.* **25,** 139-147.

152. Andreopoulos, F. M., E. J. Beckman, and A. J. Russell (1998) Light-induced tailoring of PEG-hydrogel properties. *Biomaterials* **19,** 1343-1352.

153. Press, W. H., S. A. Teukolsky, W. Vetterling, and B. P. Flannery (1992) *Numercial Recipes in Fortran77: the Art of Scientific Computing.* Cambridge University Press, New York, NY.

154. Sun, Z. G., Y. Q. Huang, and E. M. Sevick-Muraca (2002) Precise analysis of frequency domain photon migration measurement for characterization of concentrated colloidal suspensions. *Rev. Sci. Instrum.* **73,** 383-393.

155. McShane, M. J., S. Rastegar, M. Pishko, and G. L. Cote (2000) Monte Carlo modeling for implantable fluorescent analyte sensors. *IEEE T. Bio-Med. Eng.* **47,** 624-632.

156. Rossi, L. M., A. D. Quach, and Z. Rosenzweig (2004) Glucose oxidase-magnetite nanoparticle bioconjugate for glucose sensing. *Anal. Bioanal. Chem.* **380,** 606-613.

157. Yadavalli, V. K., R. J. Russell, M. V. Pishko, M. J. McShane, and G. L. Cote (2005) A Monte Carlo simulation of photon propagation in fluorescent poly(ethylene glycol) hydrogel microsensors. *Sensor. Actuat. B-Chem.* **105,** 365-377.

158. Bohen, C. F., and D. R. Huffman (1983) *Absorption and Scattering of Light by Small Particles.* John Wiley & Sons, New York, NY.

159. Huang, Y., Z. G. Sun, and E. M. Sevick-Muraca (2002) Assessment of electrostatic interactions in dense colloidal suspensions with multiply scattered light. *Langmuir* **18,** 2048-2053.

160. Meglinski, I. V., and S. J. Matcher (2002) Quantitative assessment of skin layers absorption and skin reflectance spectra simulation in the visible and near-infrared spectral regions. *Physiol. Meas.* **23,** 741-753.

161. Pan, T. S., S. S. Dali, and E. M. Sevick-Muraca (2005) Evaluation of photon migration using a two speed model for characterization of packed powder beds and dense particulate suspensions. *Opt. Express* **13,** 3600-3618.

162. Grant, F. A. (1959) Properties of rutile (titanium dioxide). *Rev. Mod. Phys.* **31,** 646-674.

163. Wang, L. H., S. L. Jacques, and L. Q. Zheng (1995) Mcml - Monte-Carlo modeling of light transport in multilayered tissues. *Comput. Meth. Prog. Bio.* **47,** 131-146.

164. Yang, R. Y., R. P. Zou, A. B. Yu, and S. K. Choi (2006) Pore structure of the packing of fine particles. *J. Colloid Interf. Sci.* **299,** 719-725.

165. Yang, R. Y., R. P. Zou, and A. B. Yu (2003) Effect of material properties on the packing of fine particles. *J. Appl. Phys.* **94,** 3025-3034.

166. Pan, T. S., and E. M. Sevick-Muraca (2006) Evaluation of ingredient concentration in powders using two-speed photon migration theory and measurements. *J. Pharm. Sci-Us.* **95,** 530-541.

167. Pogue, B. W., and G. Burke (1998) Fiber-optic bundle design for quantitative fluorescence measurement from tissue. *Appl. Optics* **37,** 7429-7436.

168. Vishwanath, K., and M. A. Mycek (2005) Time-resolved photon migration in bi-layered tissue models. *Opt. Express* **13,** 7466-7482.

169. Torquato, S., T. M. Truskett, and P. G. Debenedetti (2000) Is random close packing of spheres well defined? *Phys. Rev. Lett.* **84,** 2064-2067.

170. Pan, T. S., D. Barber, D. Coffin-Beach, Z. G. Sun, and E. M. Sevick-Muraca (2004) Measurement of low-dose active pharmaceutical ingredient in a pharmaceutical blend using frequency-domain photon migration. *J. Pharm. Sci-Us.* **93,** 635-645.

171. Patterson, M. S., and B. W. Pogue (1994) Mathematical-model for time-resolved and frequency-domain fluorescence spectroscopy in biological tissue. *Appl. Optics* **33,** 1963-1974.

172. Sun, Z. G., S. Torrance, F. K. McNeil-Watson, and E. M. Sevick-Muraca (2003) Application of frequency domain photon migration to particle size analysis and monitoring of pharmaceutical powders. *Anal. Chem.* **75,** 1720-1725.

173. Torrance, S. E., Z. Sun, and E. M. Sevick-Muraca (2004) Impact of excipient particle size on measurement of active pharmaceutical ingredient absorbance in mixtures using frequency domain photon migration. *J. Pharm. Sci-Us.* **93,** 1879-1889.

174. Hutchinson, C. L., J. R. Lakowicz, and E. M. Sevick-Muraca (1995) Fluorescence lifetime-based sensing in tissues - a computational study. *Biophys. J.* **68,** 1574-1582.

APPENDIX

NOMENCLATURE

Abbreviations:

3D	three dimensional
A	acceptor
Acryl-	α-acryloyl
AF568	Alexa Fluor 568
AF647	Alexa Fluor 647
AMCA	7-amino-4-methyl-coumarin
ANS	8-anilino-1-naphthalenesulfonic acid
APC	Allophycocyanin
Ar	argon
BSGK	bacillus stearothermophilus
CB	cascade blue
CAD	computer-aided design
CCD	charge-coupled device
ConA	concanavalin A
CQ	collisional quenching
C-SNAFL	carboxy seminaphthofluorescein
CW	continuous wave
Cy	cyanine
D	donor
DI	deionized
DMSO	dimethyl sulfoxide
DTTCI	3,3-diethylthiatricarbocyanine iodide
EM	emission
EOM	electro-optic modulator
EtOH	ethanol
EX	excitation
FCC	face centered cubic
FD	frequency-domain
FDPM	frequency-domain photon migration
FITC	fluorescein isothiocyanate
FRET	fluorescence resonance energy transfer
FWHM	full width at half maximum
GBP	glucose-binding protein
GFP	glucose fluorescence protein
GOX	glucose oxidase

Abbreviations continued:

HMP	hydroxy-2-methylpropiophenone
I-ANS	2-(4-iodoacetamidoanilino) naphthalene-6-sulfonic acid
ICG	indocyanine green
Kr	krypton
LbL	layer by layer
LPF	long pass filter
M	modulation
MC	Monte Carlo
MeOH	methanol
MG	Malachite Green
MIMG	maltose-insulin-Malachite Green
MLC	metal-ligand complexes
MOPS	morpholinopropanesulfonic
MW	molecular weight
MWCO	molecular weight cut-off
N/A	not applicable
NaB	sodium bicarbonate buffer
NHS	ω-N-hydroxysuccinimidyl ester
NIR	near infrared
OCT	optical coherence tomography
P	probability
PAA	polyacrylamide
PBS	phosphate-buffered saline
PCCA	polymerized crystalline colloidal array
PEBBLE	probes encapsulated by biologically localized embedding
PEG	poly(ethylene glycol)
PEG-NHS	α-acryloyl ω-N-hydroxysuccinimidyl ester of PEG-propionic acid
PEG-DA	poly(ethylene glycol) diacrylate
PET	photoninduced electron transfer
PMT	photomultiplier tube
PS	phase shift
QD	quantum dot
RCP	random close packing
RITC	rhodamine isothiocyanate
RF	radio frequency
SNARF	seminaphthorhodafluor
SNAFL	seminaphthofluorescein
SNR	signal to noise ratio
SPR	surface plasmon resonance
Succinyl-	succinylated
TI-Amp	transimpedance amplifier
TRITC	tetramethylrhodamine isothiocyanate.

Abbreviations continued:

TPT	trimethylolpropane triacrylate
UV	ultraviolet
YFP	yellow fluorescence protein

English symbols:

a_i^s	coefficients of orthonormal Laguerro polynomials
a_j	pre-exponential factor of a component with a lifetime τ_j
A_0	ground electronic state of acceptor
A_1	excited electronic state of acceptor
AC	amplitude of intensity-modulated light [a.u.]
[A]	acceptor concentration [mol/L]
B	time-dependent parameter in the fractal FRET decay model
c	light speed in vacuum [m/s]
C_A	critical acceptor concentration [mol/L]
C_D	critical donor concentration [mol/L]
[C]	concentration [mol/L]
$[C_q]$	quencher concentration [mol m^{-3}]
C_p	specific heat of the medium [J mol^{-1} K^{-1}]
d	minimum donor-acceptor distance
d_p	diameter of microspheres [m]
D	optical diffusion coefficient [cm]
D_m	optical diffusion coefficient at emission wavelength
D_x	optical diffusion coefficient at excitation wavelength
E	FRET efficiency
$F(\omega)$	Fourier transform of the FRET decay kinetics
g	the average of the cosine of the scattering angle
h	Planck's constant [J s]
i	imaginary number
I(t)	fluorescence intensity at time t [W cm^{-2}]
I_0	fluorescence intensity at time t=0 [W cm^{-2}]
I_{AC0}	fluorescence amplitude at time t=0 [W cm^{-2}]
I_{AC}	fluorescence amplitude at time t [W cm^{-2}]
J	overlaps of donor emission and acceptor absorption spectra
k_1	binding constant [L/mol]
k_2	binding constant [L/mol]
K	association constant [L/mol]
L_i^s	orthonomal Laguerro polynomials
L	path length [m]
n	refractive index
n_p	refractive index of particle
n_{par}	refractive index of microsphere

English symbols continued:

n_m	refractive index of medium
n_{tis}	refractive index of surrounding tissue or medium
$N(\omega)$	imaginary part of Fourier transform of the decay kinetics
m	the number of frequencies for which data are measured
M_M	measured modulation [a.u.]
M_P	model predicted modulation [a.u.]
N_A	Avogadro's number
$P(\omega)$	real part of Fourier transform of the decay kinetics
Q	fluorescence quantum efficiency
r	position [cm]
r	spherical particle radius [m]
r	donor-acceptor distance [m]
r_{AD}	collision distance [m]
$r_{s\text{-}d}$	source-detector distance [m]
r^*	interaction radius [m]
$\vec{r}$	photon position vector
R	Fresnel's reflection coefficient
R_0	Förster distance [m]
R_0^{DD}	critical energy transfer distance for donor-donor energy transfer [m]
s	step size
S_o	electronic ground state
S_1	excited singlet state
S_x	excitation source term
S_m	emission source term
t	time [s]
t_d	time delay due to the generation of fluorescence [s]
<t>	mean "time of flight" [s]
U(r,t)	photon density at position r and time t [W m^{-3}]
U_x	excitation photon density [W m^{-3}]
U_m	emission photon density [W m^{-3}]
v	speed of sound in the medium [m/s]
v_E	frequency of excitation [1/s]
w	photon weight

Greek symbols:

α	parameter related to diffusion coefficients of fluorophore and quencher
α	parameter in the generalized Förster model
β	thermal expansion coefficient [K^{-1}]
β	parameter related to diffusion coefficients of fluorophore and quencher
β	parameter in the generalized Förster model

Greek symbols continued:

γ	parameter in the generalized Förster model
δ_θ	estimated uncertainties in the measured phase-shift [deg]
δ_M	estimated uncertainties in the measured modulation-ratio
ε_A	extinction coefficients [M^{-1} cm^{-1}]
ϕ	observed rotation
ζ_m	detection efficiency factor of the instrumentation at emission wavelength
ξ_{axf}	extinction coefficients of fluorophore at the excitation wavelength
θ	phase shift [degree]
θ_0	phase shift at time t=0 [degree]
θ_A	angle between absorption dipole of acceptor and the joining vector
θ_D	angle between emission dipole of donor and the joining vector [degree]
θ_M	measured phase shift [degree]
θ_P	model predicted phase shift [degree]
θ_T	angle between emission dipole of donor and absorption dipole of acceptor [degree]
θ_i	angle of incidence of photon on the boundary of particles
θ_t	angle of transmission of photon on the boundary of particles
κ_{nr}	non-radiative rate of relaxation [1/s]
κ_r	radiative rate of relaxation [1/s]
κ_T	rate of fluorescence energy transfer [1/s]
κ_q	Stern-Volmer constant [m^3/s.mol]
κ^2	orientation factor
λ	wavelength [nm]
μ_a	absorption coefficient [cm^{-1}]
μ_a^w	water absorption coefficient [cm^{-1}]
μ_a^g	intrinsic glucose absorption coefficient [cm^{-1}]
μ_{ax}	absorption coefficient at excitation wavelength [cm^{-1}]
μ_{am}	absorption coefficient at emission wavelength [cm^{-1}]
μ_{axf}	absorption coefficient at excitation wavelength by fluorophore [cm^{-1}]
μ_s	scattering coefficient [cm^{-1}]
μ_s'	isotropic or reduced scattering coefficient [cm^{-1}]
μ_{sx}'	isotropic scattering coefficient at excitation wavelength [cm^{-1}]
μ_{sm}'	isotropic scattering coefficient at emission wavelength [cm^{-1}]
$\Delta\mu_{sg}$	change of scattering coefficient caused by glucose [cm^{-1}]
μ_t	total attenuation coefficient [cm^{-1}]
$\overrightarrow{\mu_A}$	unit vector of acceptor transition moment
$\overrightarrow{\mu_D}$	unit vector of donor trabsition moment
$\vec{v}$	photon moving direction
ς	random number

Greek symbols continued:

$\rho(r)$	probability function
τ	fluorophore lifetime [s]
τ_0	unquenched fluorophore lifetime [s]
τ_{avg}	fluorophore average lifetime [s]
τ_{avg}^{scat}	fluorophore average lifetime at presence of scattering
τ_j	lifetime of fluorescent component $_j$ [s]
τ_F	donor lifetime [s]
Φ	light fluence [W/cm^2]
ρ_P	volume density [m^{-3}]
χ^2	the error- weighted sum of squared deviations between the measured and calculated values of phase delay and amplitude demodulation
ω	angular modulation frequency [rad/sec]

VITA

FENG LIANG

Department of Chemical Engineering
Mail stop: 3122
Texas A&M University, College Station
TX 77843-3122

EDUCATION

Texas A&M University, College Station, TX
Ph.D., Chemical Engineering, 2006

China University of Petroleum, Beijing
M.S., Chemical Engineering, 2001

China University of Petroleum, Beijing
B.S., Chemical Engineering, 1997

PEER REVIEWED PUBLICATIONS

Kuwana, E., F. Liang, and E. M. Sevick-Muraca (2004) Fluorescence lifetime spectroscopy of a pH-sensitive dye encapsulated in hydrogel beads. *Biotechnol. Progr.* 20, 1561-1566.

Liang, F., T. Pan, and E. M. Sevick-Muraca (2005) Measurements of FRET in a glucose-sensitive affinity system with frequency-domain lifetime spectroscopy. *Photochem. Photobiol.* 81, 1386-1394.

Adams, K., S. Ke, S. Kwon, F. Liang, Z. Fan, Y. Lu, K. Hirshi, M. Maward, M. Barry, and E. M. Sevick-Muraca (2006) Comparison of visible and near-infrared wavelength excitable fluorescent dyes for molecular imaging of cancer. submitted to *J. Biomed. Opt.*

Liang, F., T. Pan, and E. M. Sevick-Muraca (2006) A time-resolved Monte Carlo simulation of photon migration in microsphere-based implantable sensors. in preparation, for submission to *Biosens. Bioelectron.*

Dali, S., J. Rasmussen, Y. Huang, F. Liang, and E. M. Sevick-Muraca (2006) Modeling and study of dense monodisperse charged lattices using frequency domain photon migration measurements. in preparation, for submission to *Langmuir*.